NOTICE

The quality of this microform is heavily dependent upon the quality of the original thesis submitted for microfilming. Every effort has been made to ensure the highest quality of reproduction possible.

If pages are missing, contact the university which granted the degree.

Some pages may have indistinct print especially if the original pages were typed with a poor typewriter ribbon or if the university sent us an inferior photocopy.

Reproduction in full or in part of this microform is governed by the Canadian Copyright Act, R.S.C. 1970, c. C-30, and subsequent amendments.

AVIS

La qualité de cette microforme dépend grandement de la qualité de la thèse soumise au microfilmage. Nous avons tout fait pour assurer une qualité supérieure de reproduction.

S'il manque des pages, veuillez communiquer avec l'université qui a conféré le grade.

La qualité d'impression de certaines pages peut laisser à désirer, surtout si les pages originales ont été dactylographiées à l'aide d'un ruban usé ou si l'université nous a fait parvenir une photocopie de qualité inférieure.

La reproduction, même partielle, de cette microforme est soumise à la Loi canadienne sur le droit d'auteur, SRC 1970, c. C-30, et ses amendements subséquents.

ANALYTICAL AND EXPERIMENTAL STUDIES OF THE OPEN-LOOP FREQUENCY RESPONSE OF A ROTARY ELECTROHYDRAULIC SERVOSYSTEM

King Hoi Leung

A Thesis

in

The Department

of

Mechanical Engineering

Presented in Partial Fulfillment of the Requirements
for the Degree of Master of Engineering at
Concordia University
Montréal, Québec, Canada

March 1989

ISBN 0-315-51391-8

ABSTRACT

Analytical and Experimental Studies of the Open-Loop Frequency Response of a Rotary Electrohydraulic Servosystem

King Hoi Leung

In a previous work, a new concept of electrohydraulic servovalve which incorporates a pressure relief valve as well as a variable orifice restrictor in the fluid return line was proposed and the closed loop system responses subjected to step inputs were investigated. In this thesis, a nonlinear mathematical model based on dimensionless quantities of the servosystem is derived and solved by means of digital computer to analyse the effects of the return pressure and the drain orifice area on the open-loop frequency responses. An experimental setup with rotary actuator was built and experiments were carried to compare with the previous research. Frequency response experimentation was carried out and found to match very well with the dimensionless analysis. The results indicate that these parameters could be tuned to obtain a high amplitude ratio at low frequency and yet a low peak amplitude in the resonance frequency range. This corresponds to a high gain and high damping system as predicted by the step input responses investigation. The system exhibits however a slightly lower resonance frequency which may represent a limitation for certain types of application. A design procedure was proposed to find out the boundaries of the operating zone for a higher gain and a higher damping response in the new configuration.

ACKNOWLEDGEMENT

The author would like to express his gratitude and deep appreciation to his supervisors Dr. S. LeQuoc and Dr. R.M.H. Cheng for their supervision, patience, guidance and encouragement during the whole process of this project, and for providing the resources necessary to carry out this research.

The author also highly appreciates the technical competence and numerous suggestions by Mr. W. Fitch for building the experimental setup, which can only be completed with his generous help. Gratitude is also due to the technical staff in the Engineering Workshop.

The design of the manifold block for the hydraulic full wave rectifier by Mr. C. Lisio and Mr. D. Miele is highly appreciated. Thanks also go to other graduate students in the department for their help and support.

The facilities provided by the Department of Mechanical Engineering and the Center for Industrial Controls of Concordia University to carry out this research work is also acknowledged.

The funding for this project was provided by Natural Science and Engineering Council (NSERC) of Canada, under grant No. A1718 and A8662.

TABLE OF CONTENT

LIST OF FIGURES

NOMENCLATURE

A = amplitude of sinusoidal input, V

A_0 = restrictor opening, m^2

A_v = servovalve opening, m^2

B = viscous damping coefficient, Nms

C_d = flow discharge coefficient

C_D = dimensionless damping coefficient

C_{em} = motor total motor external leakage coefficient, $(m^3/s)/(N/m^2)$

C_{em1} = external leakage coefficient from chamber 1 of motor, $(m^3/s)/(N/m^2)$

C_{em2} = external leakage coefficient from chamber 2 of motor, $(m^3/s)/(N/m^2)$

C_{ep} = external leakage coefficient from pump, $(m^3/s)/(N/m^2)$

C_f = dynamic internal friction coefficient

C_{fs} = static internal friction coefficient

C_{im} = motor internal leakage coefficient, $(m^3/s)/(N/m^2)$

C_v = flow coefficient

D_m = displacement of motor, m^3/rad

G = specific gravity

I = servovalve input current, mA

I_ℓ = input current to loading pump servoamplifier, mA

I_m = input current to motor servoamplifier, mA

I_{max} = maximum servovalve input current, mA

J = inertial load, Nms^2

K_a = servovalve amplifier gain, mA/V

K_f = velocity feedback gain, V/(rad/s)

K_v = servovalve area constant, m^2/m

K_x = servovalve torque motor constant, m/mA

$P_{1,2}$ = pressure in actuator chambers, N/m^2

P_ℓ = load pressure, N/m^2

P_r = relief valve setting pressure, N/m^2

P_s = supply pressure, N/m^2

$Q_{1,2}$ = flow rate in/out of actuator, m^3/s

Q_{em1} = external leakage flow from chamber 1, m^3/s

Q_{em2} = external leakage flow from chamber 2, m^3/s

Q_{im} = internal leakage flow inside the motor, m^3/s

Q_ℓ = load flow, m^3/s

Q_o = flow rate through orifice, m^3/s

Q_s = maximum supply flow, m^3/s

T_c = dynamic frictional torque, Nm

T_{cs} = static frictional torque, Nm

T_d = damping torque, Nm

T_f = dynamic friction torque, Nm

T_g = ideal generated torque, Nm

T_ℓ = actuator load torque, Nm

T_L = net torque delivered to the load on the rotating shaft, Nm

V = volume of oil under compression in one chamber, m^3

V_i = input command, V

V_{iamp} = amplitude of input voltage command, V

V_{imax} = maximum input command, V

V_{ioff} = offset of input voltage command, V

β = bulk modulus of fluid, N/m^2

ΔP = pressure difference, N/m^2

μ = absolute viscosity of oil, Ns/m^2

ω = angular velocity, rad/s

ω_h = hydraulic natural frequency of conventional configuration, rad/s

ω_{max} = maximum angular velocity, rad/s

ω_n = undamped natural frequency, rad/s

ω_r = input frequency, rad/s

ρ = mass density of fluid, kg/m^3

τ_v = servovalve time constant, s

Non-dimensionalised quantities :

$a = A/V_{imax}$ = amplitude of sinusoidal input

$c_{em} = JC_{em}\omega_h/D_m^2$ = leakage load factor

$c_{im} = JC_{im}\omega_h/D_m^2$ = leakage load factor

$c_\ell = c_{im} + c_{em}/2$ = leakage load factor

$i = I/I_{max}$ = servovalve input current

$p_i = P_i/P_s$ = pressure in actuator chambers, i = 1,2

$p_\ell = P_\ell/P_s$ = load pressure

$p_r = P_r/P_s$ = return back pressure

$q_i = Q_i/Q_s$ = flow rate in/out of actuator, i = 1,2

$q_\ell = Q_\ell/Q_s$ = load flow

$t_\ell = T_\ell/P_s D_m$ = load torque factor

$v_i = V_i/V_{imax}$ = input voltage

$v_{iamp} = V_{iamp}/V_{imax}$ = offset of input command

$v_{ioff} = V_{ioff}/V_{imax}$ = amplitude of input command

$x_v = A_v/A_{vmax}$ = servovalve opening

$x_0 = A_0/A_{vmax}$ = restrictor opening

$v_i = V_i/V_{imax}$ = input command

α = $J\omega_h Q_s / P_s D_m^2$ = inertia load factor for rotary actuator

ε = $(I_{max}/K_a)/(K_f/\omega_{max})$ = ratio of maximum error voltage to maximum feedback voltage

γ = $B\omega_{max}/P_s D_m$ = viscous load factor

λ = load factor for linear actuator

ϕ = ω/ω_{max} = actuator velocity

τ = $\omega_r t$ = time unit

τ_v^* = $\omega_h \tau_v$ = servovalve time constant

ω^* = ω_r/ω_h = input frequency

ω_d^* = damped natural frequency

CHAPTER 1

INTRODUCTION

1.1 General

Energy is required to have work done. An engineer is always required to solve the problems of the transmission of energy and power. Different level of technology has been developed to solve for them.

For the field of high power transmission, fluid power control is preferred to electrical power control. A fluid power device is a component or system which employs a fluid to transmit power from one point to another. It has the advantages of higher power to weight ratio, more accurate controls, faster responses and more rigid in the steady state.

Electrohydraulic servosystems were originally developed for aircraft and missiles because their efficiency, compactness, and high response capabilities offered distinct advantages. As the technology of electrohydraulic servomechanisms evolved, the use of servosystems broadened to include machine tools, mobile equipments, aircraft simulators, computer disc accessing controls, and other applications where a load must be positioned accurately. All electrohydraulic servosystems include a servovalve which links the electrical and hydraulic elements of a system. The servovalve can be considered as a signal to power transducer. With a small input current signal of up to

20 mA, the hydraulic actuator can output several horsepowers to do work precisely. Such a high power gain makes it serve as a very effective forward loop amplifier.

1.2 Introduction to Servovalves

Maskrey and Thayer [1] gave a detailed historical development of servovalves. They included the description of the evolution of servovalves from the single-stage valve to first patented two-stage valve by Tinsley of England in 1946. It was then followed by the development of using a flapper-nozzle variable orifice driven by a torque motor in first stage in conjunction with a fixed orifice to drive the second stage by W. C. Moog in 1950. Then, there were other major developments achieved till late 1950's, which led to the present form of the two-stage electrohydraulic servovalves.

A three-stage valve [2] is the result of the feeding back of signal from the Linear Variable Differential Transducer working on a spool valve to a two-stage pilot valve [3]. It allows higher flow and slewrates than are possible with the basic two-stage servovalves. This combination provides remarkedly improved threshold, hysteresis, pressure gain and null shift characteristics.

The manufacturer of Moog servovalves provides the manual [4] for the method of reading off the transfer functions from the frequency response diagrams. It also gives the appropriate transfer functions of standard flow control, pressure control, pressure-flow control (PQ), dynamic

pressure feedback (DPF), static load error washout (SLEW) and acceleration switching (AS) servovalves.

The 3-part article of Niemas [5], explains what servovalves are, how they work, and how to select them. It considers how a servovalve affects system requirements and discusses the inter-relationships between servovalves and system parameters. He also gave examples to show how a designer should go about establishing system requirement priorities.

1.3 Literature Survey

1.3.1 On the Servovalve Performance

Nikiforuk, Ukrainetz and Tsai [6] gave a detailed analysis of a flow-compensated, two-stage, four-way electrohydraulic servovalve. De Pennington, 't Mannetje and Bell [7] found that a linear transfer function of the third model was an adequate model for a two-stage electrohydraulic flow control valve.

Martin and Burrows [8] compared the frequency responses of an experimental electrohydraulic position control system and its simulation. It was found that a second order compensated valve model based on steady state considerations provided a good correlation with the experimental system up to 35 Hz and could be used for stability calculation up to 80 Hz. Kaneko [9] described the establishment of a design method to build a pressure control servovalve, which was able to

obtain a linear pressure output from the input current independent to the change in flowrate.

Lequoc, Cheng and Limaye [10], [11], [12], [13] proposed a new configuration of connection between a servovalve and its actuator. With the help of a directional control valve, a metering orifice valve and a pressure relief valve, they found that the new configuration could show a higher steady state gain and higher damping than the conventional configuration in the dynamic responses if it were properly tuned. A new design procedure was also proposed to define the region of tuning that could give the advantageous characteristics.

1.3.2 On the Characteristics of Servosystem

Several articles are found on the subject of servovalve-controlled hydraulic motor. Hibi and Ichikawa [14], [15] and Nonnenmacher [16] gave the measurement methods and mathematical models for the torque characteristics of hydraulic motors. Glickman [17] gave a detailed analysis of the transient speed responses of a servovalve-controlled hydraulic motor.

Some articles are found studying the problem of the asymmetry or nonlinearities of the servoactuator. Watton [18] studied the open loop response of servovalve-controlled singl -rod linear actuator. Nondimensional results were presented as an aid to system design, and a boundary was established such that a simplified approximation may be used. Shearer [19], Parnaby [20], Leburn and Scavarda [21] studied the

nonlinear effect of coulomb friction in hydraulic servosystems. Shearer modelled valve-controlled ram-type servosystem with position feedback. With alternate ramp input, he found that the system stability became marginal due to the lack of damping from dry friction when small amplitude inputs were used. Parnaby showed how stability boundary can be predicted for a servomechanism with nonlinear friction under conditions of autonomous operation. Leburn and Scavarda included hysteresis with the coulomb friction effect at the torque motor in the design of electrohydraulic exciter.

1.3.3 On the Sensitivity Analysis

Sensitivity analysis is necessary for the investigation of the influence of parameter variations on the dynamic behaviour of the system. LeQuoc [22] demonstrated from the analysis that for perfectly square edged metering orifices, the maximum null pressure sensitivity could be obtained by having an underlap equal to the radial clearance. For practical valves, due to the rounding of orifice edges, the null pressure sensitivity would increase when the underlap was less than the radial clearance and would decrease otherwise. Vilenius [23] applied sensitivity analysis to electrohydraulic position control servos. From the results of simulation and experimentation, he concluded that the deadband should be as small as possible. The viscous friction and actuator leakage were factors to which the position control servos were quite insensitive. The piston area was a very effective factor with both small and large deadbands. If the deadband were large, the influence of the compliance of the system was exceptionally strong.

Farahat [24] compared four different sensitivity analysis methods to each other by studying the sensitivity of the actuator piston velocity of A. Limaye's setup [13]. All the methods showed that the area of the actuator piston was the most sensitive parameter and the static friction was the insensitive parameter.

1.3.4 On the Nondimensional Analysis

Nondimensional analysis is often used because it can generalise the situation and reduce the number of parameters. Two similar systems with different sets of parameters can be compared if they are nondimensionalised.

In the book Control of Fluid Power by McCloy and Martin [25], the authors used the nondimensional method to investigate the steady state and transient flow forces in the valves, cavitation, the effects of underlap on cavitation and the small signal responses. In one of their papers [26], they had all the parameters of a servovalve controlled piston non-dimensionalised for the investigation of the limit cycle oscillations. The effects of cavitation, hysteresis and time delay on the amplitude, period and stability of these oscillations were also investigated. Stability of all steady state limit cycle oscillations were examined by considering small perturbations about the limit cycle solution point.

Montgomery and Lichtarowicz [27] used the nondimensionalised equations of the system to examine the effects of various asymmetrical

valve lap conditions on both open and closed loop responses. The experimental results were nondimensionalised and then compared with the simulation. They confirmed quantitatively the effects of lap conditionon the computed amplitude frequency responses.

Tumarkin [28] used nondimensional analysis all over his book to compare steady state characteristics of different predicted circuits, which were structurally synthesized from controlled, constant and variable connections between their elements.

1.4 Review of Previous Research

The idea of this research first came from the structural classification of servocircuits by Tumarkin [28]. He arranged possible connections between different elements to predict new circuits with special properties and characteristics. He started with the servocircuit in class 4 - group 1, which had an uncontrolled discharge port and was assumed to offer a constant back pressure. A fine metering valve and a pressure relief valve were introduced in the drain line. A 4 way, 3 positionand spring-centred directional control valve was located between the servovalve and the actuator (Fig. 1.1) so that the system could operate in both directions. The on-off controller, receiving the sign of the error signal, switched the appropriate solenoid of the directional control valve. A modular servovalve with all these hydraulic components put together was designed [13].

A steady state nondimensional analysis was then carried out to

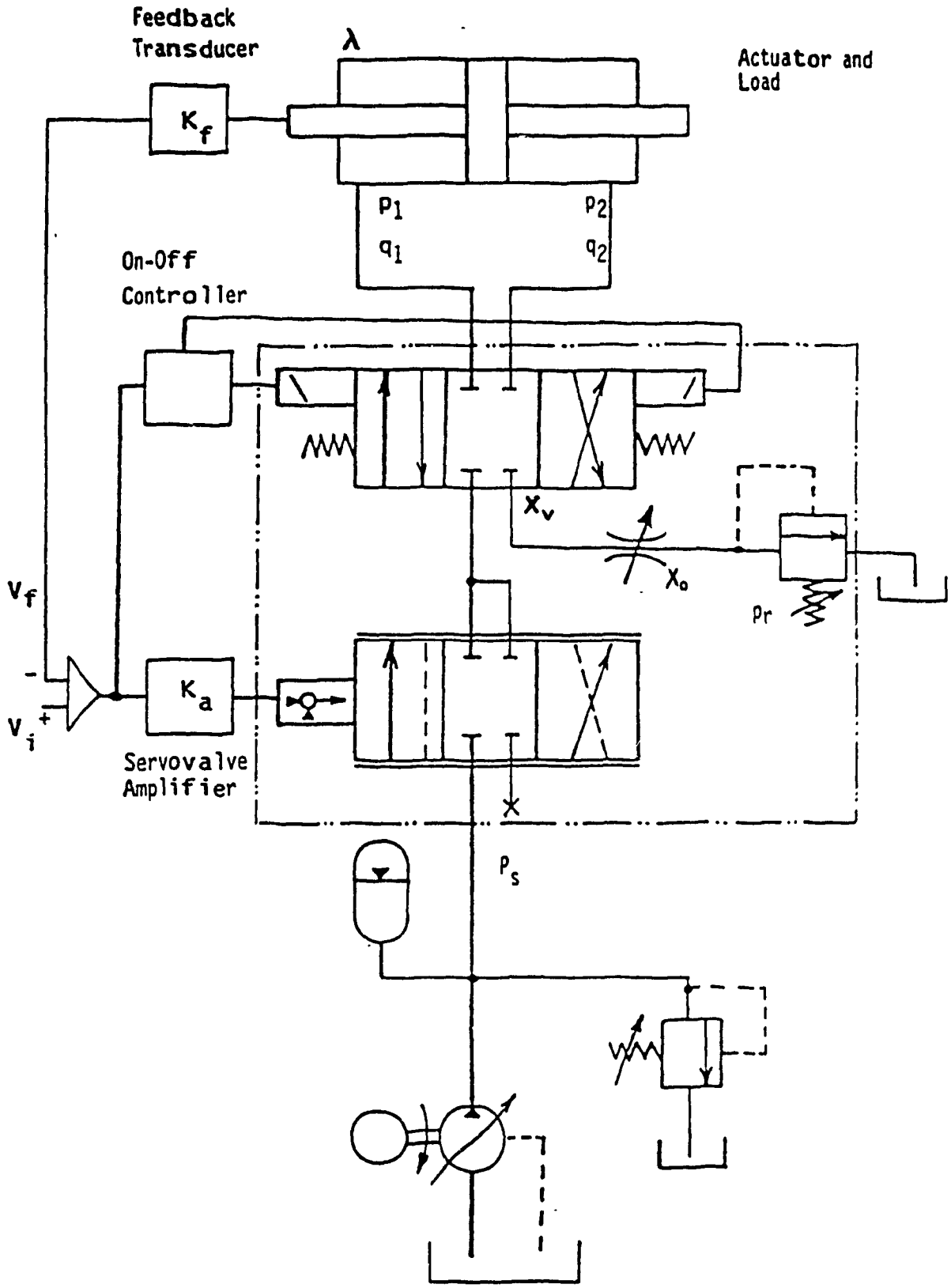

Fig. 1.1 Schematic of Servomechanism with New Servovalve Configuration

compare the characteristics of the conventional and new servovalve configurations under different tuning conditions of the metering and pressure relief valves. The new configuration first exhibited a higher steady state velocity with increase in servovalve opening until coming to a crossing point (Fig. 1.2). This zone up to the crossing point increased as the orifice area was increased and the back pressure was reduced, and vice versa.

A mathematical model for the transient analysis of the configuration was built and simulated by digital computer. It included the effects of static and dynamic friction acting on the actuator and the time delay effect of the directional control valve. Square wave and 2-step input signals were input to investigate the responses of the configurations. To versify the simulation results, an experimental test stand was built. A linear actuator was connected to a moving platform, on which masses could be placed so that the inertia of the moving parts could be changed. Quick switching between conventional and new configurations could be done by switching the 6 manual on-off valves in appropriate locations of the pipings. They were tested under 2 step and square wave inputs on the experimental test rig. The simulation and experimentation results can be summarized as below :

For the new servovalve configuration,

a) as the orifice size is reduced,

i) the damping is increased and the steady state velocity is

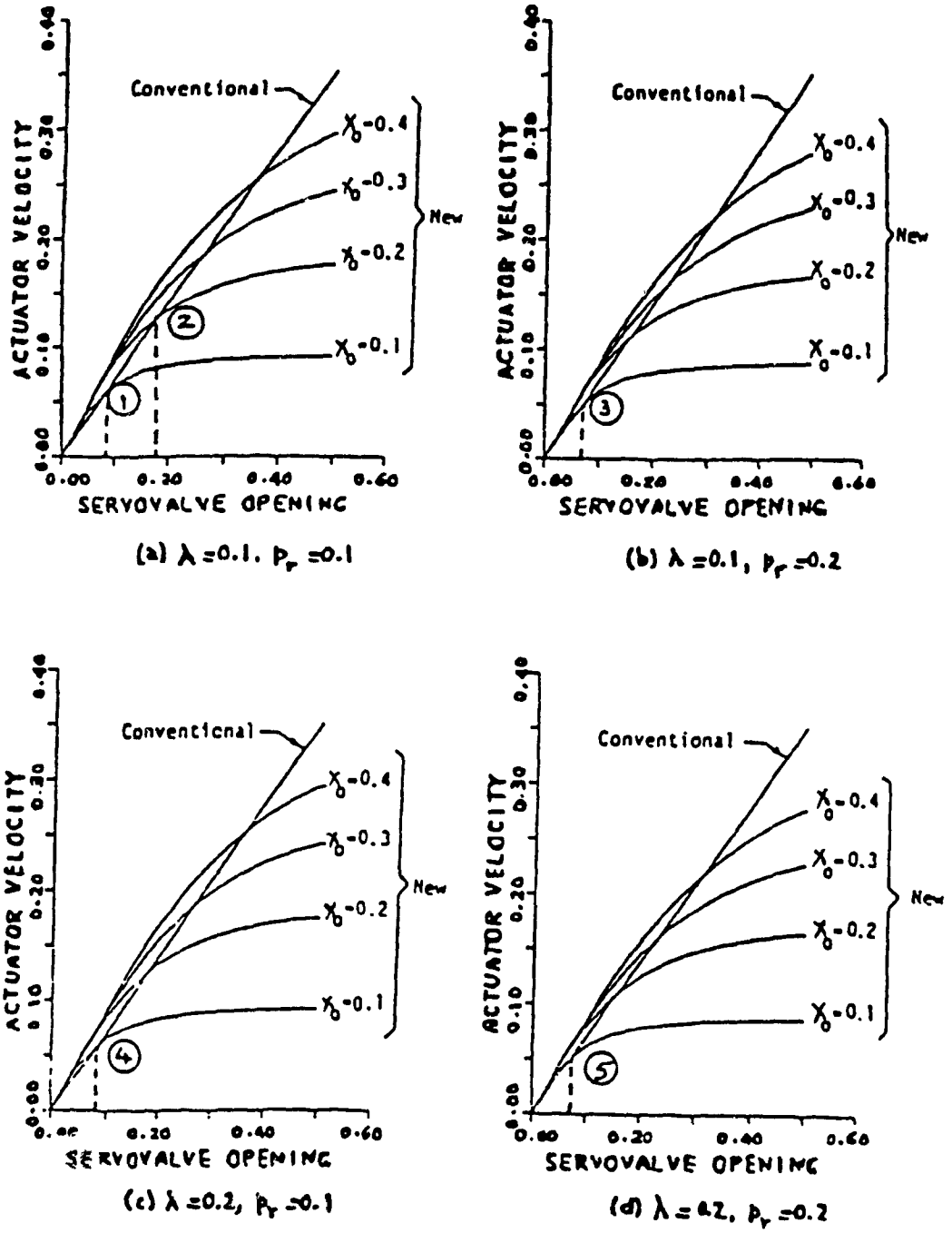

(a) $\lambda = 0.1$, $P_r = 0.1$

(b) $\lambda = 0.1$, $P_r = 0.2$

(c) $\lambda = 0.2$, $P_r = 0.1$

(d) $\lambda = 0.2$, $P_r = 0.2$

Fig. 1.2 Steady State Velocity Characteristics

reduced.

ii) there is no appreciable change in the rise time and the damped natural frequency.

b) as the back pressure is increased,

i) the percentage overshoot is reduced and there is some reduction in settling time.

ii) the steady state velocity is reduced.

iii) the effect of relief valve dynamics is more significant in the experimentation.

The comparison of the conventional and the new servovalve shows that,

i) the new servovalve offers a higher steady state velocity and higher damping under similar input conditions if the metering and back pressure relief valves were properly tuned.

ii) the damping of the system depends on the size of the orifice. Increase in the back pressure reduces the percentage overshoot.

iii) the system with conventional servovalve has lower rise time and higher damped natural frequency than that with the new servovalve.

The comparison of experimental and the simulation result showed that

the mathematical model was a good guide to predict the transient responses.

A design procedure from four different sets of system parameters was studied by computer simulation. It showed that the satisfactory results could be obtained if the ratio of the metering orifice area to the servovalve area was greater than 1.5, and the ratio of the back pressure to the supply pressure was less than 2.0. A procedure was also described to determine the tuning parameters for the new servovalve so that the system could be run in the operating zone to obtain the advantageous results in the new configuration.

1.5 Scope of Research Work

This research work is the extension of the previous research work by A. Limaye [13]. In order to remove the disadvantages from his setup with the linear actuator, a new setup using rotary actuator has been built. A hydraulic loading circuit is added onto the shaft to study the steady state torque-speed characteristics of the motor-pump combination. Experimentations are carried out to see if the conditions of higher gain and lower overshoot can still exist in the dynamic responses of the new configuration. A non-dimensional model for open loop frequency response of the unloaded system is simulated and compared with the non-dimensionalised experimental results. Finally, a design procedure is proposed to find out the boundary of the restrictor area and back pressure, together with the change of the damped natural frequency. A paper has been submitted [30] containing the abstract of the work

done in this research.

The first chapter briefly describes the application and development of servovalves as a high power controlling element. Its literature survey covers some articles on the servovalve and servosystem characteristics, sensitivity and non-dimensional analyses. It reviews the previous work on the servovalve configurations of a linear actuator servosystem.

The second chapter gives the disadvantages of previous setup and describes the design of the new setup. In the new design, the driving unit consists of the power unit, the servosystem and the components along the shaft. The loading unit consists of the inertial loading on the rotating parts and the hydraulic loading circuit. The latter of which uses a servovalve to restrict the flow of the oil through the hydraulic loading pump. Some comments on the new setup are finally given.

In the third chapter, the values of the system parameters such as the leakage coefficients, damping coefficient, static and dynamic frictions are evaluated through the results of experimentation. The steady state torque-speed characteristics of the configurations at different inputs and tuning conditions are plotted to investigate their relationship. Finally, the loading pump is removed to find the speed-input current relationship in the no-load condition.

In the fourth chapter, the open loop experimental step responses of

the configurations of the new setup with the loading pump disconnected from the shaft are carried out. The input signals include the square wave and two step inputs. It is attempted to show that the new configuration can give the higher gain and lower overshoot at some selected input and tuning conditions.

In the fifth chapter, the nondimensional formulation and simulation of the open loop frequency responses of the configurations are given. Bode diagrams are plotted from the simulation to find out the steady state velocity gain, damping ratio, order of the transfer function and damped natural frequency of the system at different input, tuning and loading conditions. It also provides the method of conversion of the experimental physical parameters into dimensionless parameters.

Chapter six shows the comparison of the experimentation and simulation results at different offset levels, restrictor area and relief valve settings for the open loop frequency responses. The experimental results are non-dimensionalised first and then compared with the non-dimensional simulation results in order to verify the model. Explanations are given for the discrepancies found in the comparison.

In the seventh chapter, a design procedure is proposed from computation to find the boundary values of restrictor area and back pressure setting in order to obtain the higher gain and lower overshoot in the new configuration. The change of values of the damped natural frequencies are also found on the boundary.

Chapter eight gives the conclusion of this research and proposal for the future research work.

CHAPTER 2

DESCRIPTION OF EXPERIMENATL SETUP

2.1 Introduction

In the previous work by A. Limaye [13], a test stand was designed to investigate the transient responses of the conventional and new configurations of a hydraulic linear motion system. On-off valves and a directional control valve were located on the tubings for the switching of the configurations. In the new configuration, the two control ports of the servovalve were joined together and the return line was blocked. A restrictor and a relief valve were located at the return line of the directional control valve. Weights could be loaded on a movable platform attached to the piston of the cylinder to change the inertia of the moving parts. There are disadvantages of the system :

1. There was only a limited moving distance of about 9.5 cm. If there were already an initial offset velocity, there could not be enough time to record the output velocity waveform in such a short travelling interval.

2. The volumes in the two chambers and in both configurations were not equal but varying with respect to the displacement of the piston inside the hydraulic cylinder.

3. The effect of external loading force acting on the system could not be investigated from the setup.

A new test stand described in this chapter has been built from the supporting blocks and the platform of the research setup from Alfredo Parra [29]. New components, manifolds, supporting blocks and layout of tubings were purchased or designed. A rotary system is being used so that there can be infinite rotary displacement. The new layout of tubings provides equal volumes in both chambers and both configurations. A hydraulic loading circuit has been designed to exert a constant loading torque on the shaft for the investigation of the steady state torque-speed relationship of the configurations. The schematics of the setup is shown in Fig. 2.1 and the diagram of the hydraulics symbols is shown in Fig. 2.2. Different components are numbered as shown in the figures. The setup can be divided into the driving and loading units. The descriptions and calibrations of some of the components are given in appendix I. Sizing, description and calibration of different components are also given in this chapter and its appendix.

2.2 The Driving Unit of the Setup

The driving unit is divided into : I) the servomotor, II) the tubings and the servovalve, III) the hydraulic power unit and IV) the transmission shaft.

I) The Servomotor

High performance Moog-Donzelli axial-piston servomotor (1) is used. Moog servovalves of 62, 73 or 760 series can be mounted on the top of the servomotor so that there can be a small compressed oil volume and hence a high hydraulic natural frequency. Intermediate sandwich

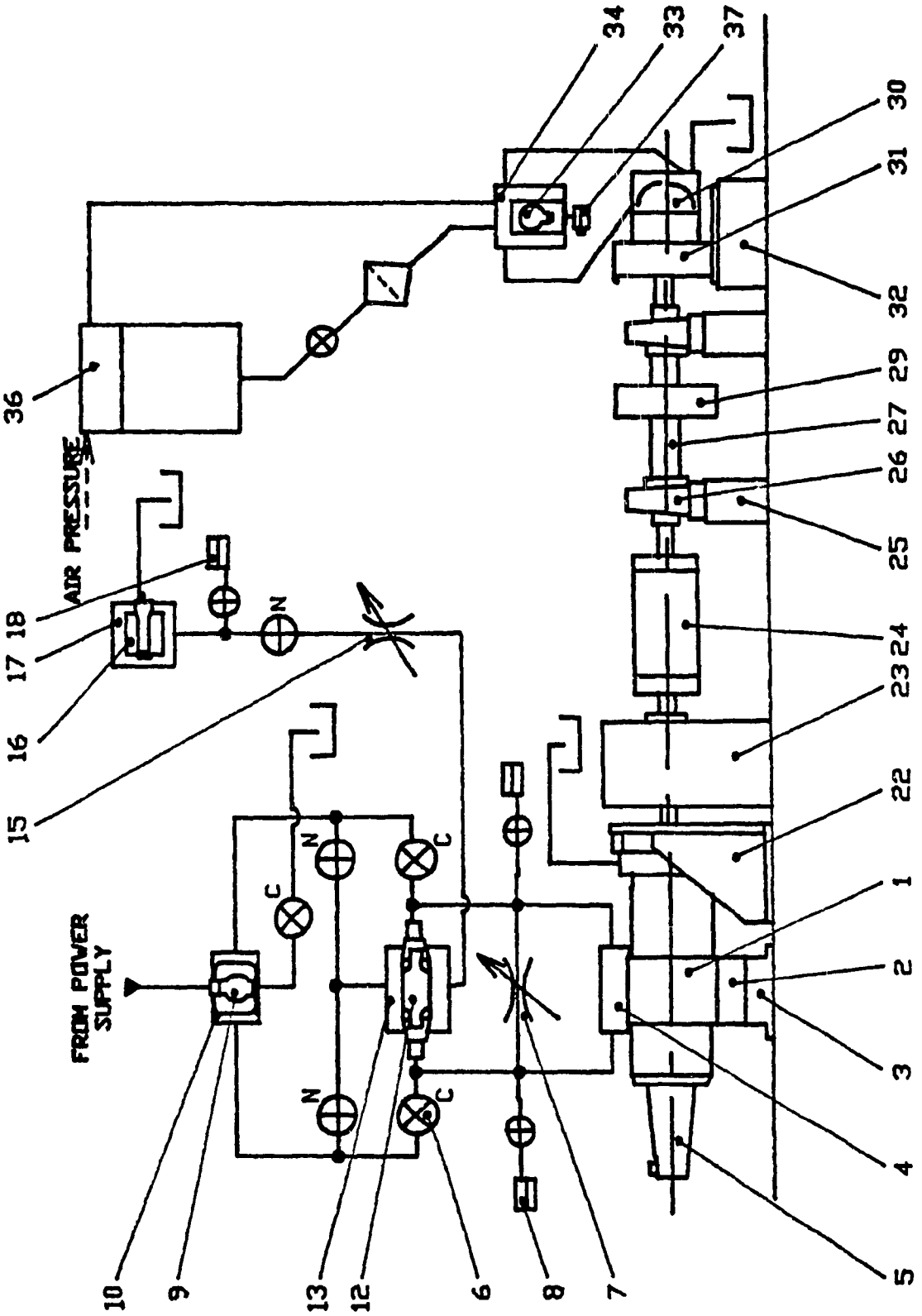

Fig. 2.1 Layout of the Experimental Setup

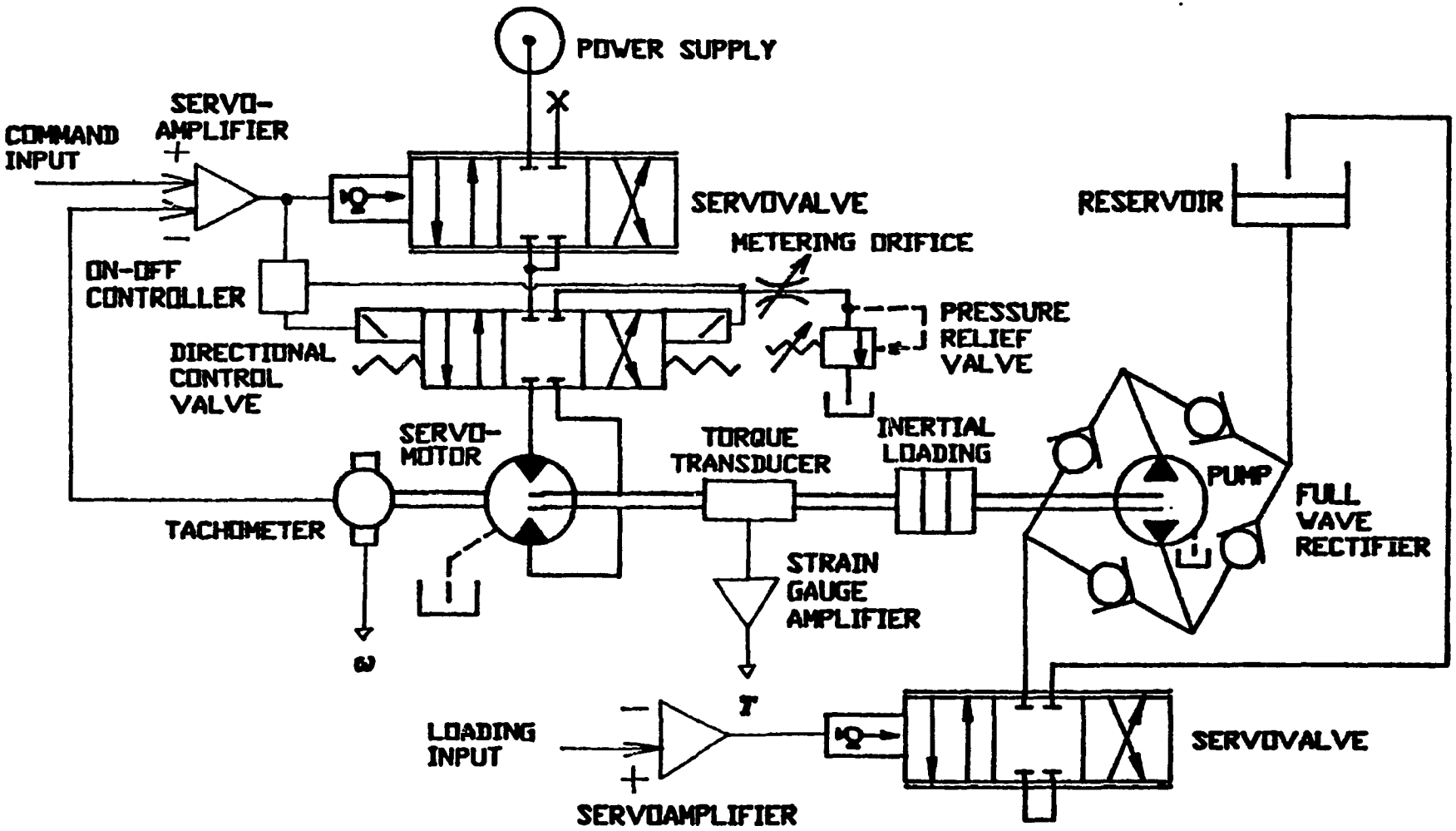

Fig. 2.2 Schematic Diagram Showing the Components of the Experimental Setup

manifolds containing hydraulic accessories such as crossport relief valves or adjustable bypass damping orifice can be included. Supply and return lines can be plumbed to the supply manifold (2) located at the bottom of the servomotor. Internal passages inside the servomotor can lead supply and return fluid to and from the servovalve. In the experimental setup, the supply and return ports of the supply manifold are plugged. The supply manifold is bolted to the platform through a supporting block (3) to have the shaft axis at the exact height of 150mm above the machined surface of the platform. The servovalve is elevated and attached on the vertical framework to provide room for the tubings, which are plumbed to the servomotor through the manifold (4) fixed on top of the servomotor. A tachometer (5) located at the tail of the servomotor outputs signal proportional to the angular speed of the shaft. The signal can be fedback to the servocontroller to provide a closed control loop. Fig. 2.3 shows the block diagram of the system.

II) The Tubings and the Servovalve

Steel tubes are chosen to avoid the inductance effects of flexible tubings on dynamic responses. It is known that the performance of the circuit depends on the resonant frequency of the system, which is inversely proportional to the square root of the volume of the fluid under compression. The basic ideas behind the design of the circuit are :

(a) Equal volumes of compressed oil in both chambers and both configurations so that there is equal natural hydraulic frequency for both cinfigurations and equal dynamics of the system in either direction

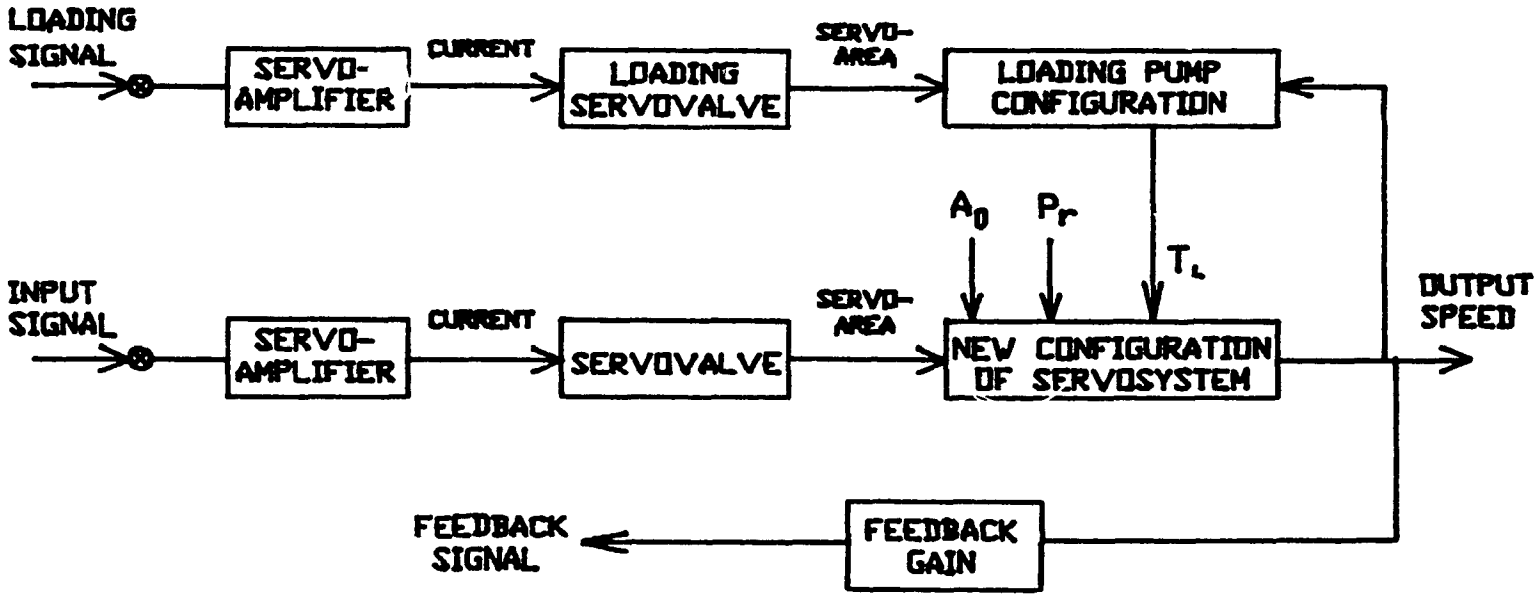

Fig. 2.3 Block Diagram of System

of rotation.

(b) Minimum possible lengths of segments for tubings aside from the unavoidable lengths in the bends, joints and fittings.

(c) Easy switching of configurations and trace of the path of flow of oil from the layout of tubings.

The layout of the tubings is shown in Fig. 2.1. The six half-inch on-off valves (6) determines what configuration the system is under operation. When the C valves are opened and the N valves are closed, it means that the conventional configuration is under operation. The system can be switched to the new configuration by closing the C valves and opening the N valves. The manifold on top of the servomotor directs the oil to the two arms of the tubings. A restrictor (7), which is normally closed, is located across the two ports. If opened, it can introduce cross-port leakage or higher damping to the system. Two pressure transducers (8) with 1000 psi range diaphragms are used to measure the pressures of the ports through the pressure transducer indicators. The Moog 760 servovalve (9) positioned on its manifold (10) receives oil from the supply unit at a supply pressure of 1000 psi. It then directs the oil to either of the two control ports according to the sign of the signal from the Moog Servocontroller (11). The servovalve should be null adjusted by turning the screw on its rear end. Input voltage signal command from dividing the output of a 5V voltage regulator is then amplified by the servocontroller to provide the current to drive the servovalve. Feedback signal from the tachometer and the feedback gain can be connected to the servocontroller to form a closed loop control circuit.

In the new configuration, despite the sign of the input signal, the flow from either port of the servovalve goes to the supply port of the directional control valve (12) through its manifold (13). The sign of the input signal from the pin 4 of the servocontroller, which equals to the sign of the error signal, goes to the on-off controller (14), which directs the 110V a.c. from the mains to the corresponding solenoid of the directional control valve. The flow of oil, after passing through the servomotor, returns to the tank through the restrictor (15) and the back pressure relief valve (16), which is located on its manifold (17). At the same time, the return from the servovalve to the tank is blocked. The calibrations of the restrictor and the relief valve are shown in the Appendix I. A pressure transducer (18) is located immediately before the relief valve to record the back pressure directly. It is noticed that the pressure setting varies slightly with the flow rate and also with the fluctuation of the flow.

All the tubings and manifolds are mounted on a vertical framework built from Unistrut P-330C beams. The framework provides the advantages of the flexibility in mounting and shifting the position of the components, changing the lengths of tubings, repairing and accessing from the back.

III) The Hydraulic Power Unit

The power unit (19), as shown in Fig. 2.4, is modified from the one used in the previous research, which could provide a maximum flowrate of about 3.5 GPM. A new pump is used so that the maximum flowrate is about

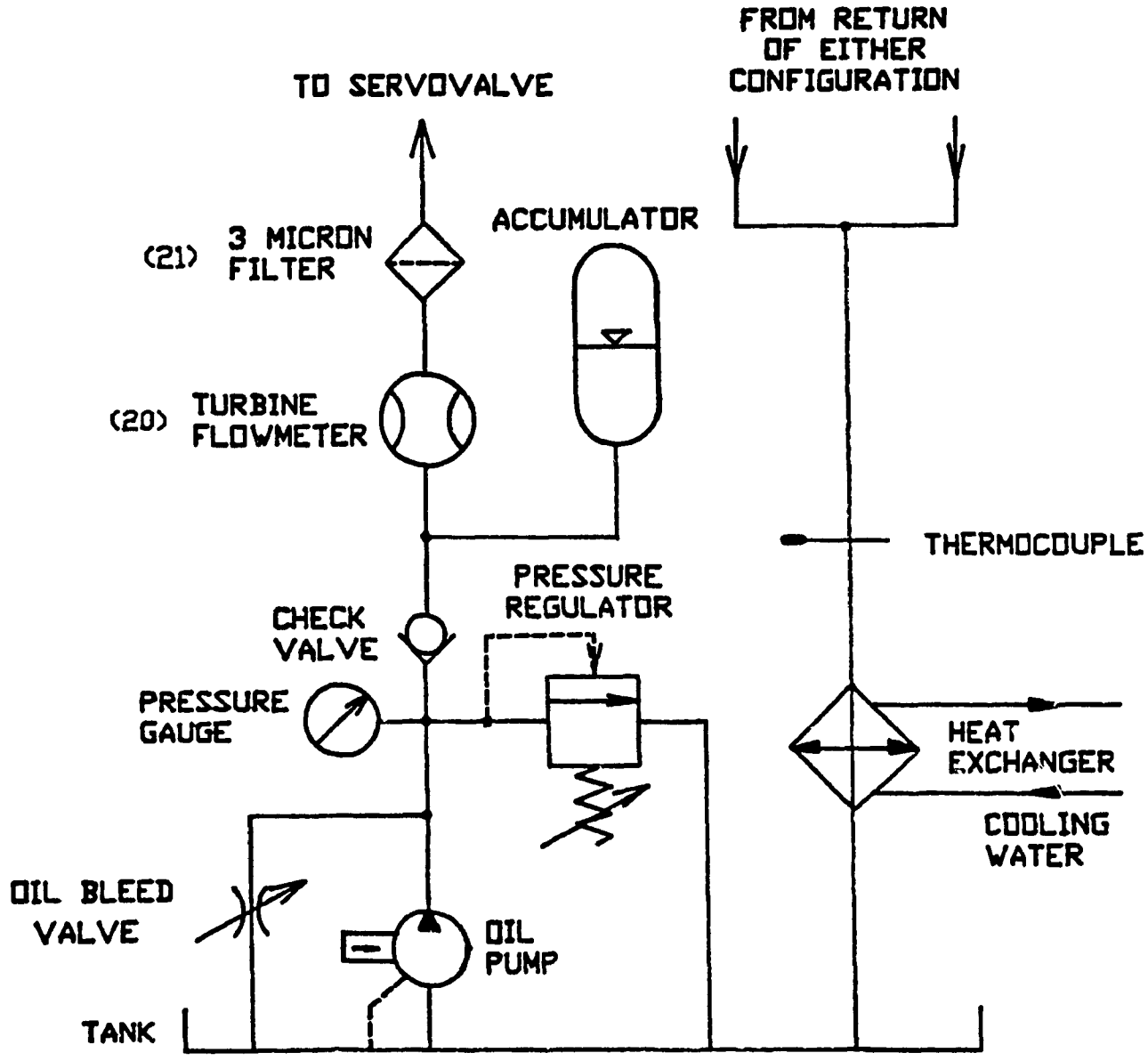

Fig. 2.4 Hydraulic Circuit Diagram for Supply and Return Lines

8 GPM. A restrictor located before the pressure regulator is introduced to bleed the oil to the tank during the starting process. A turbine flowmeter (20) and a high resolution filter of 3 micron (21) are located before the servovalve. The return flow from the servovalve of the servomotor or the relief valve passes through a water cooled heat exchanger before entering the tank. A thermocouple is located before the heat exchanger to monitor the temperature of the oil. The leakage from the servomotor is also drained back to the tank.

IV) Components along the Axis of the Shaft

No flexible couplings of components is used along the shaft so that there is no backlash when there is a change in the direction of rotation. Such design can avoid excessive wear and shock excessive wear and shock loading from torque reversals, and eliminate the pure time delay. Better dynamic responses are resulted although precise machining and alignment are required.

The servomotor is fixed on its bracket (22). It is then followed by three bearings supporting the shafts along the axis. The bearing of mounting (23) serves as an adaptor for the shafts of the servomotor and the torque transducer (24). The two pairs of pillow blocks (25) and bearings (26) support the transmission shaft (27) which is coupled to the shafts of the transducer and the loading pump. They are high speed and low friction bearings so that the viscous frictional torque acting on the system is small. The torque transducer is held in position by a piece of rod connected to its fixing ring and has its output amplified by a strain gauge amplifier (28). The electronic circuit diagrams of

the controllers and signal amplifiers are given in Appendix II.

2.3 The Loading System

The loading systems consists of : I) the inertial load and II) the hydraulic loading circuit.

I) The Inertial Load

Steel discs (29) made up of two halves can be bolted together and clamped on the transmission shaft by means of the key and keyway. They can change the inertia and hence the natural undamped frequency and the damping ratio of the system. To ensure safety, all the rotating parts are covered by a metal shield during experimentation to ensure safety. The size and length of the bolts were carefully calculated according to the forces acting on the halves when the shaft is running at high velocity.

II) The Hydraulic Loading Circuit

The idea of using a mechanical brake to apply a frictional torque on the transmission shaft is discarded to avoid the problem of immense heat generated by the work done of the friction. The bi-directional Volvo hydraulic pump (30) connected to the transmission shaft is fixed on the bracket (31) on top of the supporting block (32). The Moog 73 Servovalve (33) is fixed on a specially designed manifold, which acts as a hydraulic full wave rectifier (34). The rectifier ensures that the oil from the reservoir always goes to the pump irrespective of its direction of rotation. The pressurised oil emerged from the rectifier

is then throttled by the servovalve, which receives signal from the servoamplifier (35), before returning to the reservoir (36). The pressure built up across the pump provides the load torque acting on the transmission shaft. The reservoir stores a large amount of oil and has a large heat capacity so that the temperature of the oil goes up only slowly. The reservoir is pressurised to about 6 psi from the air supply in the lab so that the cartridge check valves (each needs about 3 psi to crack open) inside the rectifier manifold are already opened before the pump is started. A pressure transducer (37) with a 3000 psi diaphragm is located before the servovalve to monitor the pressure built up by the pump.

2.4 Sizing of Components and Tubings

The rated flows of the components and sizing of the tubings should match each other in hydraulics circuit design. The following is a list of the rated flows of the components :

Component	Rated Flow (GPM)
Power Supply	8
Servovalve	10 @ 1000 psi
Servomotor	9.3
Directional Control Valve	21
Pressure Relief Valve	8

It can be seen that the rated flows match very well with each. For

the relationship between rated flow and dimension of the tubings, with the rule-of-the-thumb for average flow velocity of 15 feet per second through half inch steel tubes, 11 GPM of flow is allowed without much loss of pressure along straignt tube. Hence, the dimension of the steel tubing has been chosen correctly.

2.5 Conclusion

The new setup is found satisfactory in its performance and has solved the major problems listed in the introduction. However, there are still several minor problems :

1. The switching time delay for the directional controller is about 8 ms.

2. The temperature of the oil goes up very fast when the servomotor runs at high velocity. It is known that the life of oil will be halved if operated for a long time for every 10°C above 60°C and the viscosity of the oil decreases greatly with the temperature. The output reading chosen is hence limited to those at the temperature between 40 and 50°C in order to minimize the error.

3. There was also heating problem of on the bearings supporting the loading shaft after the machine had been running at high speed for a while. Misalignment of the shaft was proved from different torque readings at different shaft angular positions. The problem is minimized by shimming different supporting blocks of components carefully with very thin metal foils.

CHAPTER 3

MEASUREMENT OF SYSTEM PARAMETERS AND STEADY STATE CHARACTERISTICS

3.1 Introduction

The experimental setup was built as described in Chapter 2. The values of the parameters of the components were measured or calibrated as described in Chapter 2 and its Appendix. In this chapter, the values of the system parameters, such as the leakage coefficients, the damping coefficient, the static and dynamic frictions, are evaluated through experiments carried on the system. The steady state torque-speed characteristics of the configurations at different inputs and tuning conditions are plotted to investigate their relationships. Finally, the loading pump is removed to investigate the speed-input current relationship in the no-load condition.

3.2 The Leakage Coefficients

3.2.1 Leakage Coefficients of the Motor

Two types of leakages in the driving unit can exist : the internal leakage (or cross-port leakage) between the control lines and the external leakage from the motor chambers to the case drain. Because all mating clearances in the motor are intentionally made small to reduce losses, the leakage flows are considered laminar.

The internal leakage flow is given by :

$$Q_{im} = C_{im}(P_1 - P_2) \tag{3.1}$$

where C_{im} = internal or cross-port leakage coefficient.

The external leakage in each chamber is proportional to the particular chamber pressure (assuming negligible drain pressure) :

$$Q_{em1} = C_{em1}P_1 \tag{3.2}$$

and $$Q_{em2} = C_{em2}P_2 \tag{3.3}$$

where C_{em} = external leakage coefficient (assuming to be the same in each chamber), (m^3s^{-1}/Nm^{-2}) or (GPM/psi).

The steady-state continuity equation (i.e. without compressibility flow) for the motor chambers are

$$Q_1 - C_{em}P_1 - C_{im}(P_1 - P_2) - D_m\omega = 0 \tag{3.4}$$

and $$D_m\omega + C_{im}(P_1 - P_2) - C_{em}P_2 - Q_2 = 0 \tag{3.5}$$

If there were no leakage at all, then

$$Q_1 = Q_2 = D_m\omega$$

If $C_{em} = 0$ only, then

$$Q_\ell = \frac{Q_1 + Q_2}{2} = Q_1 = Q_2 = D_m\omega + C_{im}(P_1 - P_2)$$

The leakage can affect the damping of the driving unit. They are easily determined by locking the motor shaft and letting the return line be vented to the atmosphere (i.e. $P_2 = 0$). Pressure P_1 is then applied to the forward chamber and the volume of flow per unit time in the return and drain lines are measured by means of a measuring cylinder and a timing stopwatch.

From Fig. 3.1, the slope at at 500 psi, i.e. half of the supply pressure, is taken as the average :

the internal leakage coefficient, $C_{im} = \frac{0.04\text{GPM}}{425\text{psi}}$

$$= 8.816\text{x}10^{-6}\text{m}^{-}\text{s}^{3}/\text{Nm}^{-2}$$

In Fig. 3.2, from the slope of the straight line best fitted to the points :

the external leakage coefficient, $C_{em} = 0.00933$ GPM/1000psi

$$= 8.854\text{x}10^{-14}\ \text{m}^3\text{s}^{-1}/\text{Nm}^{-2}.$$

The external leakage coefficient is found to be about one-tenth of that of the internal leakage. (Note : the internal leakage across the ports of the motor here also includes the leakage across the servovalve,

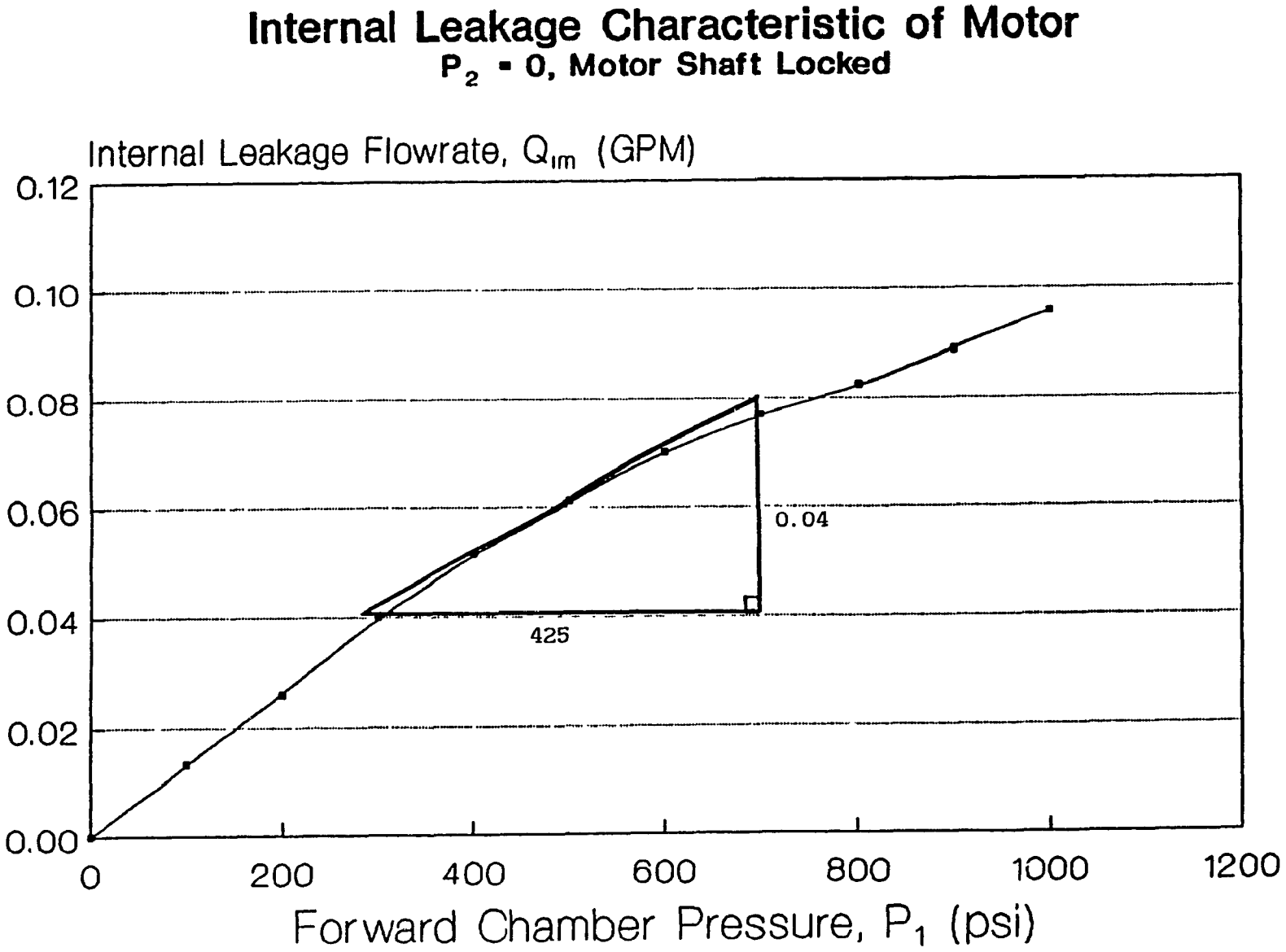

Fig. 3.1 Internal Leakage Characteristics of the Motor

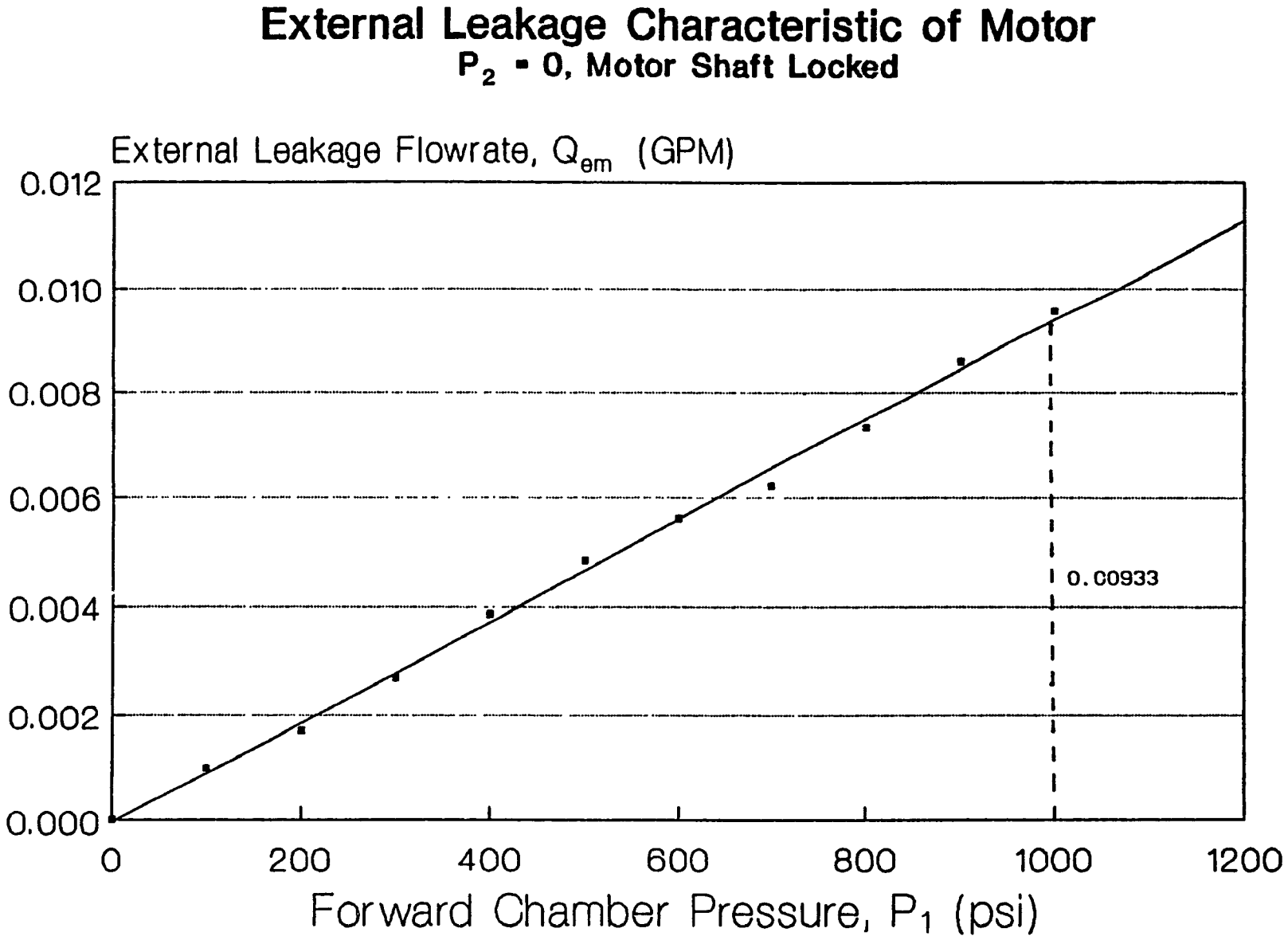

Fig. 3.2 External Leakage Characteristics of the Motor

the directional control valve and the on-off valves. This accounts for why it is 10 times as big as the external leakage.) Hence, the external leakage can be neglected in the later part in the simulation.

The power unit can supply a maximum flow of about 8 GPM. If the pressure difference across the ports were 800 psi, the leakage flow is approximately 0.08 GPM, which accounts for about 1 per cent of the maximum flow. Although the leakage flow is small, it can contribute to some damping effect.

3.2.2 Leakage Loss of the Pump

The Volvo F11C-5 Pump/Motor can work as a motor by connecting it to the oil supply power unit. The shaft is then locked and the pressure at the inlet is measured by the pressure transducer number 4. The pump does not show any internal leakage across the chambers even at a supply pressure of 2500 psi. The internal leakage coefficient of the pump is hence equal tozero. The external leakage is measured by means of a measuring cylinder and a timing stopwatch. From the slope of the graph in Fig. 3.3,

$$\text{the external leakage coefficient, } C_{ep} = \frac{0.0132 \text{ GPM}}{1500\text{psi}}$$

$$= \frac{0.0088 \text{ GPM}}{1000\text{psi}}$$

$$= 8.050\text{x}10^{-14}\text{m}^3\text{s}^{-1}/\text{Nm}^{-2}.$$

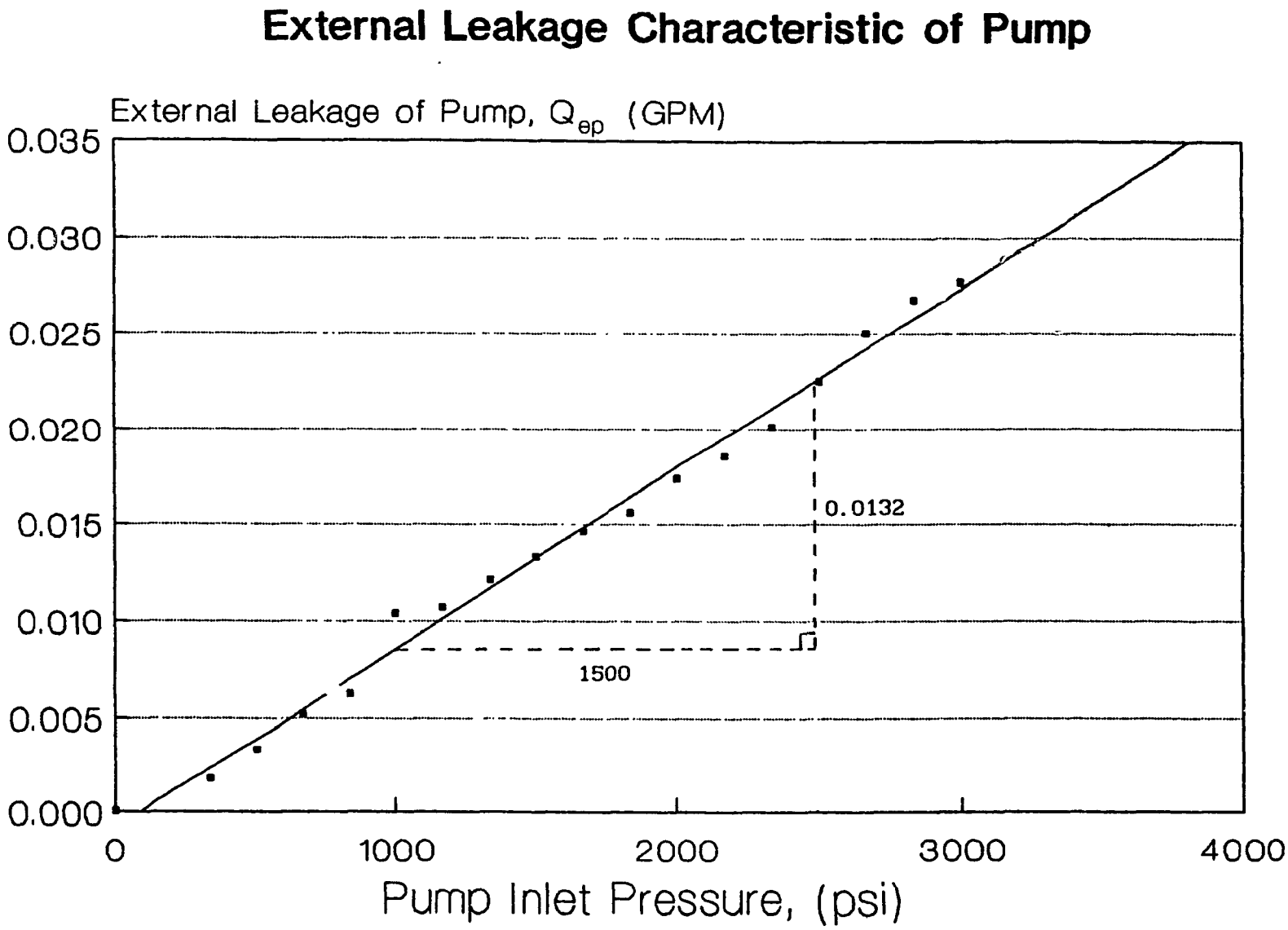

Fig. 3.3 Calibration Curve for the External Leakage of Pump

3.3 Torque Losses in the System

For a motor, the ideal generated torque is

$$T_g = D_m(P_1 - P_2) \tag{3.6}$$

There are at least three sources of torque losses which detract from the generated torque :

1. Damping torque

$$T_d = B\omega = C_D D_m \mu \omega \tag{3.7}$$

where $B = C_D D_m \mu$ = viscous damping coefficient, (Nms)

C_D = dimensionless damping coefficient,

μ = absolute viscosity of oil (Nsm^{-2}).

It is caused by shearing of the fluid in the small clearances between mechanical elements in relative motion.

2. Dynamic friction torque

It opposes the motion of piston in its bore and occurring in loaded motor elements, such as bearings. It is proportional to the sum of pressures in both chambers.

$$T_f = \frac{\omega}{|\omega|} C_f D_m (P_1 + P_2) \tag{3.8}$$

where C_f = dynamic internal friction coefficient.

Or, at the time of starting from still, the static internal frictional torque,

$$T_f = \frac{\omega}{|\omega|} C_{fs} D_m (P_1 + P_2) \qquad (3.9)$$

where C_{fs} = static internal friction coefficient.

3. Static and dynamic frictional torque

Static and dynamic frictional torques are given by $\frac{\omega}{|\omega|} T_{cs}$ and $\frac{\omega}{|\omega|} T_c$ respectively.

In overall, the net torque delivered to the load on the rotating shaft is

$$T_L = D_m (P_1 - P_2) - C_D D_m \mu\omega - \frac{\omega}{|\omega|} C_f D_m (P_1 + P_2) - \frac{\omega}{|\omega|} T_c \qquad (3.10)$$

3.3.1 To Determine C_f, C_{fs}, T_c and T_{cs}

To measure the frictional torques of the servomotor-loading pump combination, the pump is unloaded by cutting off its supply of oil so that no work is used in pumping the oil.

The operation is then switched to the new configuration and the

servovalve of the motor was fully opened. At different pressure levels of supply pressure from the power unit, the back pressure of the return line was varied by adjusting the pressure relief valve to record the pressures P_1 and P_2 at the moment that the rotation just ceased from running (for dynamic friction) and the shaft just started rotation from still (for static friction).

From Eq. (3.10), when the shaft just ceased from running, then $\omega = 0$ and $T_L = 0$.

$$D_m(P_1 - P_2) = C_f D_m(P_1 + P_2) + T_c$$

$$D_m(P_1 - P_2) - C_f D_m(P_1 - P_2) = 2C_f D_m P_2 + T_c$$

$$P_1 - P_2 = \frac{2C_f}{1 - C_f} P_2 + \frac{T_c}{D_m(1 - C_f)} \qquad (3.11)$$

By plotting $(P_1 - P_2)$ against P_2 for the dynamic friction, the slope of the graph gives the value $\frac{2C_f}{1 - C_f}$ while the y-intercept gives the value $\frac{T_c}{D_m(1 - C_f)}$.

From Fig. 3.4,

$$\text{slope} = \frac{2C_f}{1 - C_f} = \frac{30}{485}, \quad \text{giving} \quad C_f = 0.03$$

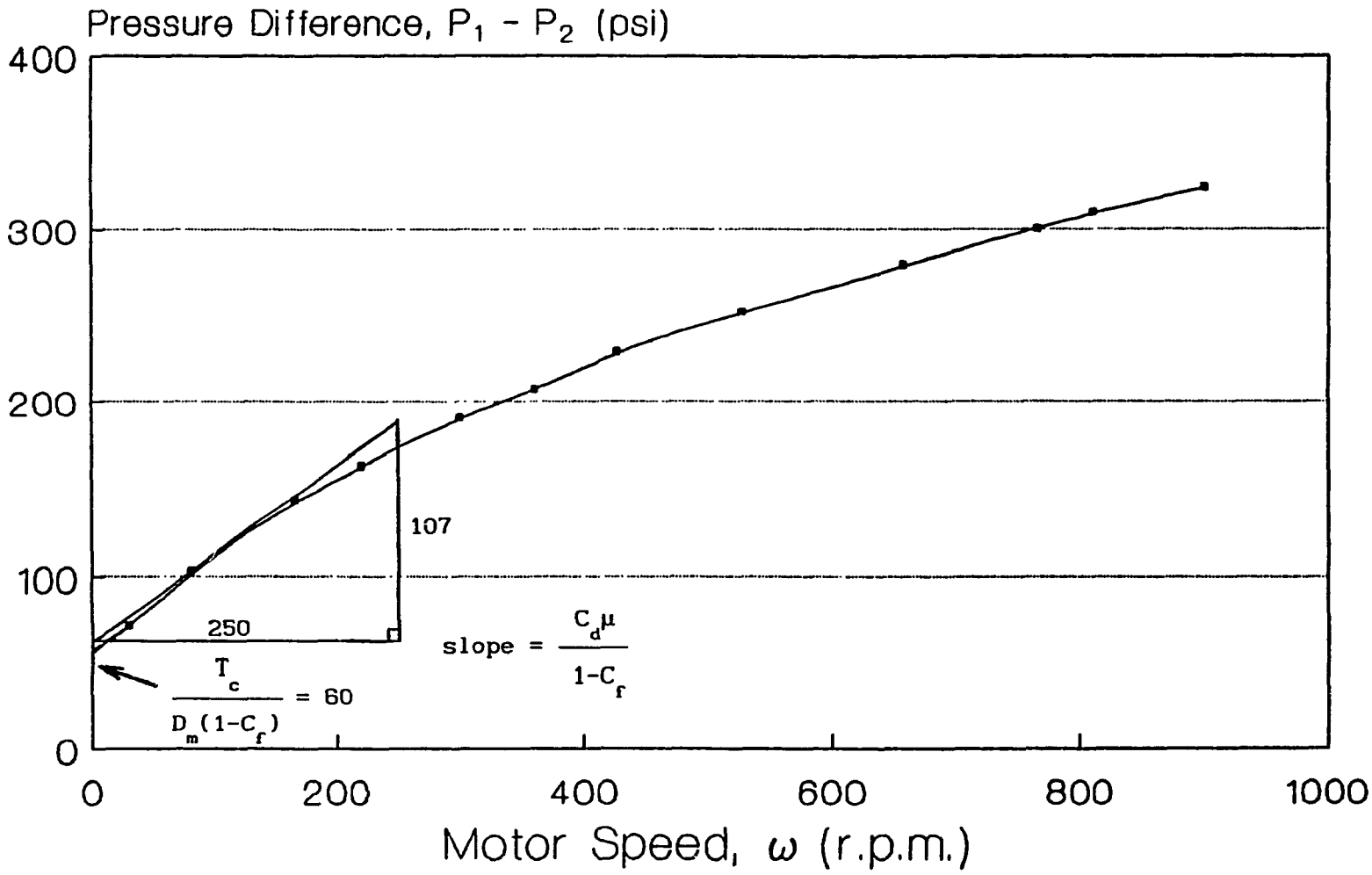

Fig. 3.4 Graph of Pressure Difference against Speed with No Load on Motor and $P_2 \propto 0$

As the y-intercept = 60 psi,

$$T_c = D_m(1 - C_f)(P_1 - P_2)_{P_2 = 0} = 1.12 \text{ Nm}$$

Assume $P_1 + P_2 = P_s = 1000$ psi,

$$T_f = 0.58 \text{ Nm.}$$

T_f is usually neglected to simplify the equations.

To measure the starting friction, the slope of the graph $P_1 - P_2$ plotted against P_2 at the starting point is measured :

$$\text{slope} = \frac{2C_{fs}}{1 - C_{fs}} = \frac{41}{267} = C_{fs} = 0.071.$$

As the y-intercept = 92 psi,

$$T_{cs} = D_m(1 - C_{fs})(P_1 - P_2)_{P_2 = 0} = 1.65 \text{ Nm.}$$

The values calculated above are not very accurate because it is very difficult to judge when the motor has just started or stopped.

3.3.2 To Measure the Damping Torque Loss

The damping torque loss, which depends on the speed ofrotation, are found by measuring the forward pressure, P_1, required to run the unloaded motor at various speeds with negligible return pressure (i.e.

$P_2 = 0$).

Putting $P_2 = 0$ in (3.10) and $T_L = 0$,

$$0 = D_m P_1 - C_D D_m \mu\omega - C_f D_m P_1 - T_c$$

$$P_1 = \frac{C_D\mu}{1 - C_f}\omega + \frac{T_c}{1 - C_f} \qquad (3.12)$$

From the slope of the graph in Fig. 3.5,

$$\text{slope} = \frac{C_D\mu}{1 - C_D} = \frac{107\text{x}6894.4}{250\text{x}\frac{2\pi}{60}}$$

$$C_D\mu = 28178\text{x}(1 - 0.03) = 27332 \text{ Nsm}^{-2}$$

$$B = C_D\mu D_m = 27332\text{x}2.802\text{x}10^{-6} = 0.0766 \text{ Nms}$$

3.4 Torque-Speed Relationship

The torque-speed relationships of the motor-pump setup are plotted at different current inputs to the servovalves controlling the flows to the motor and pump. The servocontrollers are open-looped so that the currents, which are proportional to the voltage input signal, are the input parameters and the values of which range from 0 to 10 mA.

In Fig. 3.6, the torque-speed distribution characteristics of the

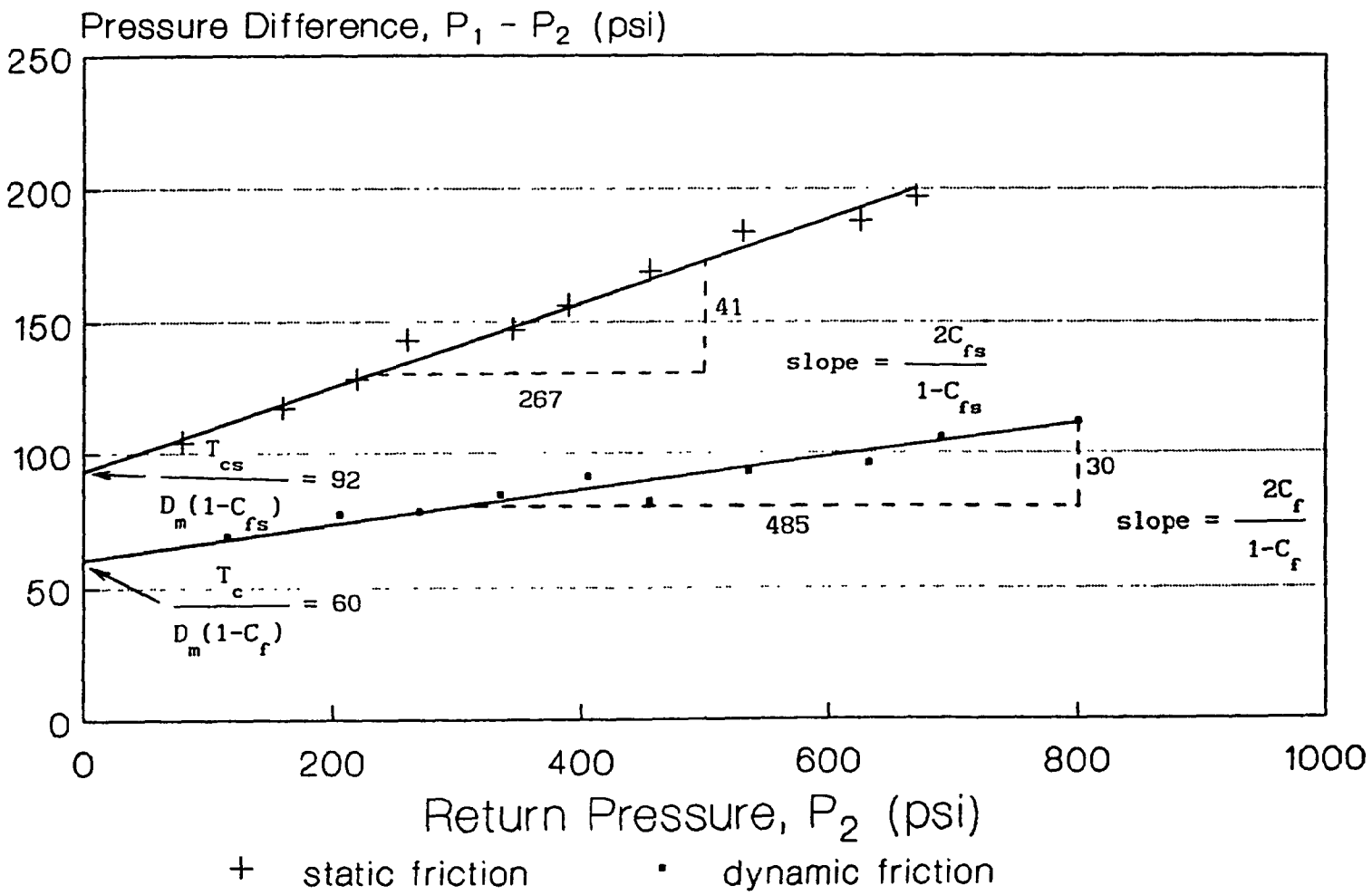

Fig. 3.5 Static and Dynamic Friction Characteristics of Pump and Motor Combination

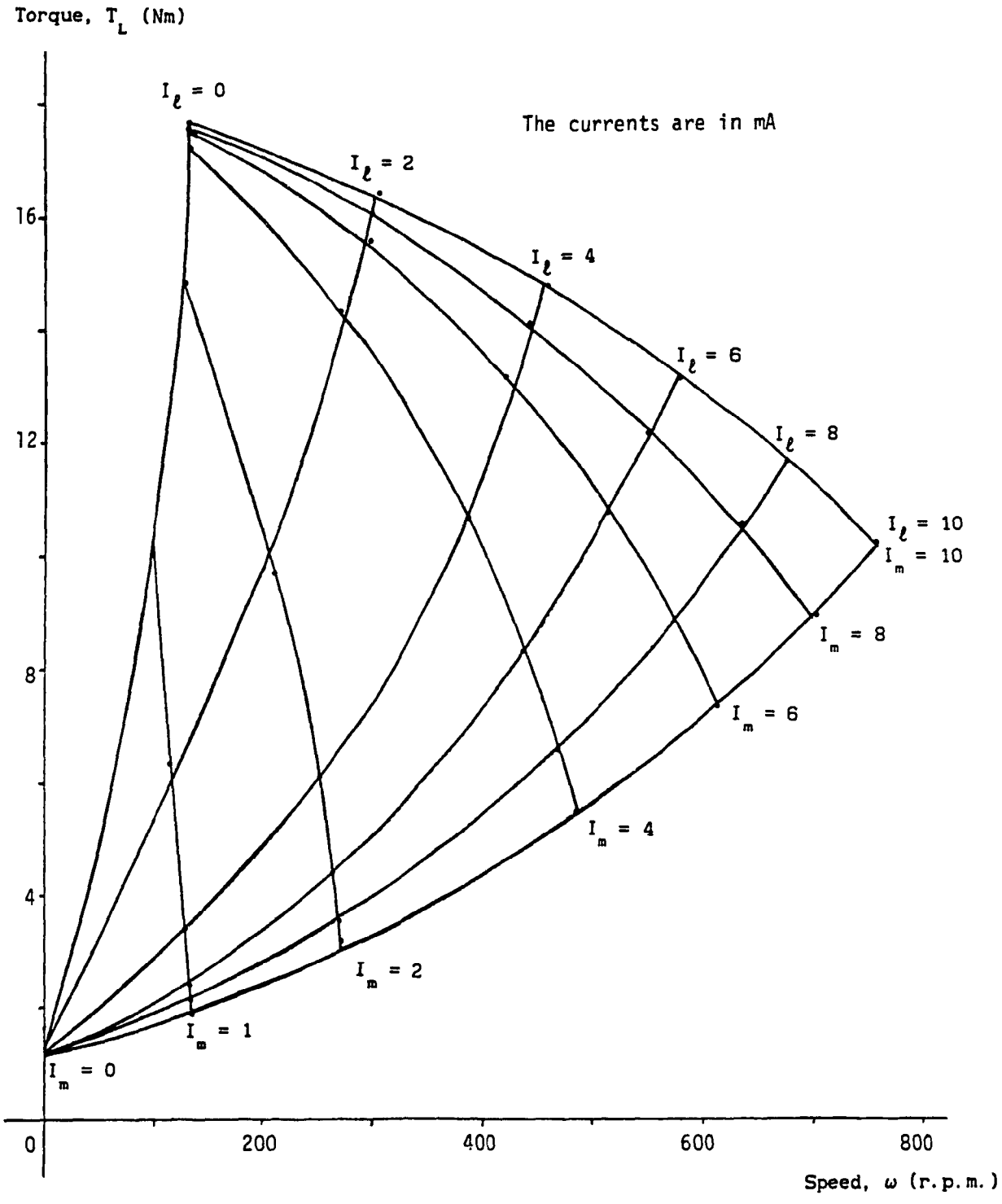

Fig. 3.6 Torque-Speed Relationships of the Motor-Pump Setup at different current inputs (conventional configuration)

conventional configuration form a web from different input current values. The intercept on the y-axis for $I_m = 0$ equals to the dynamic friction of the system after it has started moving from zero velocity. When the current input to the servovalve of the motor increases from zero to 10 mA, the curves convex upwards and converge. If the input were above 10 mA, the curves will converge very fast and become crowded together. Hence the curves above 10mA are not shown in the figure. When the current to the servovalve of the loading pump is zero, the shaft can still rotate under high loading torque because the hydraulic oil is forced across the pump and its servovalve through the internal leakage. The torque and speed increase at constant I_ℓ when I_m increases. An increase in I_ℓ at constant I_m gives higher speed but lower torque. When I_ℓ increases, the curves converge. If I_ℓ is larger than 10 mA, the curves will converge very fast also.

In the new configuration, a comparison of the characteristic at different return orifice areas with a constant back pressure can be seen from comparisons between Fig. 3.7 and 3.9, or between Fig. 3.8 and 3.10. An decrease in orifice area cause the web to shrink towards the origin. Similarly, the increase of pressure from the value in Fig. 3.7 to 3.8 or Fig. 3.9 to 4.0 causes the web to shrink towards the origin also.

The conventional and new configurations can be compared Fig. 3.6 and 3.9. At I_m input of below 3 mA, the output speed ω is larger in the new configuration unless the input current I_ℓ to the loading is less than about 3 mA. At input I_m values of greater than 3 mA, the output speed ω is generally smaller in the new configuration. For smaller orifice area

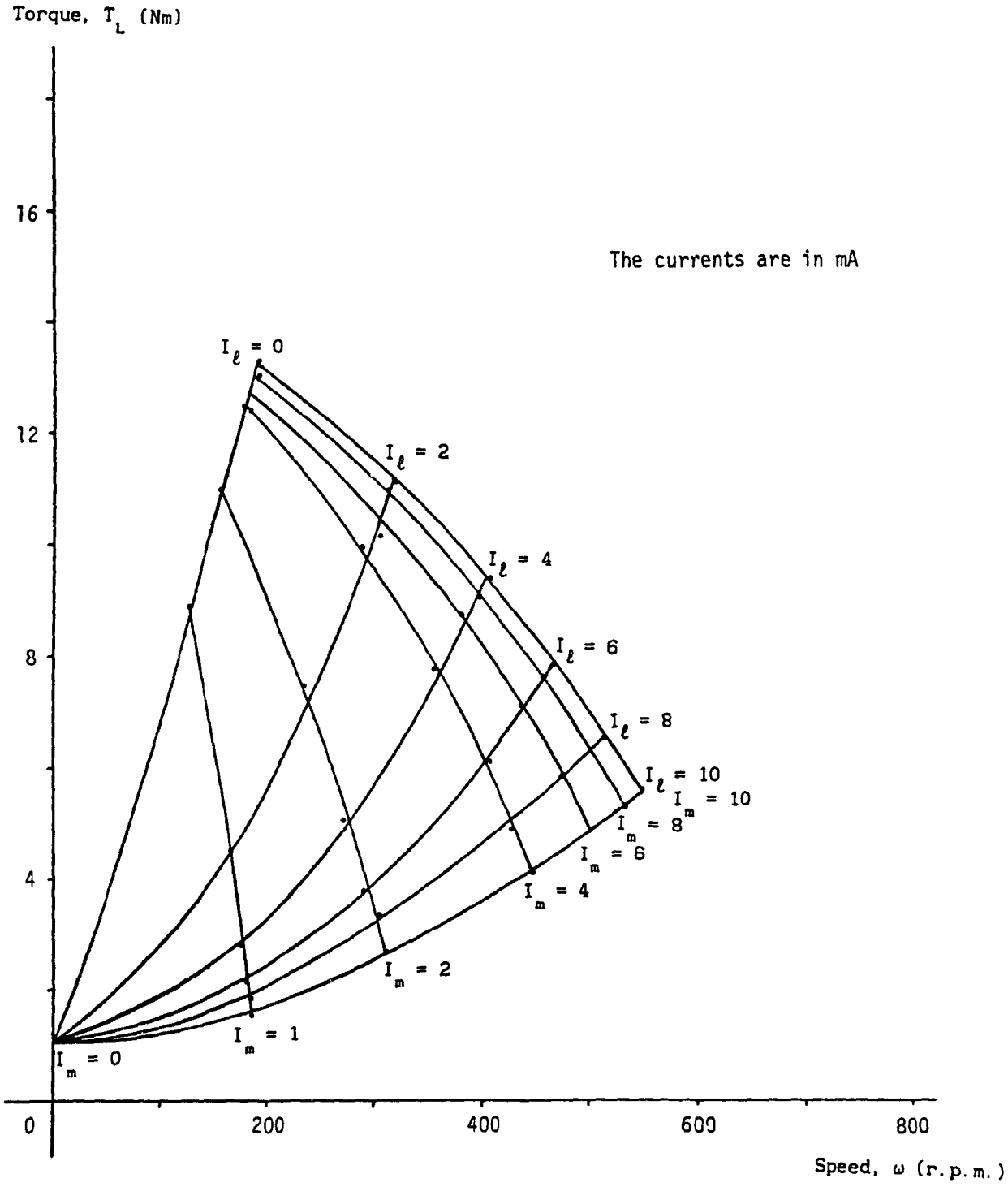

Fig. 3.7 Torque-Speed Relationships of the Motor-Pump Setup at different current inputs (new configuration : A_0 = 3.3 turns open, P_r = 150 psi)

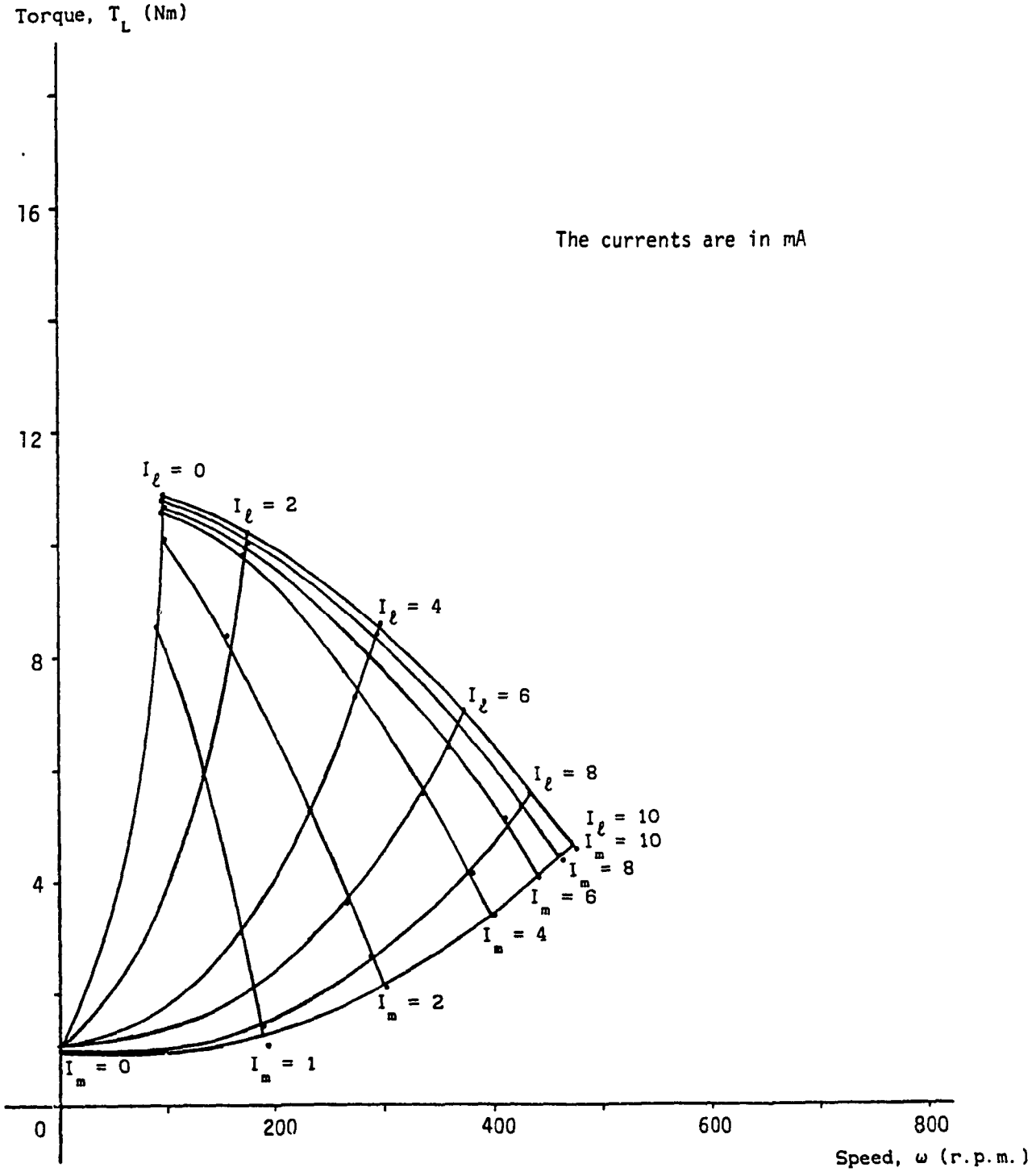

Fig. 3.8 Torque-Speed Relationships of the Motor-Pump Setup at different current inputs (new configuration : A_0 = 3.3 turns open, P_r = 300 psi)

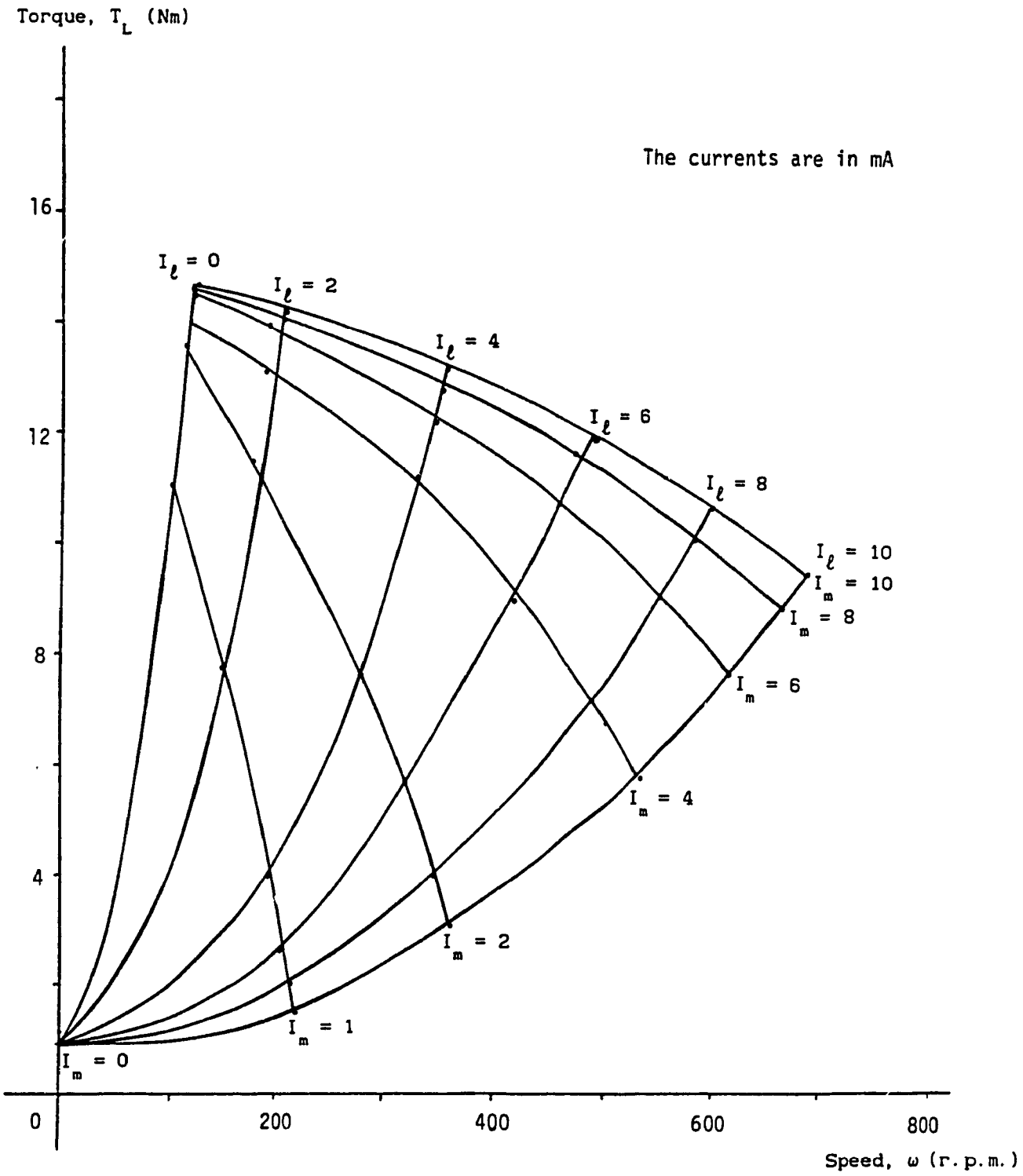

Fig. 3.9 Torque-Speed Relationships of the Motor-Pump Setup at different current inputs (new configuration : A_0 = 6.875 turns open, P_r = 150 psi)

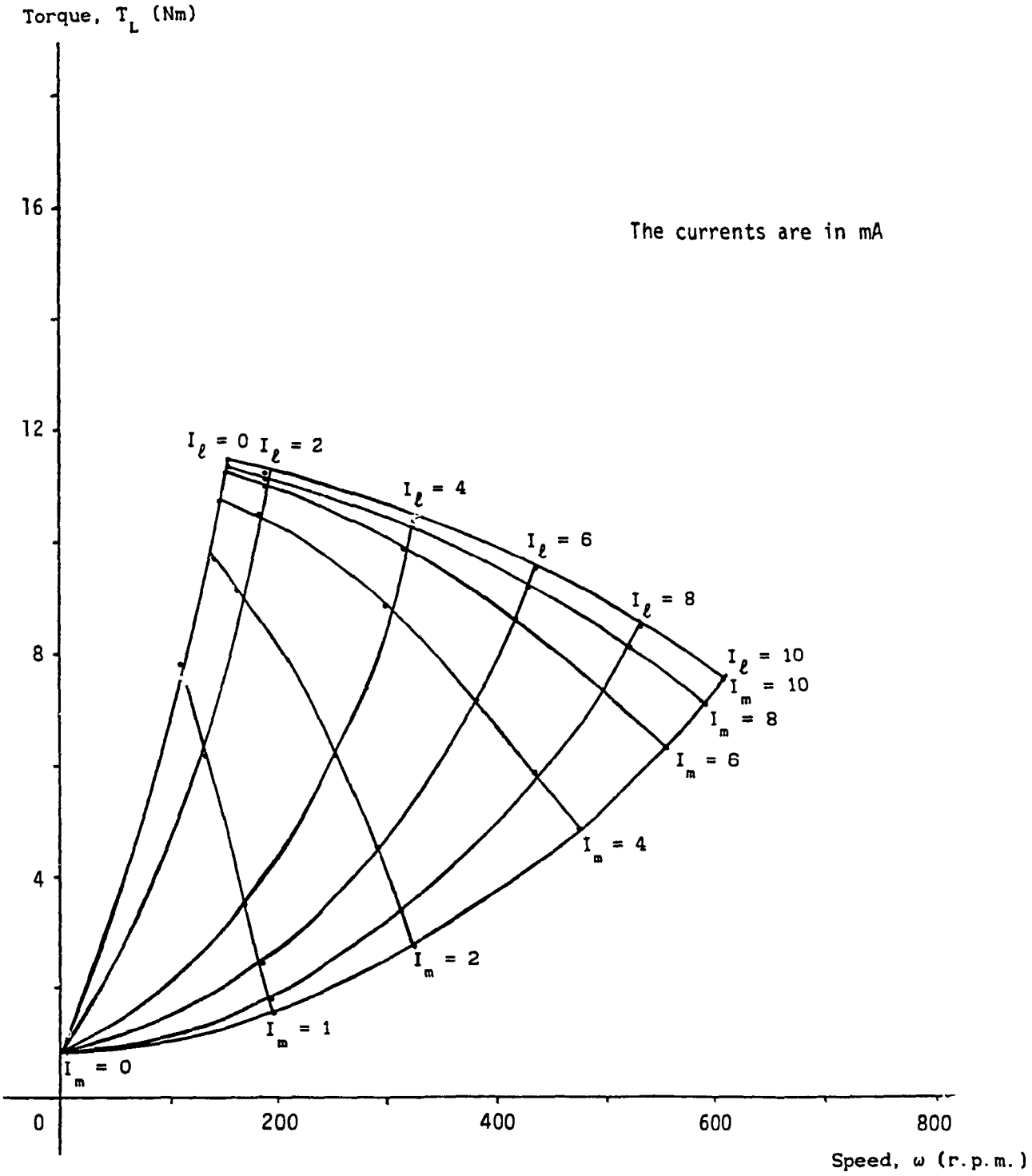

Fig. 3.10 Torque-Speed Relationships of the Motor-Pump Setup at different current inputs (new configuration : A_o = 6.875 turns open, P_r = 300 psi)

or larger back pressure, the value of I_m for a larger output speed in the new configuration becomes smaller.

It can be shown that there exists a larger velocity output from the same input current or loading current in the new configuration. Such region is good for I_m being small, orifice area large and back pressure small.

3.5 Steady State Characteristics with Loading Pump Removed

The loading pump is removed from the shaft because the loading system cannot provide a constant loading torque even though the loop is closed by negatively feeding the velocity signal back to the servocontroller. The steady state speed-input current characteristics with the loading pump removed are shown in Fig. 3.11 and 3.12. The conventional configuration are plotted with new configuration at different tuning conditions. It can be seen that the velocity increases with a decreasing slope for both configurations. The new configuration starts with a larger slope than the conventional configuration. However, the slope decreases in a faster rate than that of the conventional configuration, causing an intersection point. The region before the intersection point in the new configuration gives a larger output velocity. With a decrease of restrictor area or an increase in back pressure, the curves of the new configuration drop, giving a smaller region for the higher velocity output. The results conform with the simulation results given in the thesis by Limaye [13].

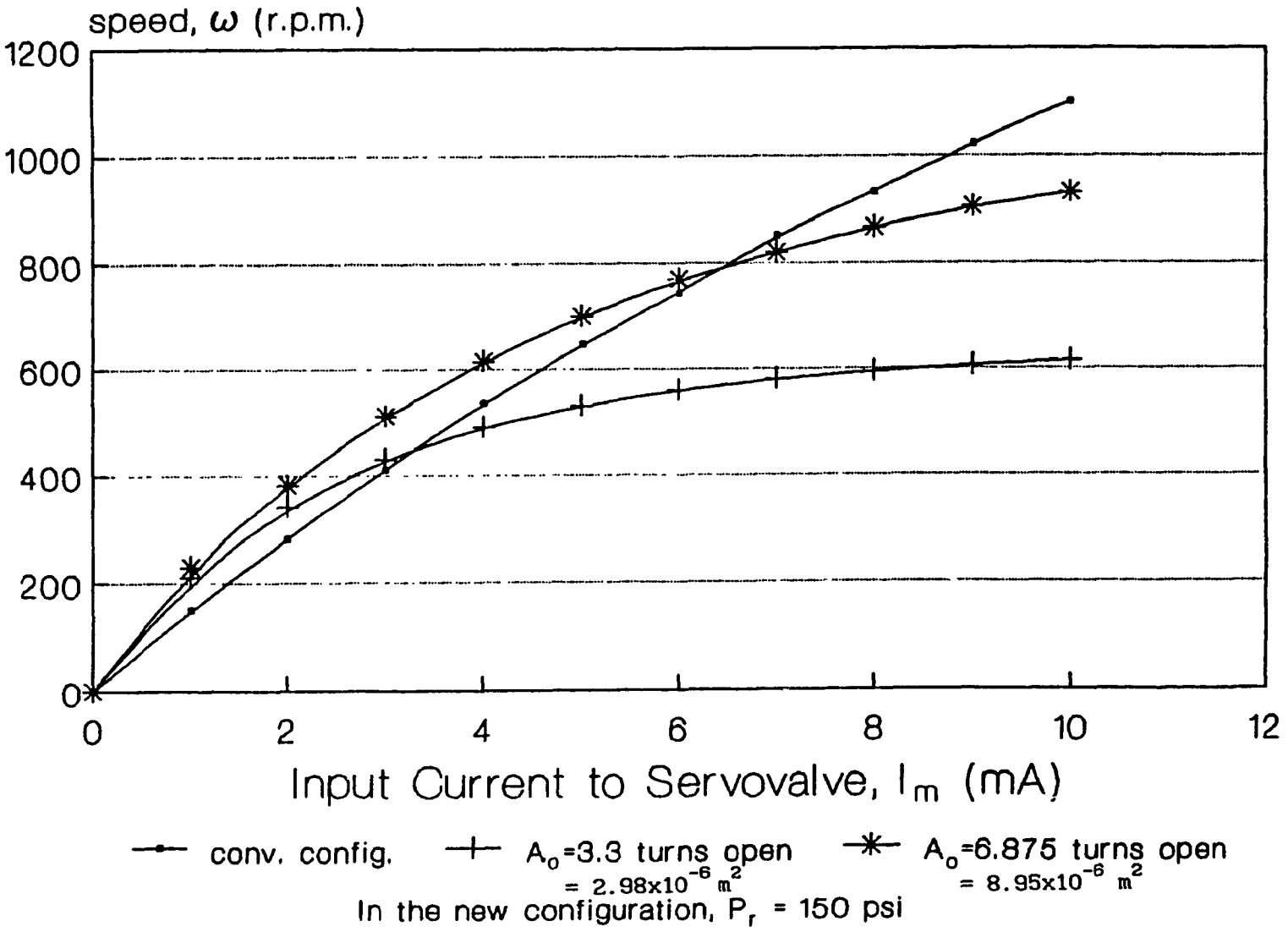

Fig. 3.11 Steady State Speed-Input Current Characteristics with Loading Pump Removed (P_r = 150 psi)

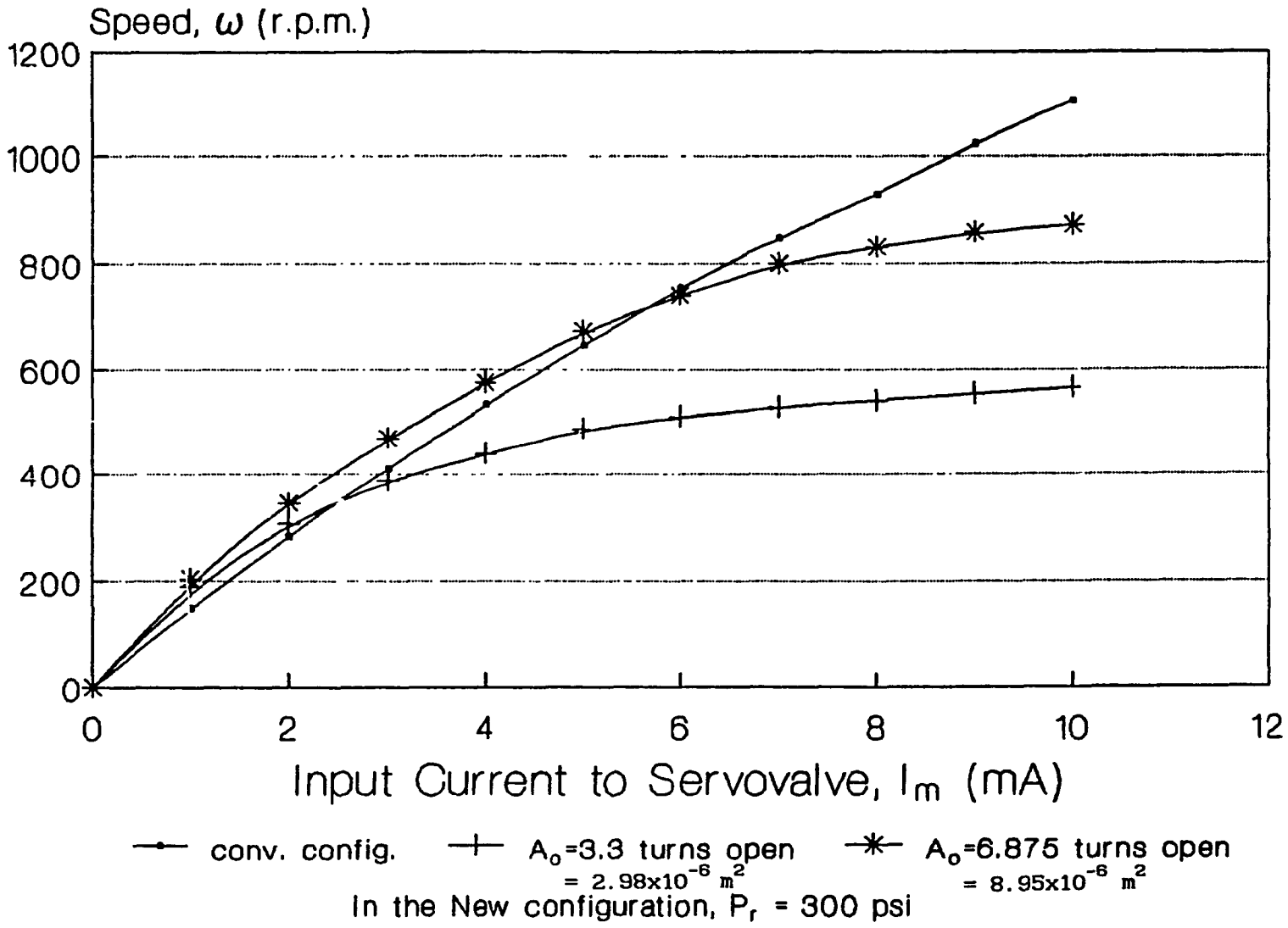

Fig. 3.12 Steady State Speed-Input Current Characteristics with Loading Pump Removed (P_r = 300 psi)

3.6 Conclusion

The experimental setup is satisfactory in that it has low leakage across or out of the motor and pump. The dynamic friction is small. The torque-speed characteristics make it possible to read the values of torque and speed outputs at a definite tuning condition by knowing the current inputs to the servovalves of the motor and pump. A comparison of the conventional and new configurations at different tuning conditions for different current inputs are given. The loading pump was removed and have the torque-input current characteristics investigation. It complies very good with previous research.

CHAPTER 4

EXPERIMENTAL OPEN LOOP STEP RESPONSES OF THE SYSTEM WITH THE LOADING PUMP REMOVED

4.1 Introduction

The new configuration was introduced because of the discovery of the existence of the advantageous properties over the conventional configuration under some tuning conditions. They were proved experimentally from the step responses of the previous setup. The properties include the lower overshoot, higher steady state gain and lower settling time in the new configuration if it were properly tuned. In this chapter, the open loop step responses of the configurations of the new setup with the loading pump removed from the shaft are carried out under the same input conditions. The purpose is to show that the advantageous properties also occur in the new setup at some selected inputs and suitable tuning conditions.

4.2 Square Wave Input

Responses of square waves signal of 1 Hz and of different open loop current amplitudes of 1 and 2 mA for the conventional configuration with the loading pump removed are shown in Fig. 4.1. It can be seen there are only one single peak of oscillation observed from the response. With large input current, there is higher damping and higher gain. When the output speed is high, the output has prominent ripples, the

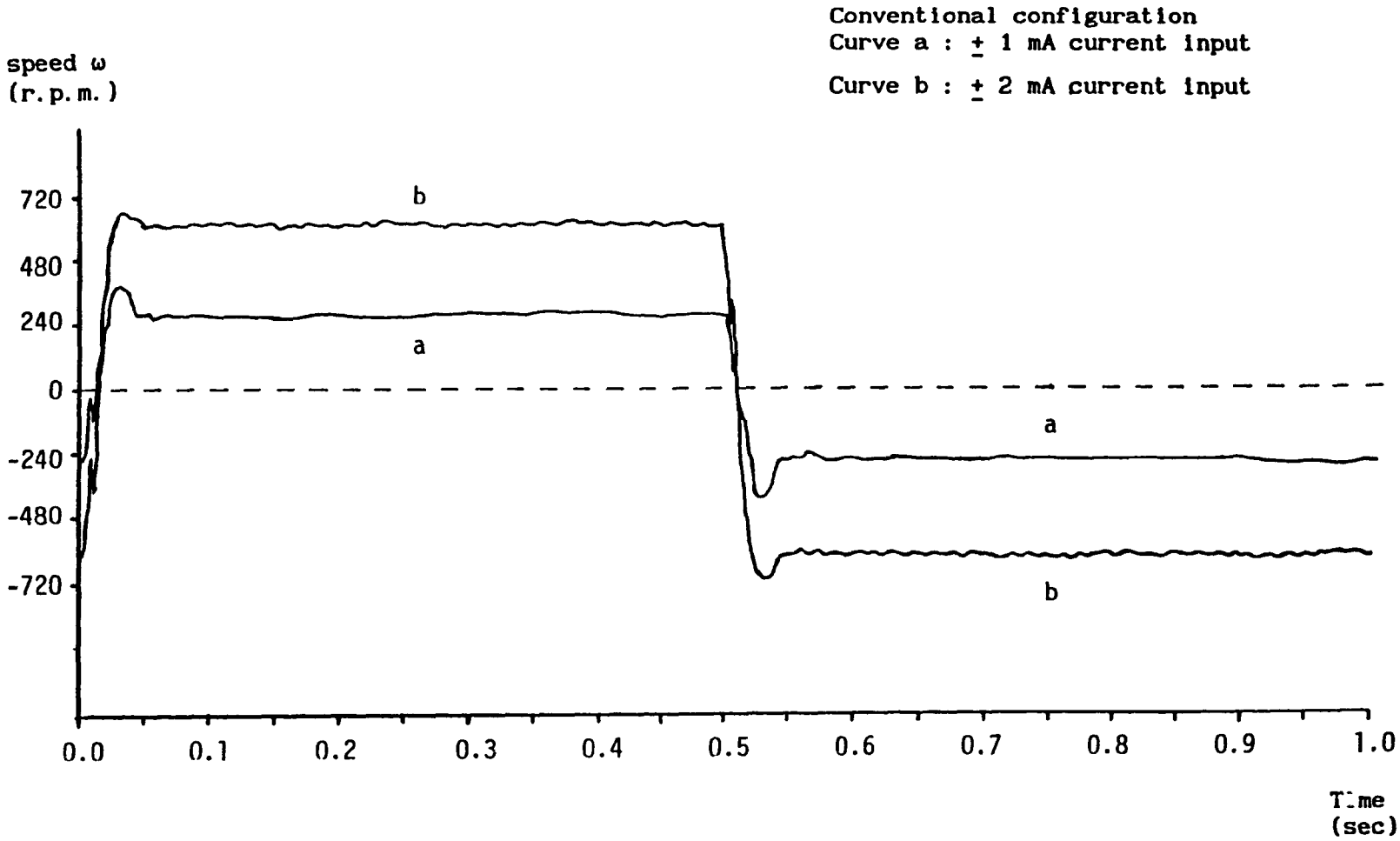

Fig. 4.1 Comparison of Square Wave Output Responses at different Input Current Levels for the Conventional Configuration

frequency of which equals to seven times of the angular velocity of the rotating shaft. The tachometer has been removed from the servomotor and tested by driving it directly with a NC machine. The output signal shows the same ripples. They should have been the noise signal of the tachometer.

Fig. 4.2 shows the effect of the metering orifice on the responses of the new configuration. With the same back pressure of 100 psi, the orifice area changes from 1 turn open (1.21×10^{-6} m^2) to 2 turns open (2.13×10^{-6} m^2). The steady state gain and the overshoot are found to be higher with the large orifice area.

Fig. 4.3 shows the effect of the back pressure on the responses of the new configuration. With a higher back pressure of 200 psi, the steady state and overshoot of the response are found to be smaller than that of with a lower back pressure of 100 psi.

Comparison of the conventional and new configurations is shown in Fig. 4.4. It is found that at the same input current, with the tuning condition of 1 turn open of orifice valve and 100 psi in back pressure, the output response of the new configuration has a lower overshoot and higher gain. With much higher amplitude of input current, it can be predicted from the steady state characteristics in Chapter 3 that the gain of the new configuration becomes lower than that of the conventional configuration. If the orifice area is increased to obtain a higher gain, a larger overshoot than the conventional configuration is expected.

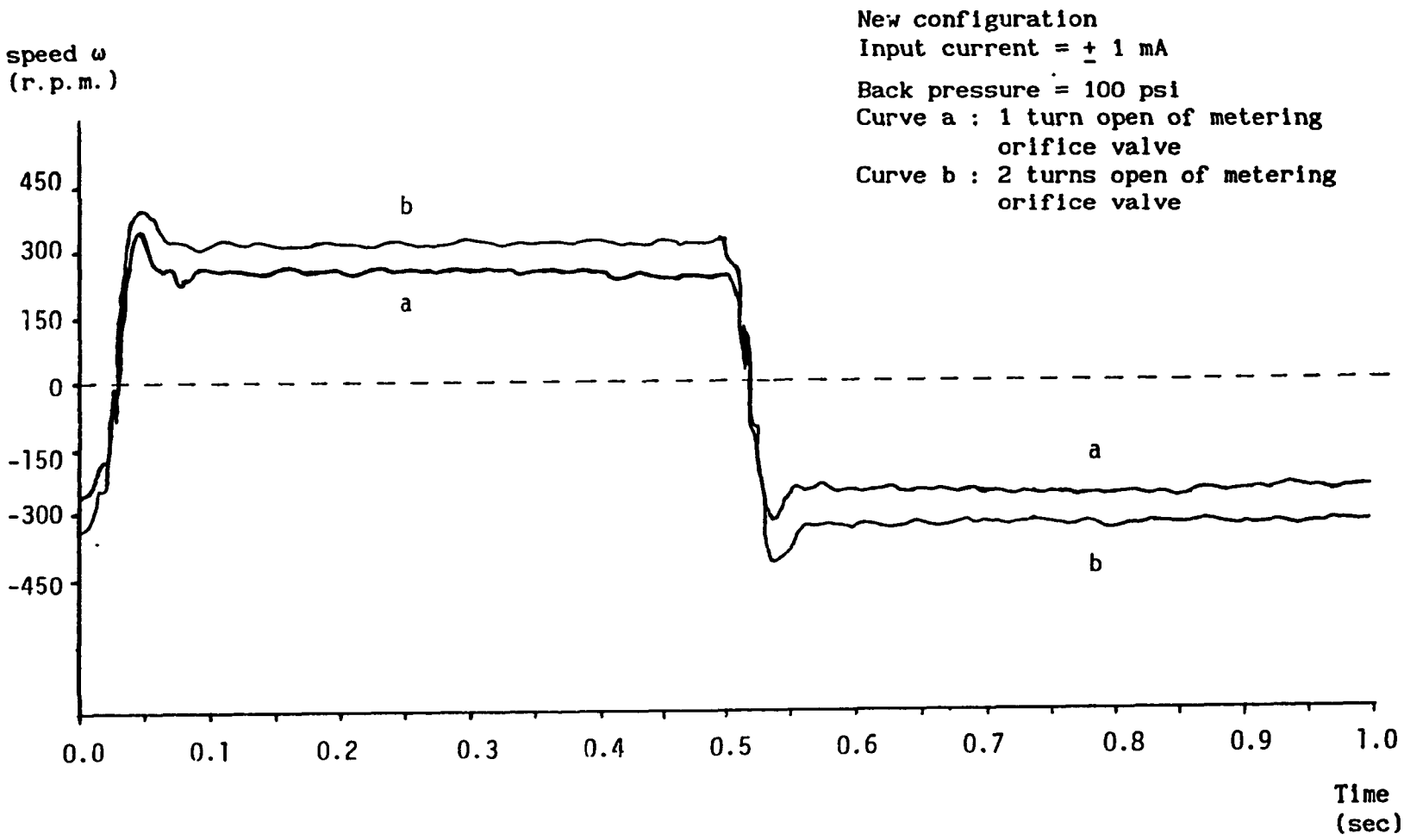

Fig. 4.2 Comparison of Square Wave Output Responses at different Metering Orifice Areas in the New Config. (P_r = 100 psi)

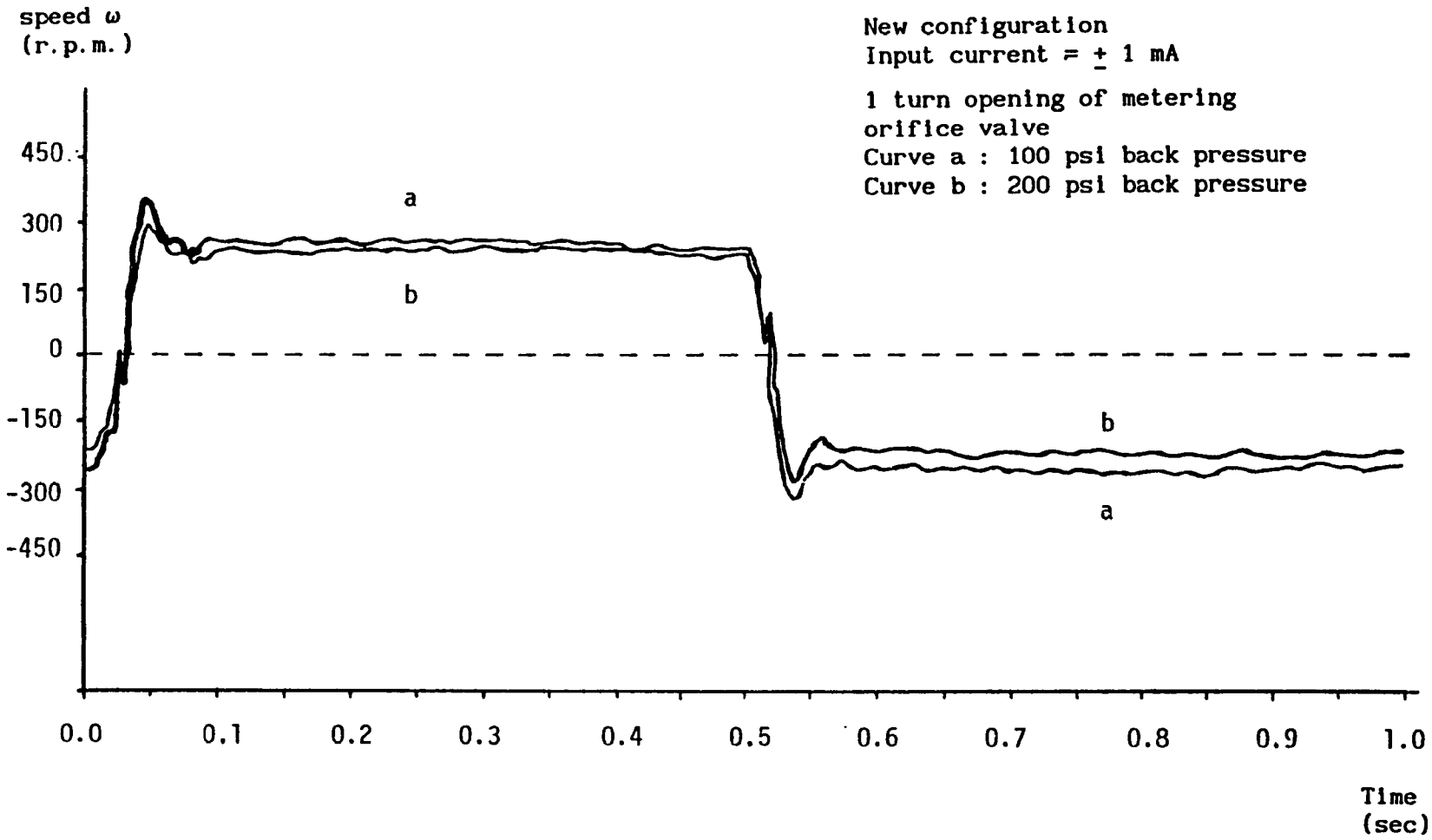

Fig. 4.3 Comparison of Square Wave Output Responses at different Back Pressures in the New Config. (A_o = 1 turn open)

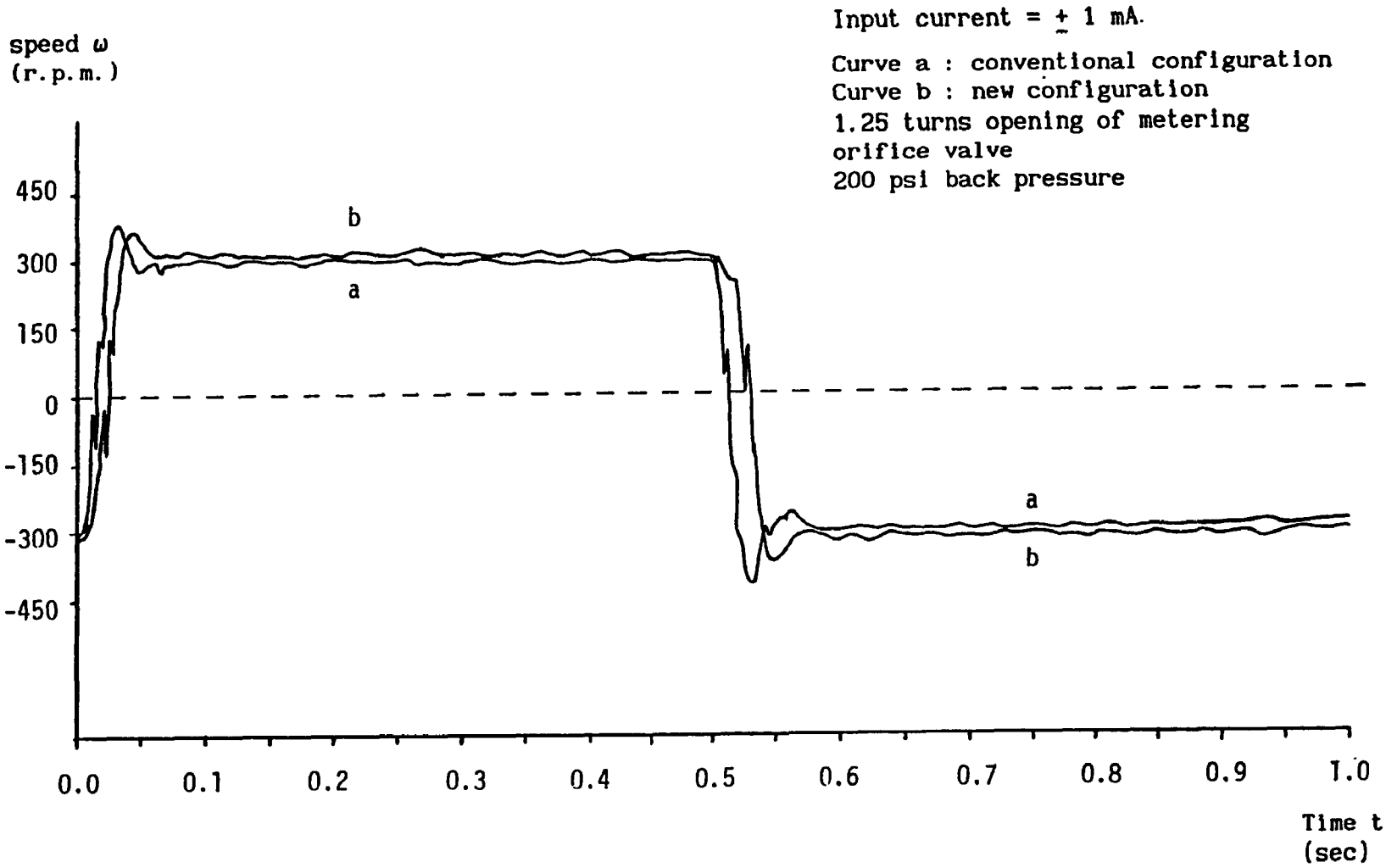

Fig. 4.4 Comparison of Square Wave Output Responses of the Two Configurations

From Fig. 4.4, it can also be seen that after the switch of the direction of rotation, the new configuration starts to rise later than the conventional configuration. It is either caused by a smaller damped natural frequency of the new configuration or by the time delay of the directional control valve, which accounts to about 8 ms. The delay can affect the stability and dynamics of the outputs. In order to eliminate its effect, an offset current can be superimposed onto the square wave input to avoid the switching of the direction of rotation.

4.3 Two Step Input

A two step input can be considered as an offset square wave. The new setup has the advantage over the old one that it has an infinite angular displacement. A wave generator can be used to generate square wave signal, which is to be superimposed through the servocontroller onto an offset input voltage signal. The total signal is then amplified to provide the current to drive the servovalve. In the following experiments, an offset current of 1.25 mA is superimposed with a square wave of amplitude 0.5 mA and 1 Hz frequency.

Fig. 4.5 shows the effect of the metering orifice on the new servovalve configuration. With a back pressure of 100 psi, the metering orifice from is opened from 2 turns (2.13×10^{-6} m^2) in curve a to 4 turns (3.70×10^{-6} m^2) in curve b. In the first half of the cycle, the curve b shows a higher gain and slightly underdamped response while curve a is overdamped. As shown in Section 4.2, the higher velocity output in the first half of the cycle gives a smaller overshoot. In the second half

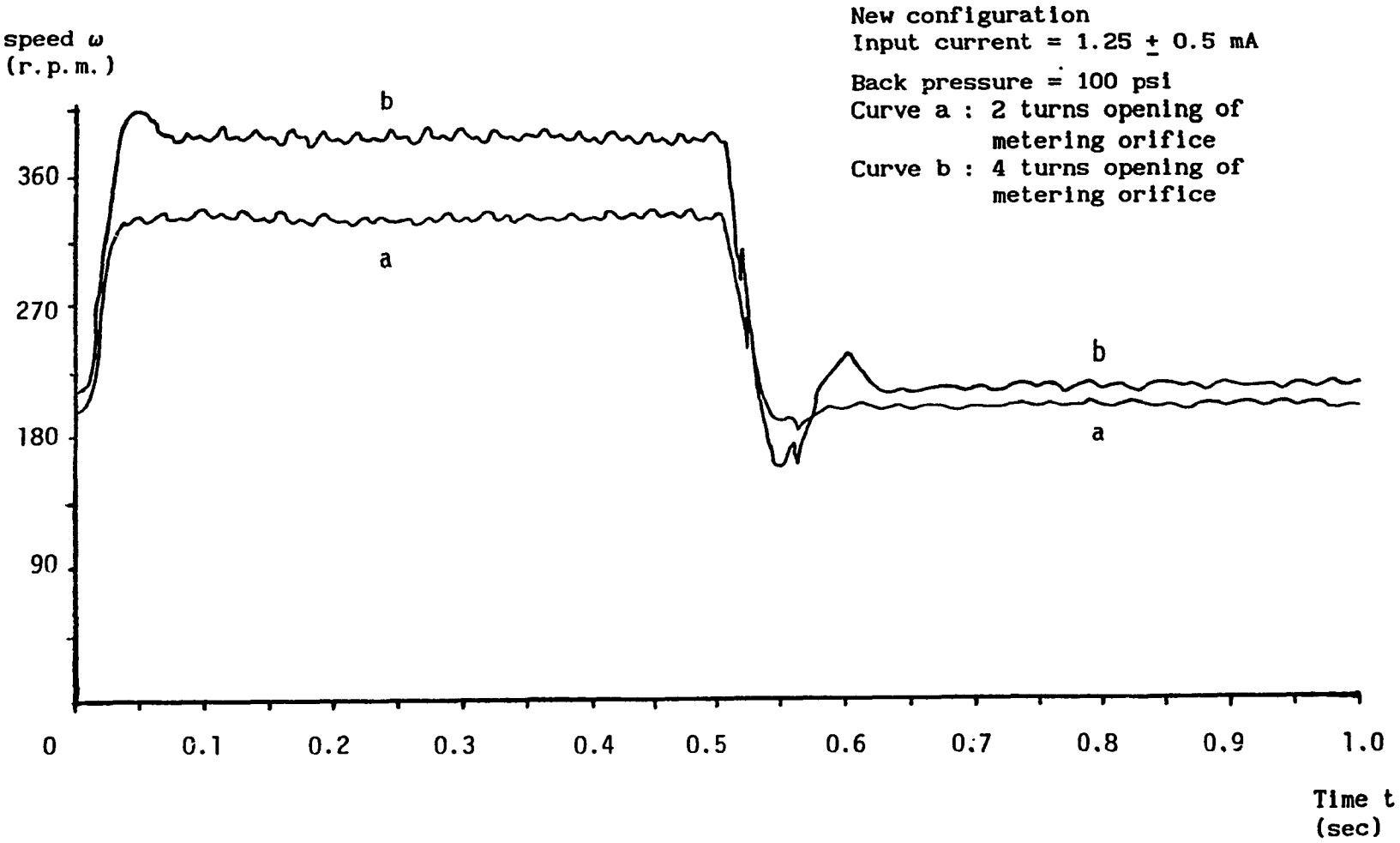

Fig. 4.5 Comparison of Two Step Output Responses at different Metering Orifice Areas in the New Config. (P_r = 100 psi)

of the cycle, the curve b still shows a higher steady state velocity but the overshoot is much larger.

Fig. 4.6 shows the effect of the back pressure on the new servovalve configuration. With a metering orifice opening of 4 turns, the back pressure changes from 100 psi to 200 psi. The steady state gain is found to drop and there is smaller overshoot or higher damping.

A comparison of output responses of the configurations is shown in Fig. 4.7. The new configuration has the tuning condition of 2 turns opening oand a back pressure of 100 psi. The advantageous output properties of lower overshoot and higher gain in the new configuration are observed. The effect of the time delay for the directional control valve has been removed. Hence, the longer time needed to reach the peak of the overshoot is caused by a smaller damped natural frequency.

4.4 Conclusion

The new setup has been shown to possess the advantageous properties found in the old setup when its new configuration is properly tuned. Being the same as the previous research, larger orifice area or lower pressure gives higher gain and higher overshoot. However, the output response has only one or two oscillations, which makes observation difficult. The presence of noises and ripples also affect the output reading. The settling time cannot be read from the responses. The damped natural frequency is found to be smaller in the new configuration. To investigate the natural frequency and damping ratio

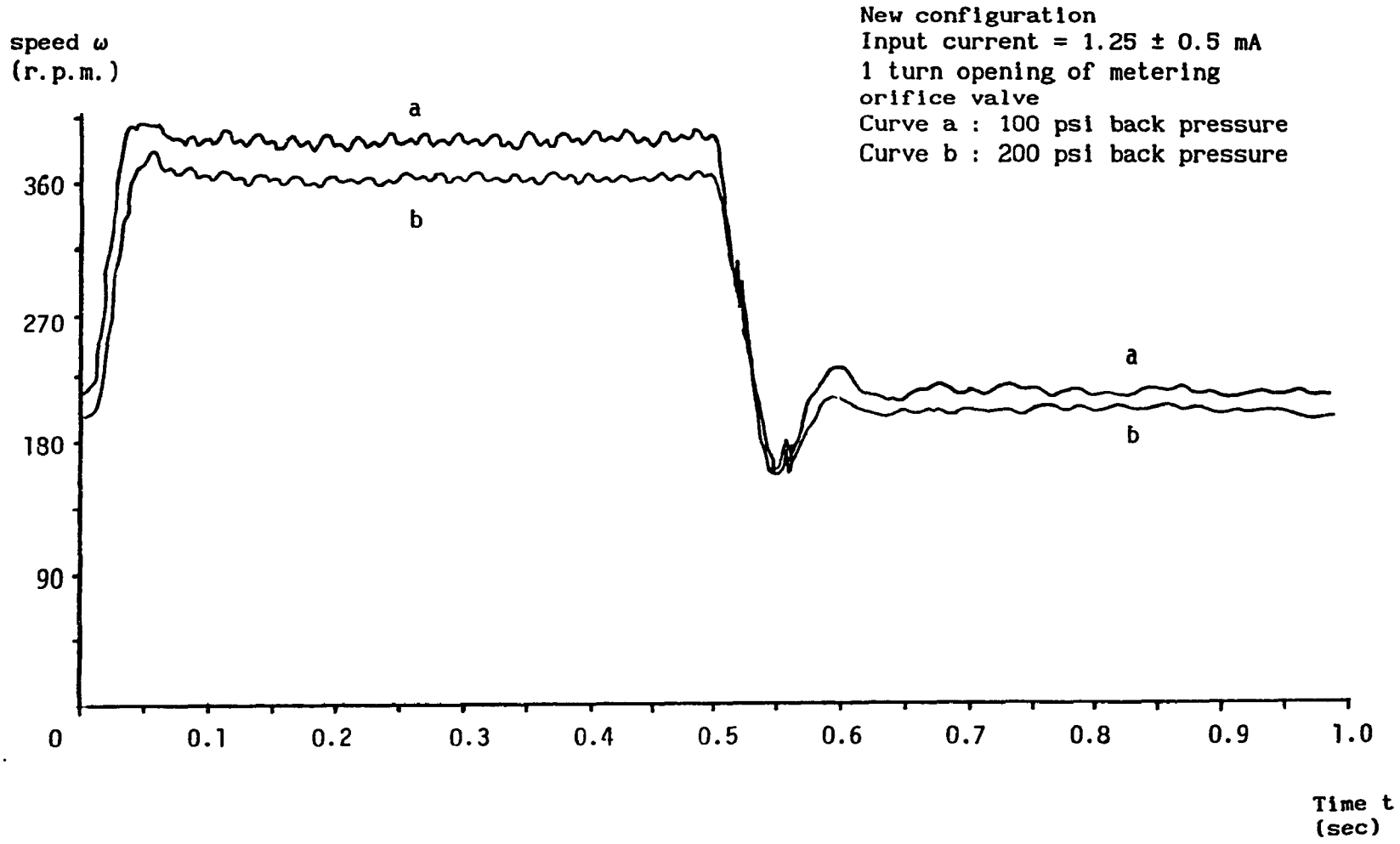

Fig. 4.6 Comparison of Two Step Output Responses at different Back Pressures in the New Config. (A_0 = 4 turns open)

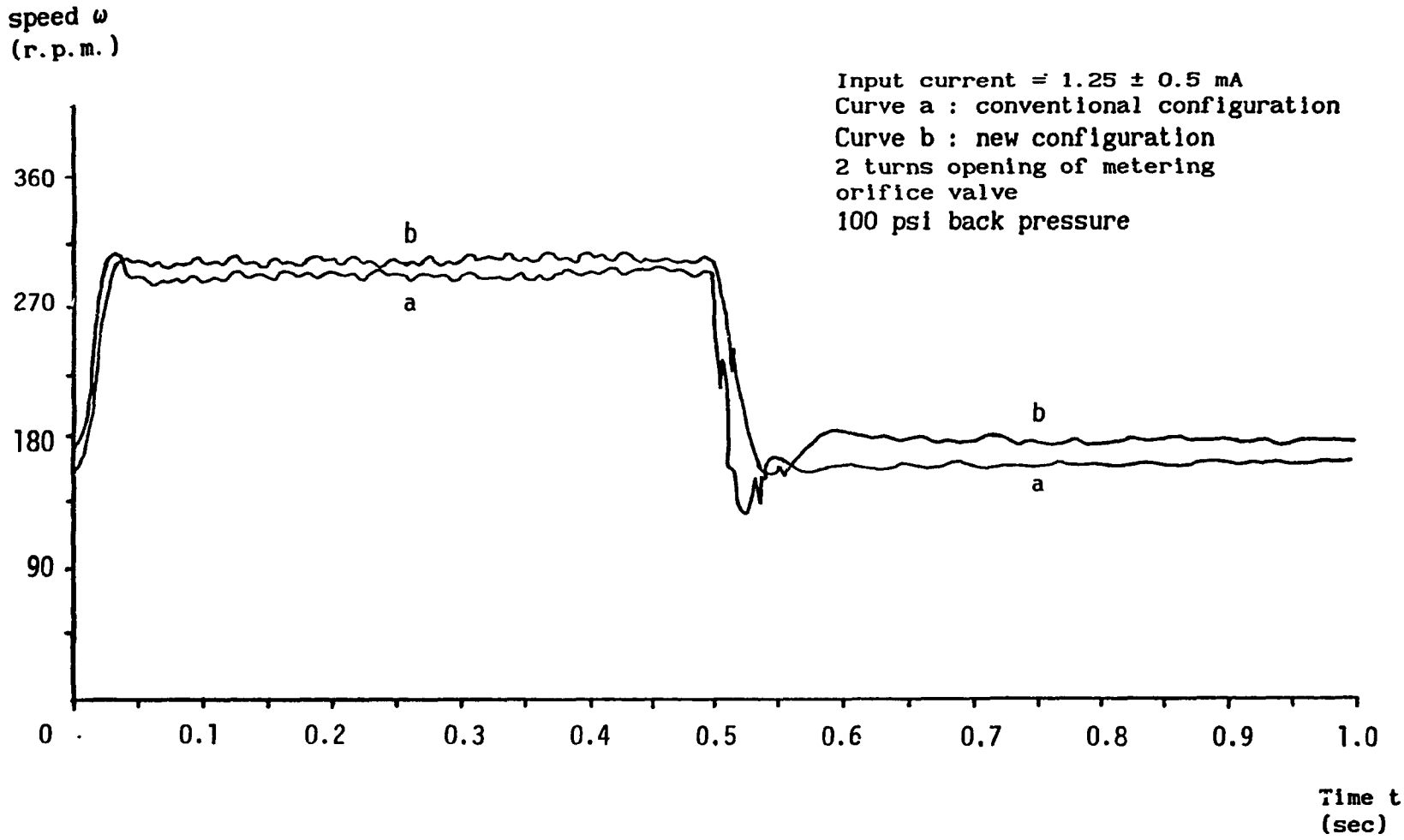

Fig. 4.7 Comparison of Two Step Output Responses of the Two Configurations

of the responses, a frequency response test is carried out in the later part of the thesis.

CHAPTER 5

NON-DIMENSIONAL FORMULATION AND SIMULATION OF THE OPEN LOOP FREQUENCY RESPONSE OF THE SERVOCIRCUITS

5.1 Introduction

In A. Limaye's thesis [13], the new configuration servosystem was found to show the advantageous characteristics of higher steady state velocity, lower settling time and lower percent overshoot than the conventional configuration if the orifice area and back pressure were properly tuned. Upon closer inspection, the new configuration can be found to have a smaller damped natural frequency than the conventional configuration.

Frequency response analysis is used in this chapter trying to give an explanation to the advantageous characteristics observed in the transient responses of the new configuration. From the plotted Bode diagram, one can determine the steady state magnitude of the response at the very low frequency region. The damping ratio and natural frequency with different inputs can be also be read off from the diagram. The variation of magnitude ratio and phase angle against input frequencies can be used to estimate the transfer function of the servosystem. Normally, small perturbation method is used to derive the transfer function under the limitation that the amplitude of input sine wave is very small and there is zero offset. However, during the experimentation, the noises in the output signal, the dead zone near the

null point, time delays in the switching elements and the static friction acting on the spool of the servovalve were found to make the output response at the null point inaccurate and very difficult to be measured. With the help of digital simulation, the Bode diagrams can be plotted to see the effects of different offsets and amplitudes of the inputs sine waves, thus giving a complete picture of the responses than that given by the small perturbation method.

5.2 Dimensionless Expression of the Characteristic Equation

The use of dimensionless quantities can reduce the number of parameters and greatly simplify the mathematical description of various effects in the servomechanisms and their subsequent analysis. Two servomechanisms are said to be running at equivalent situations if all of their dimensionless parameters are equal. The use of dimensionless quantities does not, of itself, produce new results. In principle, in the derivation and analysis of any relationship the use of dimensional or dimensionless form should give the same results.

In the dimensionless analysis of the servomechanism, it is a characteristic feature of the dimensionless quantities of voltage, input current, servovalve area, flow rates, pressures, speed, torque and back pressure that their maximum values cannot exceed unity. This feature, which is inherent in dimensionless quantities, is vital in analyzing various characteristics.

In the case of the dimensionless restrictor area, x_o , we may have

$x_o > 1$. This is because the value of x_o is an independent variable, which is, in general case, unrestricted.

For the input frequency, ω_r, a reference frequency has to be found to convert the former to a dimensionless quantity. The natural hydraulic frequency, ω_h, derived by small perturbation method from the conventional configuration is taken as a reference for both configurations to nondimensionalise ω_r into the dimensionless input frequency ω^*. The dimensional physical parameters can be grouped together to form various dimensionless quantities.

5.3 Model of the Dimensionless Analysis of the Frequency Response of the Conventional Configuration

The model is given in the form of a set of simultaneous linear and nonlinear differential dimensionless equations describing the relationship between the dimensionless quantities and the input.

a) The input signal

The sinusoidal signal is given as

$$V_i = V_{ioff} + V_{iamp} \sin\omega_r t \qquad (5.1)$$

where V_{iamp} = amplitude of input voltage command, V

V_{ioff} = offset of input voltage command, V

It can then be nondimensionalised as follow :

$$v_i = \frac{V_{ioff} + V_{iamp} \sin\omega_r t}{V_{imax}} = v_{ioff} + v_{iamp} \sin \tau \qquad (5.2)$$

where $v_{iamp} = \frac{V_{iamp}}{V_{imax}}$ = dimensionless offset of input command

$v_{ioff} = \frac{V_{ioff}}{V_{imax}}$ = dimensionless amplitude of input command

b) Input Current Signal

The current to the servovalve in a closed loop system :

$$I = K_a (V_i - K_f \omega) \qquad (5.3)$$

Rearrange (5.3),

$$V_i = \frac{I}{K_a} + K_f \omega \qquad (5.4)$$

Hence the maximum voltage input is

$$V_{imax} = \frac{I_{max}}{K_a} + K_f \omega_{max} \qquad (5.5)$$

Divide (5.4) by (5.5),

$$v_i = \frac{V_i}{V_{imax}} = \frac{\frac{I}{K_a} + K_f\omega}{\frac{I_{max}}{K_a} + K_f\omega_{max}}$$

$$= \frac{1}{1 + \frac{K_f\omega_{max}}{I_{max}/K_a}} \frac{I}{I_{max}} + \frac{1}{1 + \frac{I_{max}/K_a}{K_f\omega_{max}}} \frac{\omega}{\omega_{max}}$$

or $$v_i = \frac{1}{1 + \frac{1}{\varepsilon}} i + \frac{1}{1 + \varepsilon} \phi \qquad (5.6)$$

where $v_i = \frac{V_i}{V_{imax}}$ = dimensionless input voltage

$i = \frac{I}{I_{max}}$ = dimensionless input current

$\phi = \frac{\omega}{\omega_{max}}$ = dimensionless speed

I_{max} = maximum current to torque motor, mA

$\omega_{max} = \frac{Q_s}{D_m}$ = maximum speed, rad/s

$$\varepsilon = \frac{\text{maximum error voltage}}{\text{maximum feedback voltage}} = \frac{I_{max}/K_a}{K_f\omega_{max}}$$

For open loop frequency response analysis,

$K_f = 0$,

$\varepsilon \rightarrow \infty$,

then $v_i = i$. (5.7)

c) Servovalve Orifice Area

Assume that the transfer function for the servovalve is first order, then

$$\tau_v \frac{dA_v}{dt} + A_v = K_x K_v I \tag{5.8}$$

At steady state and maximum input current,

$$A_{vmax} = K_x K_v I_{max} \tag{5.9}$$

Divide eq. (5.8) by (5.9) and rearrange,

$$\frac{\omega_r}{\omega_h} \frac{\omega_h}{\omega_r} \frac{\tau_v \frac{dA_v}{dt}}{A_{vmax}} + \frac{A_v}{A_{vmax}} = \frac{K_x K_v I}{K_x K_v I_{max}}$$

$$\frac{\omega_r}{\omega_h} \omega_h \tau_v \frac{d\left(\frac{A_v}{A_{vmax}}\right)}{d(\omega_r t)} + \frac{A_v}{A_{vmax}} = \frac{I}{I_{max}}$$

$$\omega^* \tau_v^* \frac{dx_v}{d\tau} + x_v = i \tag{5.10}$$

where ω_r = sinusoidal frequency of input signal, rad/s

$$\tau_v^* = \omega_h \tau_v = \text{dimensionless time constant of servovalve}$$

$$\omega_h = \sqrt{\frac{2\beta D_m^2}{JV}} = \text{natural hydraulic frequency of the conventional configuration, rad/s}$$

$$\omega^* = \frac{\omega_r}{\omega_h} = \text{dimensionless input frequency}$$

$$x_v = \frac{A_v}{A_{vmax}} = \text{dimensionless servovalve area}$$

$$\tau = \omega_r t = \text{dimensionless time unit}$$

d) The Flows through the Servovalve Area

It is assumed that the servovalve orifices are matched and symmetrical and there is no internal leakage insides the servovalve.

The flowrates are given by the equations (for $x_v > 0$)

$$Q_1 = C_d A_v \sqrt{\frac{2(P_s - P_1)}{\rho}} \qquad (5.11)$$

$$Q_2 = C_d A_v \sqrt{\frac{2P_2}{\rho}} \qquad (5.12)$$

Divide the equations by the maximum flowrates

$$q_1 = \frac{\sqrt{\frac{2(P_s - P_1)}{\rho}}}{Q_s} = \frac{C_d A_v \sqrt{\frac{2P_s}{\rho}} \sqrt{\frac{P_s - P_1}{P_s}}}{C_d A_{vmax} \sqrt{\frac{P_s}{\rho}}} = \sqrt{2}\, x_v \sqrt{1 - p_1} \qquad (5.13)$$

Similarly,

$$q_2 = \sqrt{2}\, x_v \sqrt{p_2} \tag{5.14}$$

e) Chambers Flow Pressure Relationship

The equations of changes of pressures in the actuator chambers in taking into acount of the compressibility of oil and internal and external leakages can be non-dimensionalised as follows :

In the first chamber,

$$\frac{V}{\beta}\frac{dP_1}{dt} = Q_1 - D_m\omega - C_{im}(P_1 - P_2) - C_{em}P_1 \tag{5.15}$$

Divide eq. (5.15) by Q_s and rearrange :

$$\frac{P_s\omega_r}{P_s\omega_r}\frac{\frac{V}{\beta}\frac{dP_1}{dt}}{Q_s} = \frac{Q_1}{Q_s} - \omega_{max}\frac{D_m\omega}{Q_s\omega_{max}} - \frac{P_s C_{im}}{Q_s}\frac{(P_1-P_2)}{P_s} - \frac{P_s C_{em}}{Q_s}\frac{P_1}{P_s}$$

$$\frac{VP_s\omega_r}{\beta Q_s}\frac{d(\frac{P_1}{P_s})}{d(\omega_r t)} = \frac{Q_1}{Q_s} - \frac{D_m\omega_{max}}{Q_s}\frac{\omega}{\omega_{max}} - \frac{P_s C_{im}}{Q_s}\frac{(P_1-P_2)}{P_s} - \frac{P_s C_{em}}{Q_s}\frac{P_1}{P_s}$$

or

$$\frac{2\omega^*}{\alpha}\frac{dp_1}{d\tau} = q_1 - \phi - \frac{C_{im}}{\alpha}(p_1 - p_2) - \frac{C_{em}}{\alpha}p_1 \tag{5.16}$$

where $Q_s = C_d A_{vmax}\sqrt{\frac{P_s}{\rho}}$ = maximum flowrate at maximum servovalve area and zero load pressure, m/s

$$p_{1,2} = \frac{P_{1,2}}{P_s} = \text{dimensionless servomotor chamber pressure}$$

$$q_{1,2} = \frac{Q_{1,2}}{Q_s} = \text{dimensionless flowrates}$$

$$\frac{VP_s\omega_r}{\beta Q_s} = \frac{\frac{\omega_r}{\omega_h}}{\frac{Q_s\beta\omega_h}{VP_s\omega_h^2}} = \frac{2\omega^*}{\frac{J\omega_h Q_s}{P_s D_m^2}} = \frac{2\omega^*}{\alpha}$$

with

$$\alpha = \frac{J\omega_h Q_s}{P_s D_m^2} = \frac{J\omega_h \omega_{max}}{P_s D_m}$$

$$= \frac{\text{maximum inertial torque at natural frequency}}{\text{inertia load torque}}$$

$$= \text{dimensionless inertia load factor}$$

and

$$\omega_{max} = \frac{Q_s}{D_m} = \text{maximum speed of the motor}$$

also

$$c_{im} = \frac{JC_{im}\omega_h}{D_m^2} = \text{internal leakage load factor}$$

also

$$c_{em} = \frac{JC_{em}\omega_h}{D_m^2} = \text{external leakage load factor}$$

because $\frac{C_{im}P_s}{Q_s} = \frac{c_{im}}{\alpha}$ and $\frac{C_{em}P_s}{Q_s} = \frac{c_{em}}{\alpha}$

In the second chamber, the flow pressure relationship,

$$\frac{V}{\beta}\frac{dP_2}{dt} = -Q_2 + D_m\omega + C_{im}(P_1 - P_2) - C_{em}P_2 \qquad (5.17)$$

can be non-dimensionalised similarly to

$$\frac{2\omega^*}{\alpha}\frac{dp_2}{d\tau} = -q_2 + \phi + \frac{c_{im}}{\alpha}(p_1 - p_2) - \frac{c_{em}}{\alpha}p_2 \qquad (5.18)$$

$\frac{(5.16) - (5.18)}{2}$:

$$\frac{\omega^*}{\alpha}\frac{dp_\ell}{d\tau} = q_\ell - \phi - \frac{c_\ell}{\alpha}p_\ell \qquad (5.19)$$

where

$$c_\ell = c_{im} + \frac{c_{em}}{2} = \text{dimensionless leakage load factor}$$

f) Torque - Acceleration Equation of the Rotating Shaft

The torque - acceleration equation of the actuator, assuming inertia load, viscous damping and external load torque but neglecting the frictional torque is :

$$J\frac{d\omega}{dt} = D_m(P_1 - P_2) - B\omega - T_\ell \qquad (5.20)$$

Divide the equation by $D_m P_s$ and rearrange :

$$\frac{\omega_r}{\omega_r}\frac{\omega_{max}}{\omega_{max}}\frac{\omega_h}{\omega_h}\frac{J\frac{d\omega}{dt}}{D_m P_s} = \frac{D_m(P_1 - P_2)}{D_m P_s} - \frac{B\omega}{D_m P_s}\frac{\omega_{max}}{\omega_{max}} - \frac{T_\ell}{D_m P_s}$$

$$\frac{J\omega_{max}\omega_h}{D_m P_s}\frac{\omega_r}{\omega_h}\frac{d(\frac{\omega}{\omega_{max}})}{d(\omega_r t)} = \frac{P_1 - P_2}{P_s} - \frac{B\omega_{max}}{D_m P_s}\frac{\omega}{\omega_{max}} - \frac{T_\ell}{D_m P_s}$$

or

$$\alpha\omega^*\frac{d\phi}{d\tau} = p_1 - p_2 - \gamma\phi - t_\ell \qquad (5.21)$$

where

$$\gamma = \frac{B\omega_{max}}{D_m P_s} = \frac{\text{maximum viscous torque}}{\text{stall torque}}$$

= viscous load factor

$$t_\ell = \frac{T_\ell}{D_m P_s} = \frac{\text{external torque}}{\text{stall torque}}$$
$$= \text{torque load factor}$$

g) Open Loop Characteristic Equations of the Conventional Configuration

If the internal leakage inside the servovalve can be neglected, then $q_1 = q_2$ at the steady state, because the servovalve is matched and symmetric.

Moreover, if the external leakage of the servomotor can also be neglected, then $q_1 = q_2$ even in the transient state. Such case is usually considered true as the external leakage is practically very small.

Equate equations (5.13) and (5.14) :

$$1 = p_1 + p_2 \tag{5.22}$$

Differentiate (5.22) w.r.t. τ,

$$\frac{dp_1}{d\tau} = - \frac{dp_2}{d\tau} \tag{5.23}$$

Such condition is also satisfied if $q_1 = q_2$ is substituted into the equations (5.16) and (5.18). It means that the pressure gradients in the two chambers are equal and opposite at any time.

With the load pressure defined as

$$p_\ell = p_1 - p_2 \tag{5.24}$$

p_1 and p_2 be solved from eq. (5.22) and (5.24) :

$$p_1 = \frac{1 + p_\ell}{2}$$

and

$$p_2 = \frac{1 - p_\ell}{2}$$

Substituting p_1 and $p_2$into equations (5.13) and (5.14) to obtain :

$$q_1 = q_2 = x_v\sqrt{1 - p_\ell}$$

The load flow is given by :

$$q_\ell = \frac{q_1 + q_2}{2} = x_v\sqrt{1 - p_\ell} \tag{5.25}$$

For the case of $x_v < 0$, the flow rates are given by :

$$q_1 = x_v\sqrt{p_1}$$
$$q_2 = x_v\sqrt{1 - p_2}$$

Hence the load flow becomes

$$q_\ell = x_v\sqrt{1 + p_\ell} \tag{5.26}$$

Combining equations (5.25) and (5.26) for all values of x_v,

$$q_\ell = x_v\sqrt{1 - p_\ell \frac{x_v}{|x_v|}} \tag{5.27}$$

A single non-linear differential characteristic equation can be obtained by eliminating q_ℓ and p_ℓ amongst the equations (5.19), (5.21) and (5.27), giving a single equation :

$$x_v\sqrt{1 - (\alpha\omega^* \frac{d\phi}{d\tau} + \gamma\phi + t_\ell)\frac{x_v}{|x_v|}}$$
$$= (\omega^*)^2 \frac{d^2\phi}{d\tau^2} + (c_\ell + \frac{\gamma}{\alpha})\omega^* \frac{d\phi}{d\tau} + (1 + \frac{c_\ell}{\alpha}\gamma)\phi + \frac{c_\ell}{\alpha}t_\ell \tag{5.28}$$

This equation shows the nonlinear relationship of output ϕ with the input servovalve area x_v. Now the equations (5.2), (5.7), (5.10) and (5.28) can give a complete dimensionless model of the open loop conventional configuration for frequency response analysis. If the external leakage is taken into account, the set of equations to be solved are (5.2), (5.7), (5.10), (5.13), (5.14), (5.16), (5.18) and (5.21).

5.4 Model of the Dimensionless Analysis of the Frequency Response of the New Configuration

Assume that the lengths of the tubings between the servovalve and servoactuator are adjusted such that the volumes of hydraulic oil are equivalent in both chambers of the actuators and in both configurations. The dynamics of the directional control and relief valves are also neglected.

- For $x_v > 0$, the dimensionless flow rates in and out of the actuators are now :

$$q_1 = \sqrt{2}\, x_v \sqrt{1 - p_1} \tag{5.29}$$

$$q_2 = \sqrt{2}\, x_o \sqrt{p_2 - p_r} \tag{5.30}$$

where $x_o = \frac{A_o}{A_v}$ = dimensionless orifice area

$p_r = \frac{P_r}{P_s}$ = dimensionless back pressure

Assume that q_1 and q_2 are equal, then squaring and equating eq. (5.29) and (5.30) to obtain :

$$x_o^2(p_2 - p_r) = x_v^2(1 - p_1)$$

Differentiate both sides w.r.t. τ :

$$x_o^2 \frac{dp_2}{d\tau} = 2x_v(1 - p_1) \frac{dx_v}{d\tau} - x_v^2 \frac{dp_1}{d\tau} \tag{5.31}$$

However, from equations (5.16) and (5.18), if $q_1 = q_2$ and neglecting the external leakage, then

$$\frac{dp_1}{d\tau} = - \frac{dp_2}{d\tau} \tag{5.32}$$

The equations (5.31) and (5.32) contradict each other. Hence the assumption that $q_1 = q_2$ cannot be established or the flow rate

transients and the pressure gradients are not equal in the two chambers. This is because the introduction of the back pressure and the non-oscillating orifice area at the exit port has broken down the symmetry of the system. Therefore, the relationship between the servovalve area x_v and output speed ϕ cannot be represented by a single nonlinear expression.

The dimensionless model of the new configuration are now represented by the equations (5.2), (5.7), (5.10), (5.16), (5.18), (5.21), (5.29) and (5.30). It can be observed that in the above equation, the restrictor area x_o is fixed rather than oscillating like the servovalve area x_v. Assume that the transfer function of the servovalve does not change in switching from the conventional configuration to the new configuration. If the restrictor area x_o is set to move exactly in the same amplitude and in phase with the servovalve area x_v and the back pressure p_r is zero, then the new configuration is equivalent to the conventional configuration.

5.5 Computational Simulation Method

The frequency response curves are obtained by solving the following two sets of non-linear differential equations using the Runge-Kutta method :

a) For the conventional configuration :

- Input signal, from equations (5.2) and (5.7) :

$$v_i = i = v_{ioff} + v_{iamp} \sin\tau \tag{5.33}$$

- Servovalve opening, from equation (5.10) :

$$\frac{dx_v}{d\tau} = \frac{1}{\omega^* \tau_v^*} (i - x_v) \tag{5.34}$$

- Pressures in the chambers, from equations (5.16) and (5.18) :

$$\frac{dp_1}{d\tau} = \frac{\alpha}{2\omega^*} (\sqrt{2}\, x_v \sqrt{1 - p_1} - \phi - \frac{c_{im}}{\alpha} (p_1 - p_2) - \frac{c_{em}}{\alpha} p_1) \tag{5.35}$$

$$\frac{dp_2}{d\tau} = \frac{\alpha}{2\omega^*} (-\sqrt{2}\, x_v \sqrt{p_2} + \phi + \frac{c_{im}}{\alpha} (p_1 - p_2) - \frac{c_{em}}{\alpha} p_2) \tag{5.36}$$

- Actuator torque-acceleration, from equation (5.21) :

$$\frac{d\phi}{d\tau} = \frac{1}{\alpha\omega^*} (p_1 - p_2 - \gamma\phi - t_\ell) \tag{5.37}$$

In case of $x_v < 0$, substitute

$$q_1 = \sqrt{2}\, x_v \sqrt{p_1} \qquad \text{and}$$
$$q_2 = \sqrt{2}\, x_v \sqrt{1 - p_2}$$

into equations (5.35) and (5.36) respectively.

If the external leakage is neglected, equations (3.56) and (3.57) can be replaced by a single non-linear equation for the load pressure p_ℓ :

$$\frac{dp_\ell}{d\tau} = \frac{\alpha}{\omega^*} \left(x_v \sqrt{1 - p_{\ell} \frac{x_v}{|x_v|}} - \phi - \frac{c_\ell}{\alpha} p_\ell \right) \qquad (5.38)$$

Equation (5.37) is then changed to :

$$\frac{d\phi}{d\tau} = \frac{1}{\alpha\omega^*} \left(p_\ell - \gamma\phi - t_\ell \right) \qquad (5.39)$$

b) For the new configuration, equations (5.33), (5.34), (5.35) and (5.37) are the same except that equations (5.36) is replaced by the equation :

$$\frac{dp_2}{d\tau} = \frac{\alpha}{2\omega^*} \left(-\sqrt{2}x_o \sqrt{p_2 - p_r} + \phi + \frac{c_{im}}{\alpha} (p_1 - p_2) - \frac{c_{em}}{\alpha} p_2\right) \qquad (5.40)$$

In the case of $x_v < 0$, substitute

$$q_1 = -\sqrt{2}x_o \sqrt{p_1 - p_r} \quad \text{and}$$
$$q_2 = \sqrt{2}x_v \sqrt{1 - p_2}$$

into equations (5.35) and (5.40) respectively.

With approximate initial values of x_v, p_ℓ and ϕ, sinusoidal signals, v_i, of different offsets, v_{ioff}, amplitudes, v_{iamp}, and input frequencies, ω^*, are input to the system. Several cycles of time are allowed for the output speed waveform, ϕ, to become steady. The amplitude ratio and phase lag of the output compared to the input are then plotted by the computer to form the Bode diagram.

$$\text{Amplitude ratio} = 20 \log_{10} \frac{\text{peak to peak value of output } \phi}{2 \text{ x amplitude of input sine wave}}$$

5.6 Conversion of the Experimental Physical Parameters into Dimensionless Parameters

The experimental set up was described in Chapter 2. The following gives a summary of the dimensional and dimensionless parameters.

a) Physical Constants or Measured Parameters

Supply pressure, $P_s = 1000$ psi

$= 6.894 \times 10^{6}$ Nm^{-3}

Density of oil (Tellus 46), $\rho = 867$ kgm^{-2}

Bulk modulus of oil (Tellus 46), $\beta = 7.995 \times 10^{8}$ Nm^{-2}

Moment of inertia of rotary parts, $J = 0.00482$ kgm^{2}

Volume of one chamber, $V = 1.354 \times 10^{-4}$ m^{3}

Time constant of servovalve, $\tau_v = 3.18 \times 10^{-3}$ s $= \frac{1}{50 \text{ Hz}}$

Displacement of servomotor, $D_m = 2.802 \times 10^{-6}$ m^{3}

b) Calculated Parameters or Calibrated Values

Dynamic frictional torque, $T_\ell = 1.12$ Nm

Servomamplifier gain, $K_a = 7.78$ mA/V

Viscous damping coefficient, $B = 0.0766$ Nms

Stall torque, $P_s D_m = 6.894 \times 10^{-6} \times 2.802 \times 10^{-6}$

$= 19.317$ Nm

Maximum speed, from eq. (5.21) $\omega_{max} = \frac{P_s D_m - T_\ell}{B}$

$$= \frac{19.317 - 1.12}{0.0766}$$

$$= 237.6 \text{ rad s}^{-1}$$

$$= 2269 \text{ r.p.m.}$$

Servovalve area gain constant, $K_x K_v = 7.94 \times 10^{-7} \text{ m}^2/\text{mA}$

Maximum flowrate, $Q_s = D_m \omega_{max}$

$$= 6.7 \times 10^{-4} \text{ m}^3\text{s}^{-1}$$

$$= 10.6 \text{ GPM}$$

Maximum servovalve area, $$A_{vmax} = \frac{Q_s}{C_d \sqrt{\frac{P_s}{\rho}}}$$

$$= 1.235 \times 10^{-5} \text{ m}^2$$

Maximum input current, $$I_{max} = \frac{A_{vmax}}{K_x K_v}$$

$$= 15.56 \text{ mA}$$

Maximum input voltage, $$V_{imax} = \frac{I_{max}}{K_a}$$

$$= 2.0 \text{ V}$$

Internal leakage coefficient of servomotor, $C_{im} = 8.62 \times 10^{-13} \text{ m}^3\text{s}^{-1}/\text{Nm}^{-2}$

External leakage coefficient of servomotor, $C_{em} = 8.54 \times 10^{-14} \text{ m}^3\text{s}^{-1}/\text{Nm}^{-2}$

Total leakage coefficient of servomotor, $$C_l = C_{im} + \frac{C_{em}}{2}$$

$$= 9.047 \times 10^{-13} \text{ m}^3\text{s}^{-1}/\text{Nm}^{-2}$$

Resonant hydraulic frequency, $$\omega_h = \sqrt{\frac{2\beta D_m^2}{JV}}$$

$$= 138.7 \text{ rad s}^{-1} = 22.07 \text{ Hz}$$

c) Non-dimensional Parameters

Dimensionless time constant of servovalves,

$$\tau_v^* = \omega_h \tau_v$$
$$= 138.7 \times 3.18 \times 10^{-3}$$
$$= 0.441$$

Inertia load factor,

$$\alpha = \frac{J\omega_h \omega_{max}}{P_s D_m}$$
$$= \frac{0.004821 \times 138.7 \times 237.6}{6.894 \times 10^6 \times 2.802 \times 10^{-6}}$$
$$= 8.30$$

Viscous load factor,

$$\gamma = \frac{B\omega_{max}}{P_s D_m}$$
$$= \frac{0.0766 \times 237.6}{19.317}$$
$$= 0.942$$

Total leakage load factor,

$$c_\ell = \frac{JC_\ell \omega_h}{D_m^2}$$
$$= \frac{0.004821 \times 9.047 \times 10^{-13} \times 138.7}{(2.802 \times 10^{-6})^2}$$
$$= 0.08$$

Torque load factor,

$$t_\ell = \frac{T_s}{P_s D_m}$$
$$= \frac{1.12}{19.317}$$
$$= 0.058$$

The values of these non-dimensional parameters are used to describe the model of the conventional configuration. With the addition of the dimensionless tuning parameters x_o and p_r, the new configuration can be described.

5.7 Simulation Results and Comparisons

The systems of equations in Section 5.5 are solved by using Fortran 77 on the minicomputer Vax/780. It has first to be realised that the models are inherently nonlinear due to the presence of a square root sign in the flow equations. In the new configuration, the presence of the restrictor area, A_o, in the return line enhances the nonlinearity because it remains constant while the servovalve area is oscillating, making the servosystem unsymmetrical.

The input signal is

$$V_i = (0.3 + 0.2 \sin\omega t)\ V$$

or normalised as

$$v_i = i = 0.15 + 0.1 \sin\tau$$

The plot in Fig. 5.1 for the conventional configuration show that the increase of v_{ioff} will increase the damping, decrease the steady state gain but decrease the damped natural frequency slightly.

For the new configuration, the restrictor settings are

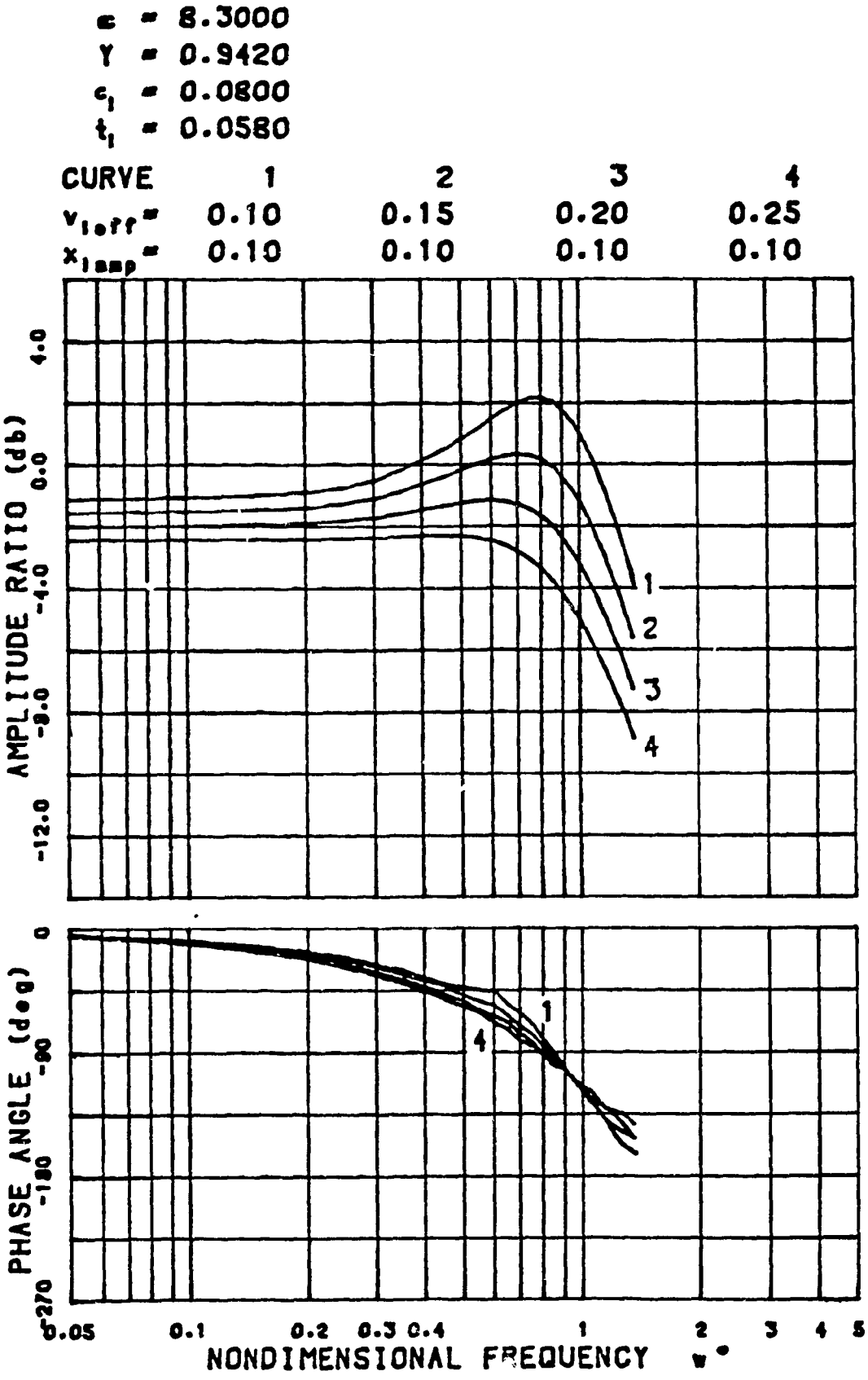

Fig. 5.1 Effect of v_{1off} on the Frequency Responses of the Conventional Configuration

Number of turns opened	$x_o = \frac{A_o}{A_{vmax}}$
2	0.166
4	0.294
5	0.397
6	0.513
8	0.920

where $A_{vmax} = 1.235 \times 10^{-5}\ m^2$,

and the pressure settings are

Back pressure, P_r (psi)	$p_r = \frac{P_r}{P_s}$
100	0.1
200	0.2
300	0.3
400	0.4

where P_s = 1000 psi.

The Bode diagram for different restrictor orifice areas x_o at 2, 4, 6 and 8 turns open and at p_r = 0.1 are given in Fig. 5.2. It can be seen that if x_o is too small (i.e. x_o = 0.166), the output has a diminished amplitude and smaller phase lag. When x_o increases, the amplitude ratio curves move upward and tend to converge. They also show a higher steady state gain in the low frequency region and lower damping. The resonant frequencies increase slightly with x_o and stay

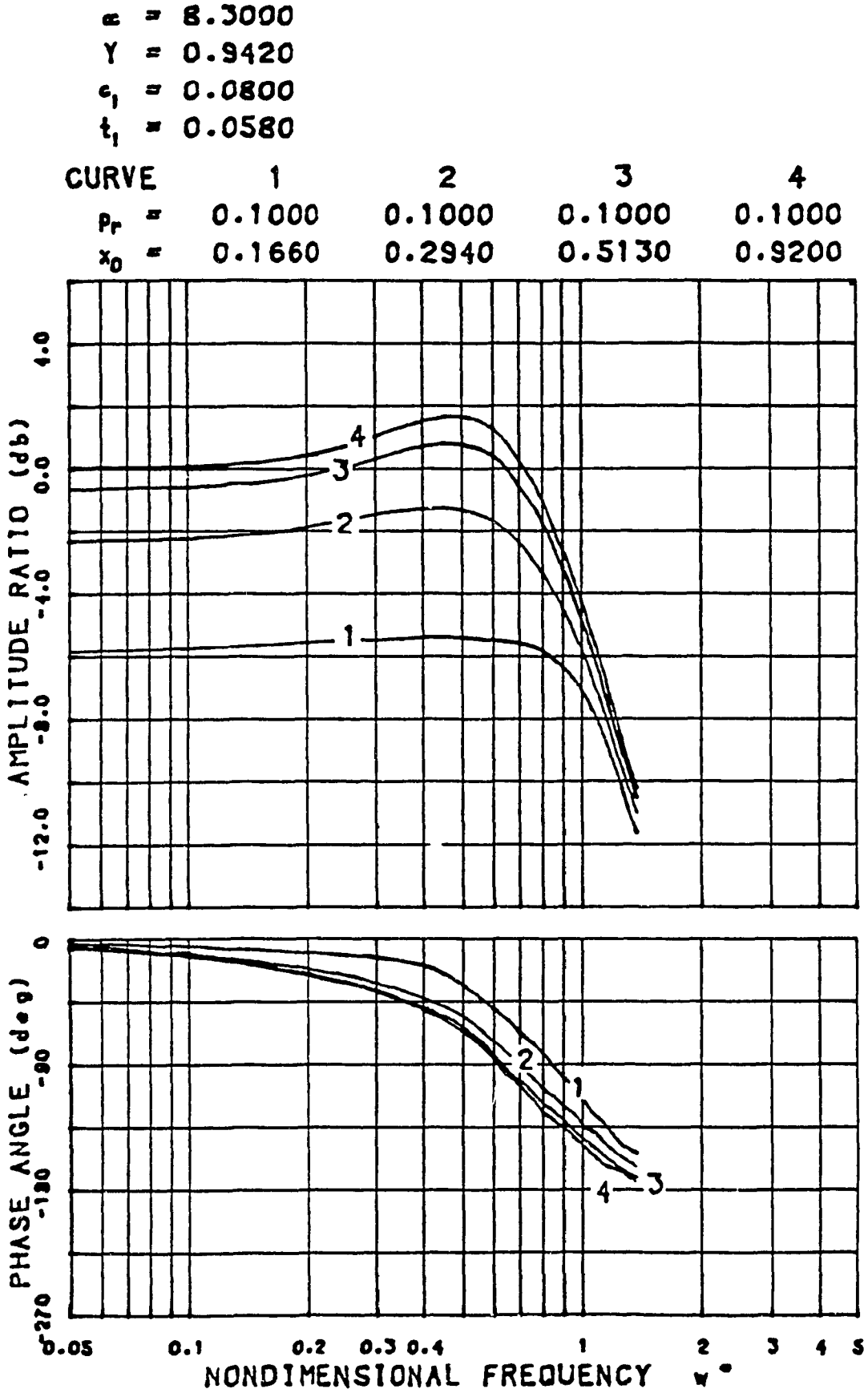

Fig. 5.2 Effect of x_0 on the New Configuration Frequency Responses (v_1 = 0.15 + 0.1 sinτ)

around $\omega^* = 0.45$ to 0.50. The phase lag is also found to increase and converge when x_o increases.

Fig. 5.3 plots the Bode diagram for different return pressure settings where it can be seen that when p_r increases from 0.1 to 0.4, the amplitude ratio curves move downward rather evenly, showing a lower steady state gain, higher damping and slightly decreasing resonant frequency, ranging from $\omega^* = 0.4$ to 0.5. The phase lag is found to decrease slightly with the increase in p_r.

In Fig. 5.4 and 5.5, the response of the conventional configuration is plotted together with those of the new configuration at different settings of x_o and p_r respectively. As illustrated in Fig. 5.4, the value of x_o in the new configuration should not be too small like the situation in the curve 2 (4 turns of opening of orifice). An excessively large x_o value can cause the amplitude ratio curve of the new configuration to exhibit an undesirably high resonance peak (i.e. curve 4 for 6 turns of opening of orifice). The curve 3 (5 turns of opening) is the desirable one. Even if the resonance peak were too high, it is possible to be brought down by increasing the value of p_r in the curve 4 of Fig. 5.4 or the equivalent curve 2 of Fig. 5.5. It results in a more damped system while maintaining a high amplitude ratio in the low frequency region as shown in Fig. 5.5. The desirable ones would be like curve 3 in that figure. The back pressure p_r should not be too large to lower the curve too much like the curve 4 in Fig. 5.5.

The greatest disadvantage of the new configuration is that there is

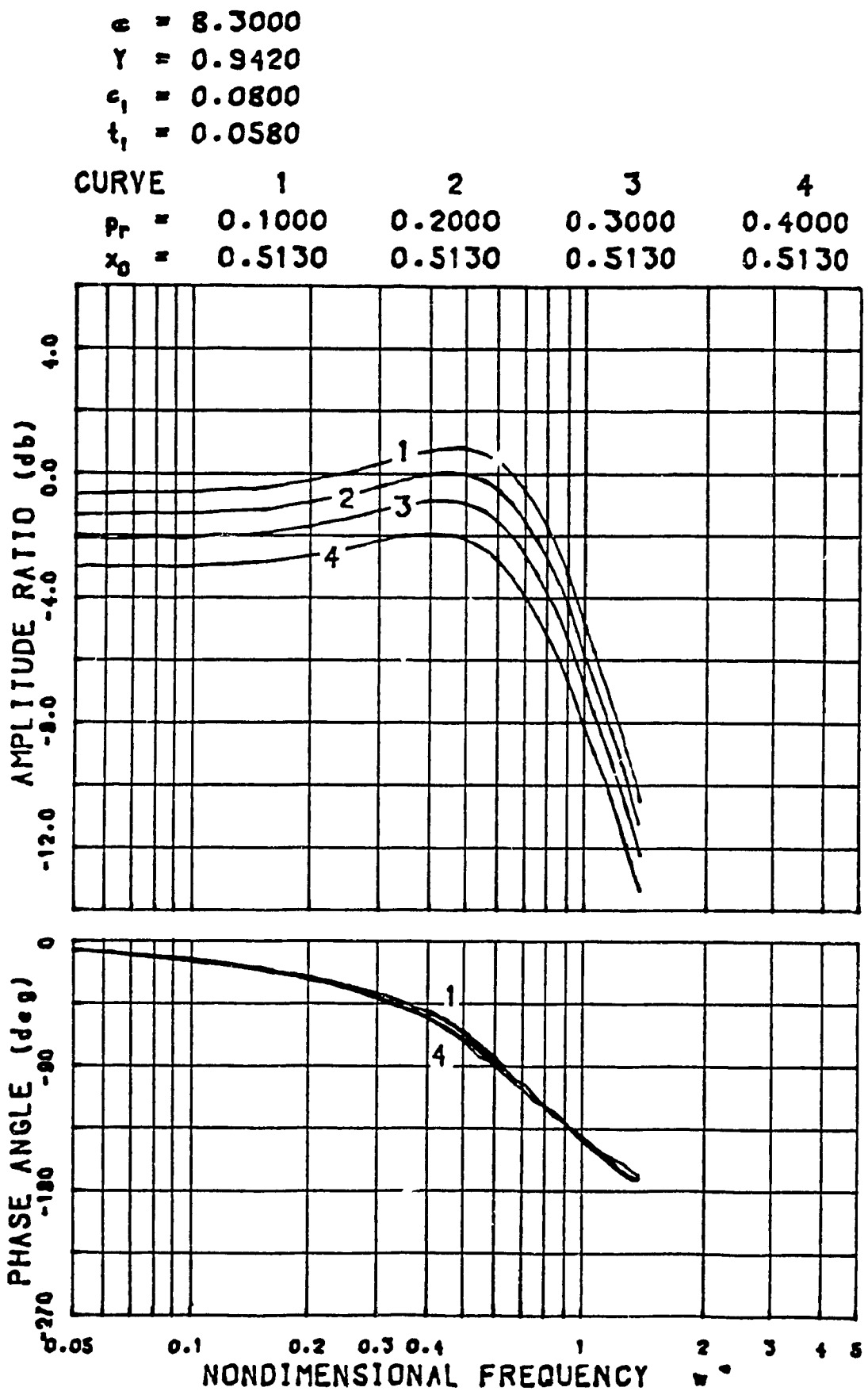

Fig. 5.3 Effect of p_r on the New Configuration Frequency Responses ($v_1 = 0.15 + 0.1 \sin\tau$)

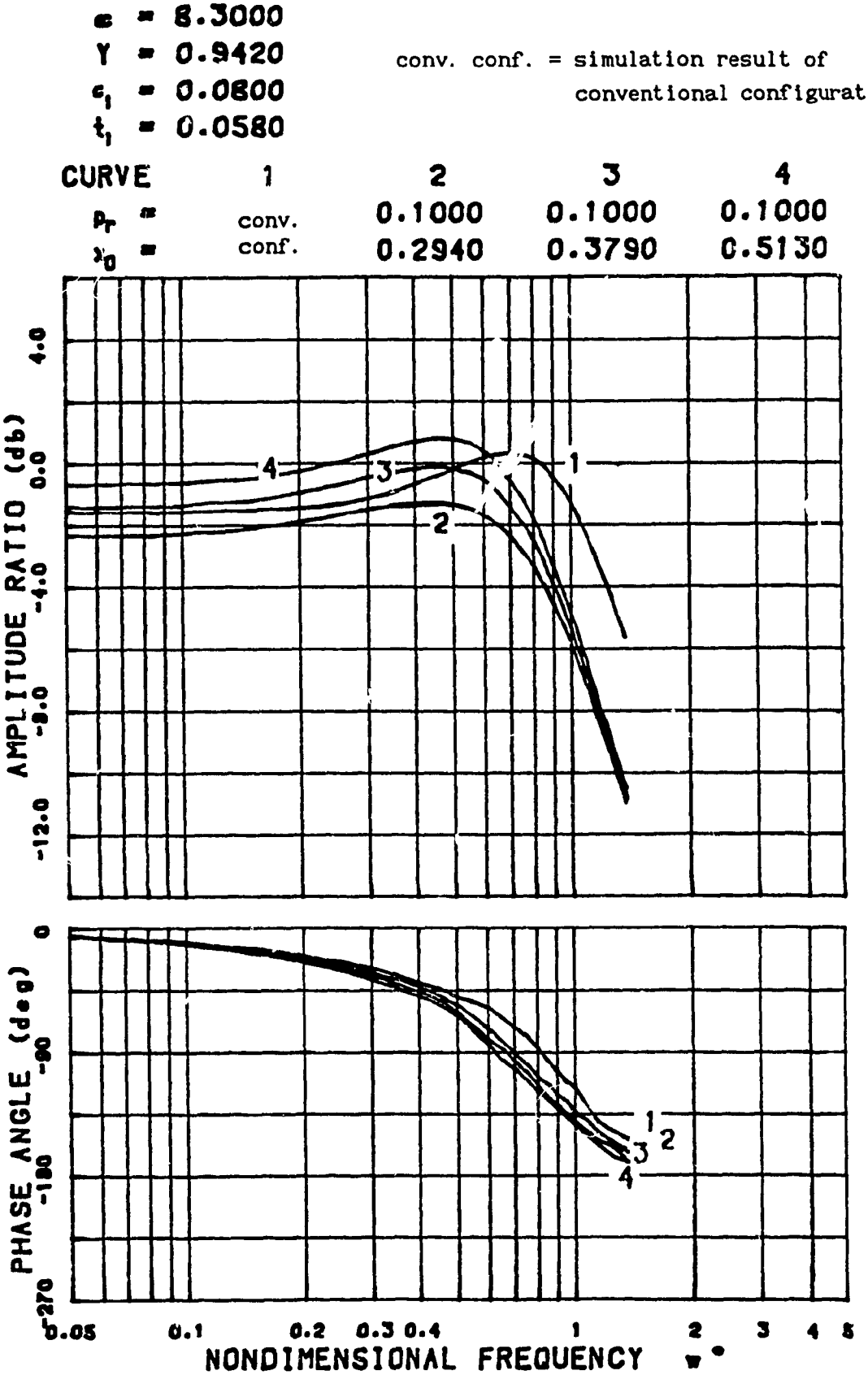

Fig. 5.4 Comparison of the Conventional (Curve 1) and New Configurations Frequency Responses at Different p_r ($v_1 = 0.15 + 0.1 \sin\tau$)

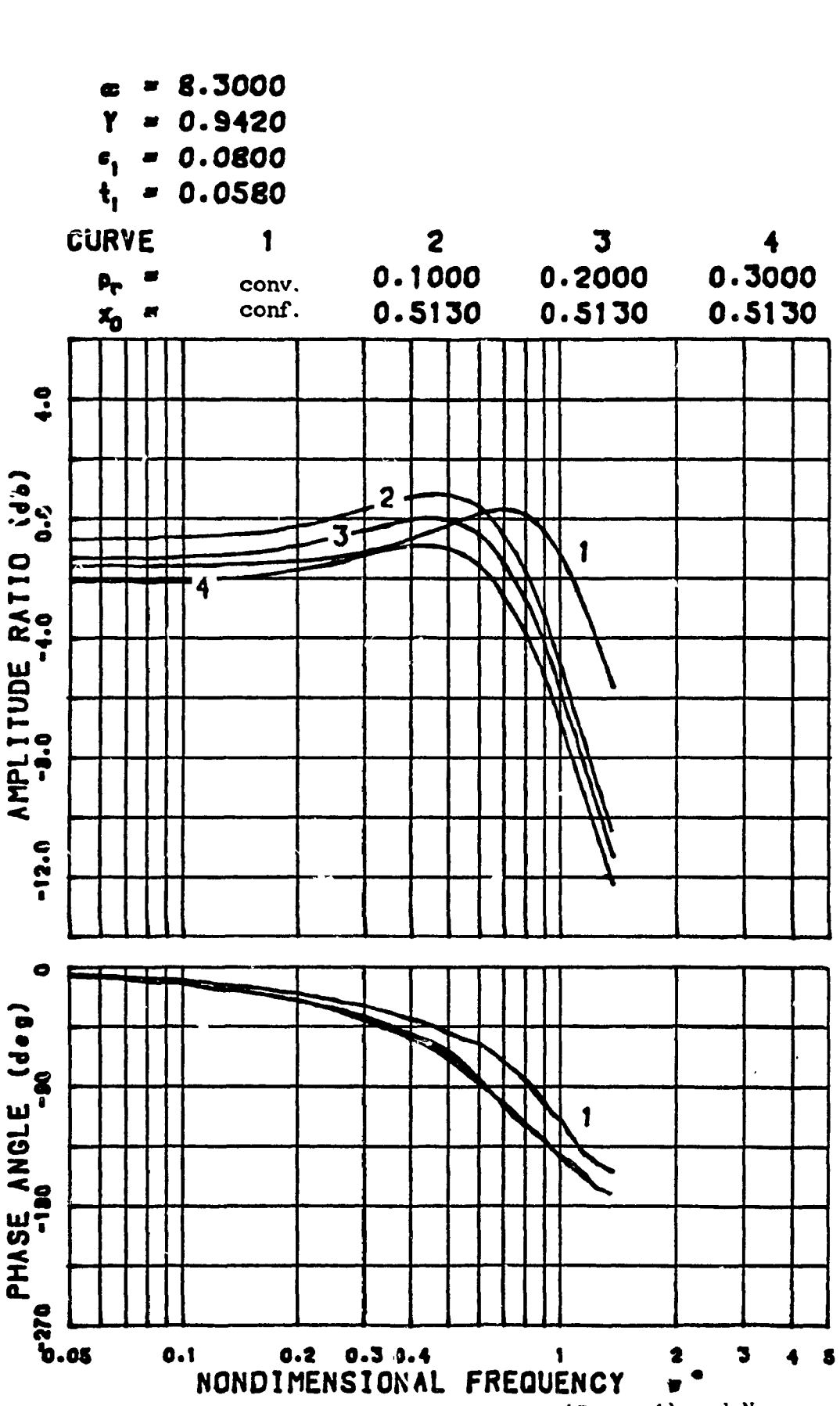

Fig. 5.5 Comparison of the Conventional (Curve 1) and New Configurations Frequency Responses at Different x_0 ($v_1 = 0.15 + 0.1 \sin\tau$)

a decrease of resonant frequency from the conventional configuration (ω^* = 0.7) to the new configuration (ω^* = 0.4 to 0.5), which accounts to a factor of about $1/\sqrt{2}$. This is due to the fact that only one chamber's volume contributes to the oil spring because only one line is controlled by the input signal of varying orifice area, while the other line has a fixed restrictor area. If both lines are controlled by the input signal at the same time as in the conventional configuration, then there are two parallel oil springs and higher resonant frequency can be obtained.

The pairs of curves 1 and 3 in Fig. 5.4 and 5.5 are good examples showing how the new configuration can have a more desirable transient response than the conventional configuration when the restrictor area and back pressure are properly tuned. In the new configuration, the lower resonance peak means a higher damping, while the higher amplitude value at the low frequency region means a higher steady state gain.

5.8 Conclusion

A nonlinear non-dimensional mathematical model has been derived for a conventional and new electrohydraulic servo configuration. The frequency responses of both configurations are investigated using digital computer simulation. The analysis provides an explanation to the previous research based on step input responses which established that with a suitable tuning of the return orifice and back pressure it is possible to obtain a high gain yet high damping servosystem. As observed in this chapter, the new configuration offers a lower resonance frequency. This may limit the utilisation of the new servo

configuration for certain types of applications.

CHAPTER 6

COMPARISON OF EXPERIMENTAL AND SIMULATION RESULTS FOR OPEN LOOP FREQUENCY RESPONSES

6.1 Introduction

A hydraulic rig as described in Ch. 2 was built for the investigation of the frequency responses of the conventional and new configurations. As mentioned before, the hydraulic linear motion system in A. Limaye's work [13] is replaced by a rotary motion system. The new setup has the advantages of having unlimited angular displacement. Also, the hydraulic motor can provide very constant volumes for the two chambers with respect to the angular displacement.

Chapter 5 shows how the new configuration has the advantageous characteristics over the conventional configuration of having higher damping and lower overshoot. However, the simulation also predicted a significant drop of damped natural frequency in the new configuration, which leads to the same reference to non-dimensionalise the input frequency.

In this chapter, comparison of experimental readings on frequency responses at different offset levels, restrictor areas and relief valve settings are carried out. The results are then nondimensionalised and compared with simulation results to see if there is any discrepancy and give explanations.

6.2 Experimentation Performance for Frequency Responses

The loading pump is disconnected from the main shaft for the frequency response experiments because the loading torque depends not only on the orifice area of the loading servovalve, but also on the speed of the rotating shaft. The latter prevents a constant loading torque but adds complication to the overall transfer function by interweaving the two hydraulics systems together. Moreover, if the torque signal from the torque transducer is negatively fedback to the servoamplifier in an attempt to give a constant loading torque, then unstable output is observed. It is because an increase in the loading servovalve orifice area will decrease the resistance, increase the flow but decrease the loading torque, creating a positive feedback effect so that the servovalve area will increase indefinitely. The loading pump is removed to achieve the primary purpose of the investigation of the frequency responses of both configurations of the servomotor system.

Besides unlimited angular displacement, the new setup has a lot of advantages. The static and dynamic frictions are rather small. The performance of the back pressure relief valve is very desirable as it can maintain a very constant back pressure even though there is an offsetted sinusoidal input command. Moreover, the output waveforms from both configurations have only little distortion so that the amplitude ratio and phase lag can be measured easily. Sinusoidal waveforms for testing have been input to the experimental setup. The output waveforms of the new configuration show the presence of shock waves in the oil because of the time delay effect of the directional control valve such

that the output waveform cannot be distinguished above 7 Hz. (Appendix III)

The switching problem of the directional control valve is overcome by adding an offset to the input. The temperature of the oil is monitored by placing a thermometer on the return line before the tank. Output readings are only taken at the temperature range of 40 to 50^{o}C to limit the error coming from the temperature variation. It is also found that if the input offset velocity is too high (higher than 500 r.p.m), the responses become overdamped. There is also a problem of large ripple voltages from the tachometer output when the speed is too high. The ripples make it difficult to read the amplitude and phase lag of the output. Carrying out the frequency responses at small offset removes the problems of the heating up of bearing and oil, overdamped responses and the ripple voltages.

6.3 Comparison of the Experimental and Simulation Results for Open Loop Frequeccy Responses

A signal of 0.3 + 0.15 sinωt V is input to the open loop system and the amplifier gain is adjusted to be K_a = 5 mA/V. The output is then non-dimensionalised and plotted against the non-dimensionalised input frequency.

Fig. 6.1 shows the comparison of the experimental Bode diagram for the conventional configuration with that of the simulation. The experimental data is found to match very well with the simulation

ϵ = 8.3000
γ = 0.9420
c_1 = 0.0800
t_1 = 0.0580

CURVE 1

conv. conf.

● - experimental value

conv. conf. = simulation result of conventional configuration

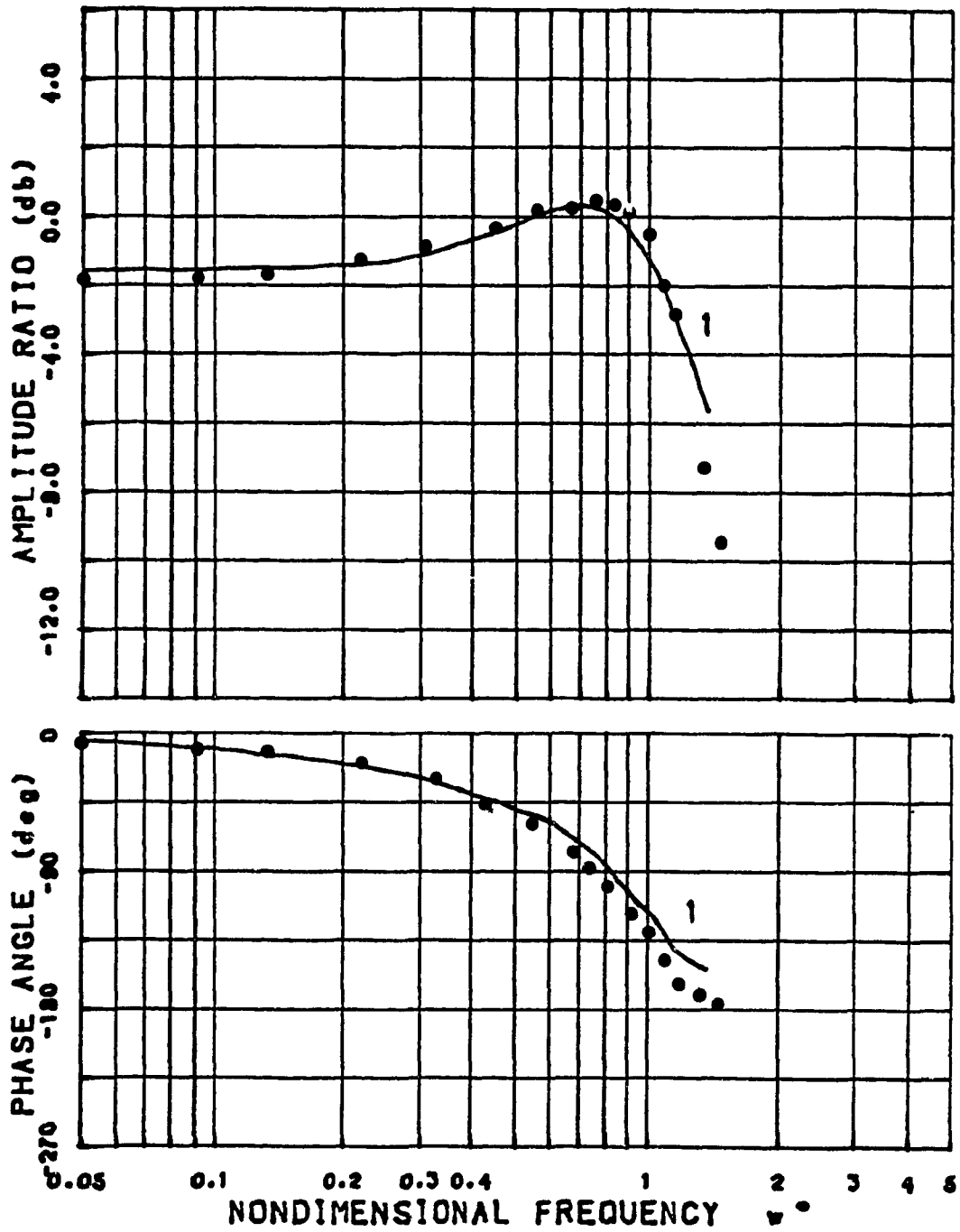

Fig. 6.1 Experimental versus Simulation Values for Conventional Configuration (v_i = 0.15 + C.1 sinτ)

result. The intersection of the high frequency asymptote with the horizontal line of the gain takes place at $\omega^* = 1.05$ or 24 Hz, compared with the predicted natural frequency of 22 Hz. The resonant frequency is found to be 17 Hz. At high frequency, the experimental amplitude ratio and phase lag drops at a faster rate than that of the simulation. It is because of the bigger influence of the high frequency elements.

Fig. 6.2 shows the comparison of experimental and simulation responses at 4 and 6 turns of opening of restrictor (curve 1 and 2 respectively) experimental resonant frequency is about 10 Hz, which is very close to the simulated values. At high frequency, the experimental amplitude ratio and phase lag drop off at a faster rate than the simulation results. The experimental result for curve 2 has a smaller damping than that of the curve 1, agreeing with what is predicted from the simulation.

From Fig. 6.3, it can be seen that the experimental results for the new configuration at the back pressures of 100 psi and 200 psi and at 6 turns of opening of the restrictor agree quite well with the simulation. The resonant frequency is again about 10 Hz and the high frequency region drops off faster than that of the simulation. Slightly larger discrepancies between experimental and simulation results are noticed here. It is also noticed that, with an oscillating input command signal, the varying flowrate of oil through the pressure relief valve can cause the back pressure setting to drop about 6 percent, which is observed from readout of the pressure tranducer located just before the relief valve. The drop in pressure may have been caused by the

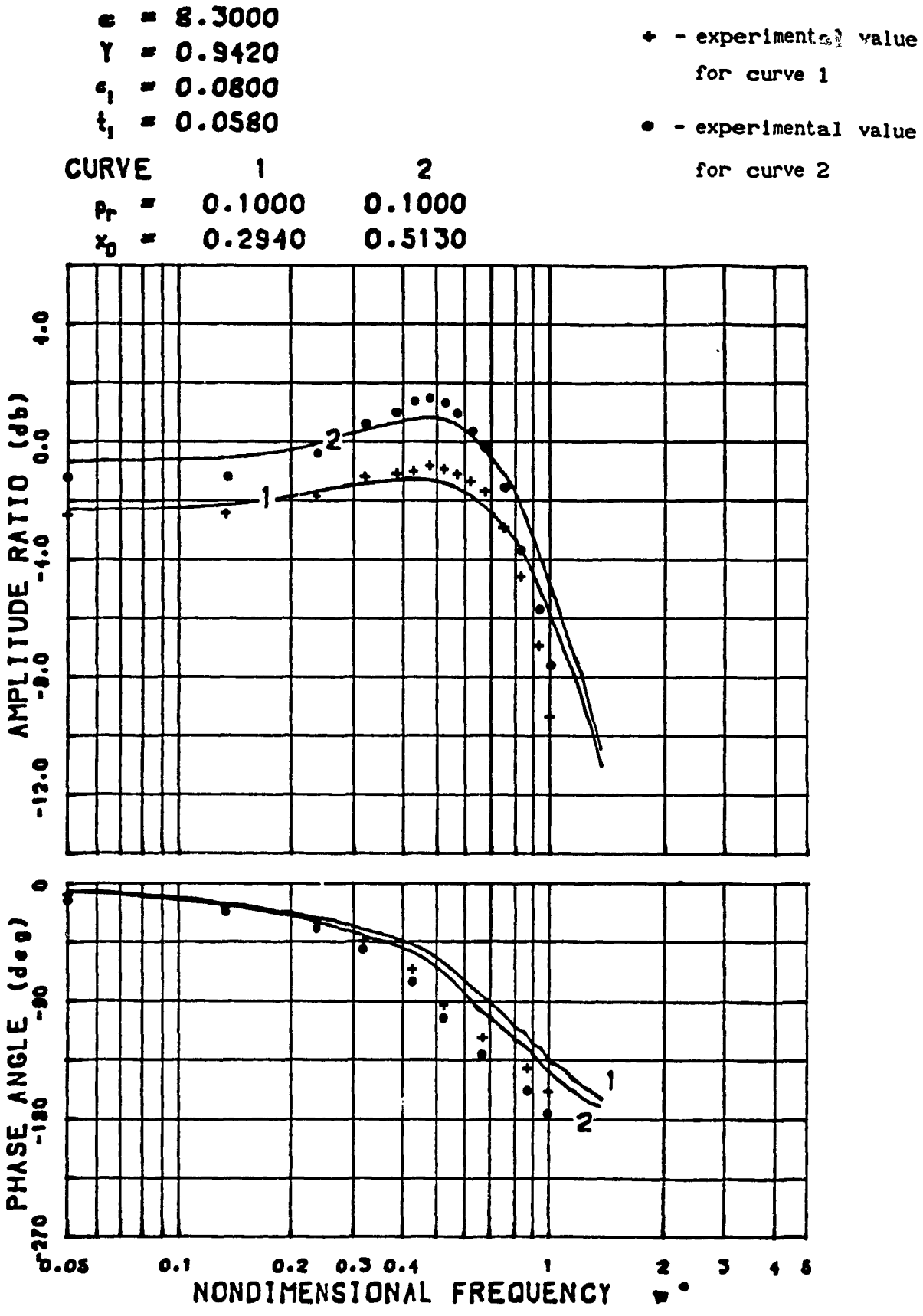

Fig. 6.2 Experimental versus Simulation Values for New Configuration at Different x_0

(v_1 = 0.15 + 0.1 sinτ)

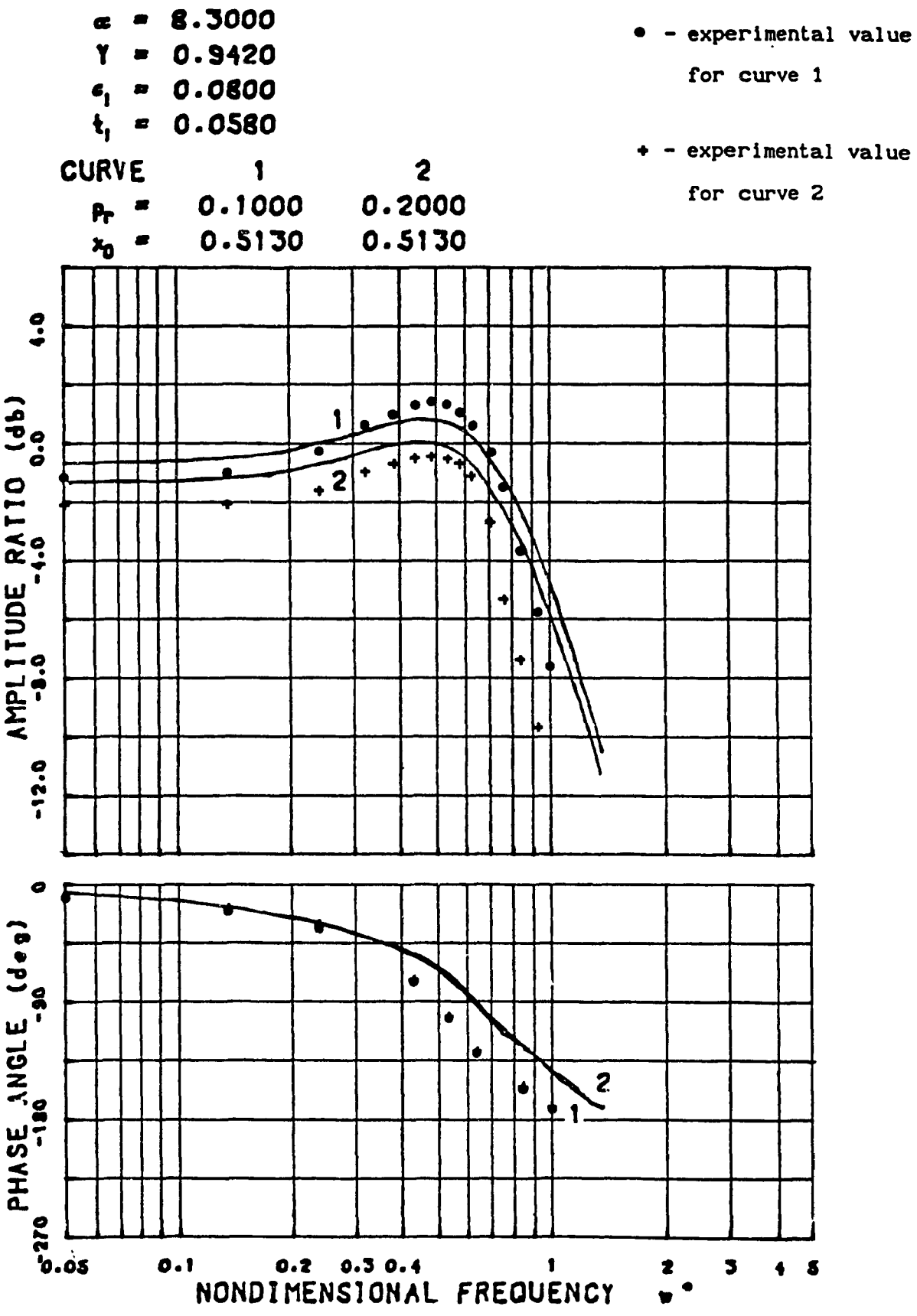

Fig. 6.3 Experimental versus Simulation Values for New Configuration ($v_1 = 0.15 + 0.1 \sin\tau$)

vibration of the valve seat inside the relief valve. The relief valve has once been removed to see the effect of zero back pressure. No significant deviation from the trend shown in Fig. 6.3 was observed. Hence the presence of the relief valve is not responsible for the drop in the resonant frequency in the new configuration.

To have the properties of higher steady state gain and higher damping, suitable orifice area and back pressure should be chosen. From the simulation diagrams in Fig. 5.3 and 5.4, it can be predicted that with 5 turns of opening of restrictor and 100 psi back pressure, the desirable result can be achieved. The experimental and simulation data are shown in Fig. 6.4.

The experimental result demonstrated the existence of the advantageous properties of the new configuration, but with the sacrifice of a lower resonant frequency. Such drop in the resonant frequency comes from the reduction to only one controlled line in the new configuration as mentioned before.

6.4 Conclusion

Based on the comparison of the experimental and the simulation results, it can be concluded as follow :

- The nondimensional mathematical models for both configurations are are correct and provide a method to predict the performance of design under different physical parameters and different tuning or loading

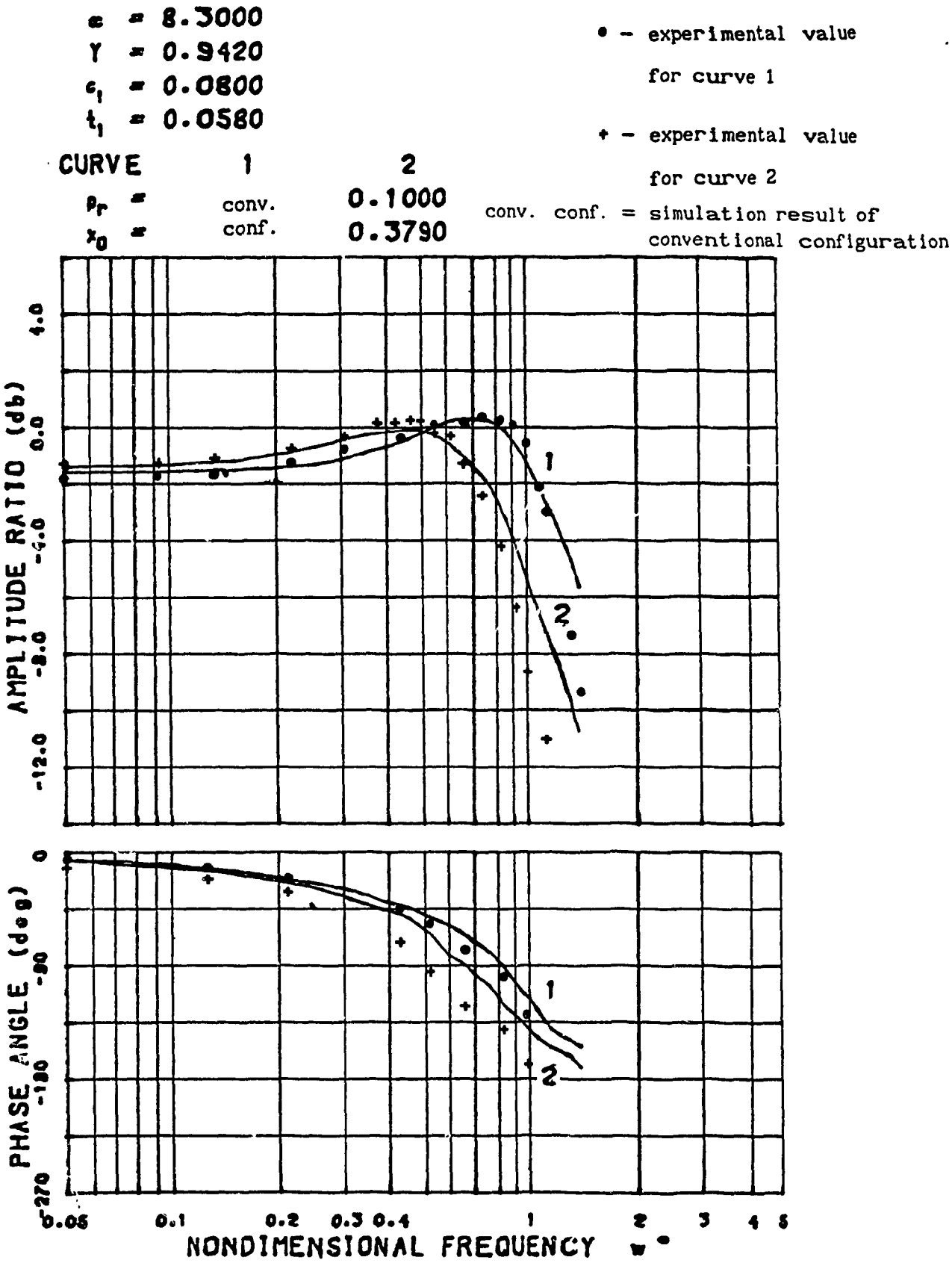

Fig. 6.4 Comparison of Experimental and Simulation Results for the Conventional and New Configurations ($v_1 = 0.15 + 0.1 \sin\tau$)

conditions. It can also be used to compare systems with different physical parameters by transforming them into dimensionless parameters.

- The experiments confirm the decrease of resonant frequency in the in the new configuration as predicted from the simulation although there exists the advantageous characteristics of higher gain and higher damping. Faster drops of amplitude ratio and phase lag in the high frequency region are observed in both configurations.

- The dynamics of the pressure relief valve show only little influence on the overall dynamics.

CHAPTER 7

OPERATING ZONE DETERMINATION METHOD

7.1 Introduction

In chapter 5, nondimensional Bode diagrams are plotted to investigate the frequency responses of the nondimensional mathematical model of the experimental setup. From the simulation, it is found possible to obtain a higher gain yet higher damping in the new servosystem when the return orifice area and back pressure are properly tuned. The experimental results in Chapter 6 have shown that they match very well with the simulation results.

This chapter gives the procedures to define the operating zone of the open loop system by computer based on the mathematical model of the experimental setup. The boundaries are defined for the combinations of orifice area and back pressure such that the new configuration can have an improved frequency response inside them.

7.2 Defining the Boundaries

Despite the drop in the damped natural frequency in the new configuration, emphasis has been placed on the condition of higher steady state gain and higher damping. It has been found in Chapter 5 that, for the new configuration, when x_o increases, the curve profiles converge upwards with decreasing distance between the steady state gain

and the pe' . value. In the procedure, the steady state gain and the peak value of the conventional configuration are computed first and then stored. Calculations follow by putting $p_r = 0.0$, and then the value of x_o is increased from a very small value and iterated until the steady state gain converges with that of the conventional configuration. It contributes to the lower limit boundary of the operating zone. x_o is then increased and iterated again until the gain at the peak equals to that of the conventional configuration. It then contributes to the upper limit boundary of the operating zone. The difference between the peak and the steady state gain values in the new configuration should not b· larger than that of the conventional configuration for the operating zone to exist. Fig. 7.1(a) and (b) show the conditions for the definition of lower and upper boundary limits at $p_r = 0.0$.

p_r is now raised in steps of 0.05, the lower and upper limits being calculated each time. Fig. 7.2 is the master diagram showing the boundaries of the operating zone of the nondimensionalised model of the experimental setup with an input of $0.15 + 0.1 \sin\tau$. Other figures of the operating zones show the change in the input offsets or loading conditions from it. The data on the footnote of the diagram give the values of the steady state gain, gain at the peak and the damped natural frequency of the conventional configuration. At $p_r = 0.1$, the lower and upper boundary limits exist (Fig. 7.3(a)) and the difference between them is sma?l. When p_r increases, the difference widens and the boundaries bend upwards. However, at $p_r = 0.30$, when x_o increases, the response curves converge with the peak value being less than that of the conv· ıtional configuration (Fig. 7.3(b)). Hence, even with x_o increased

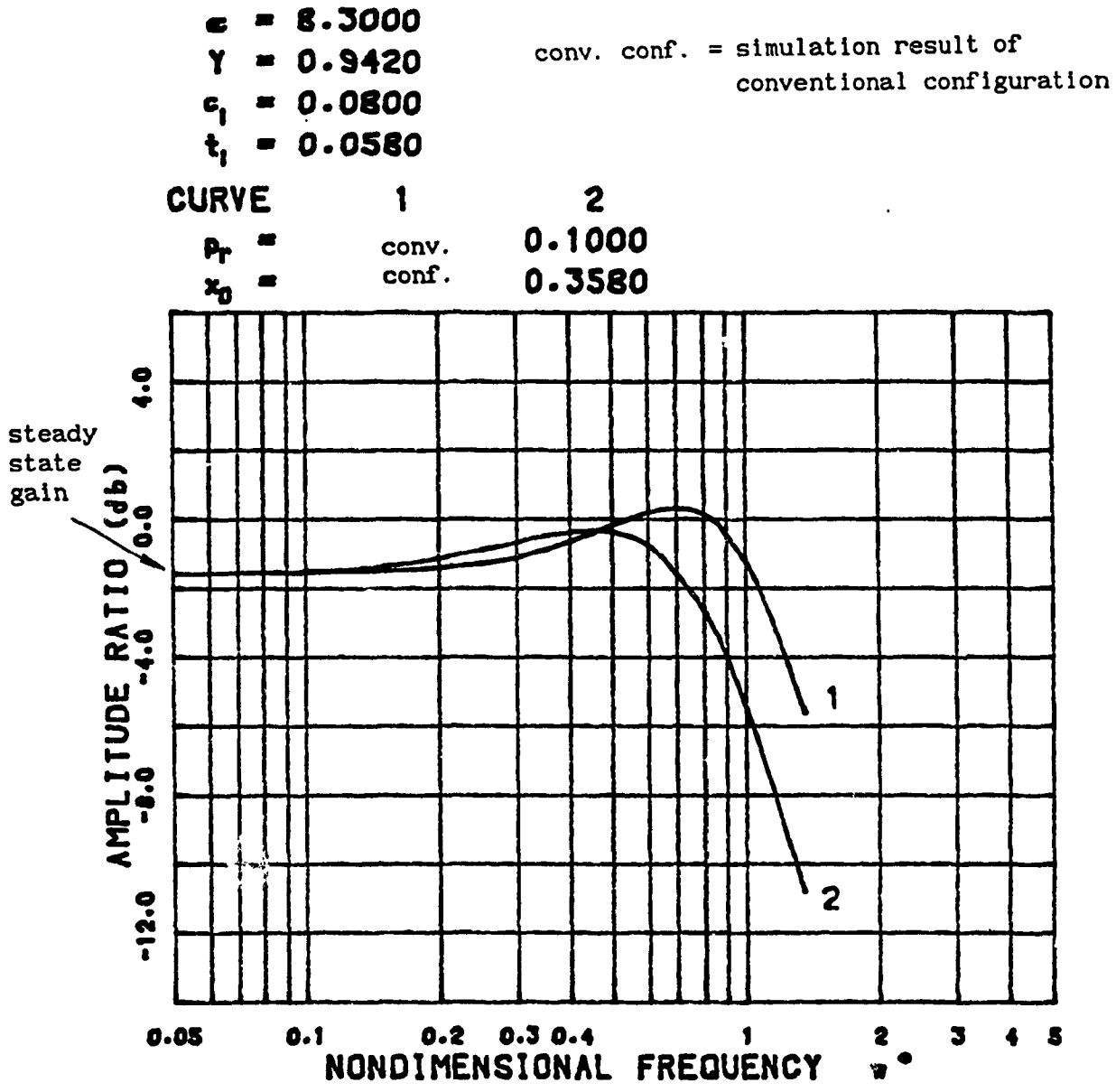

Fig. 7.1(a) Bode Diagram Showing the Lower Boundary from the Steady State Gain

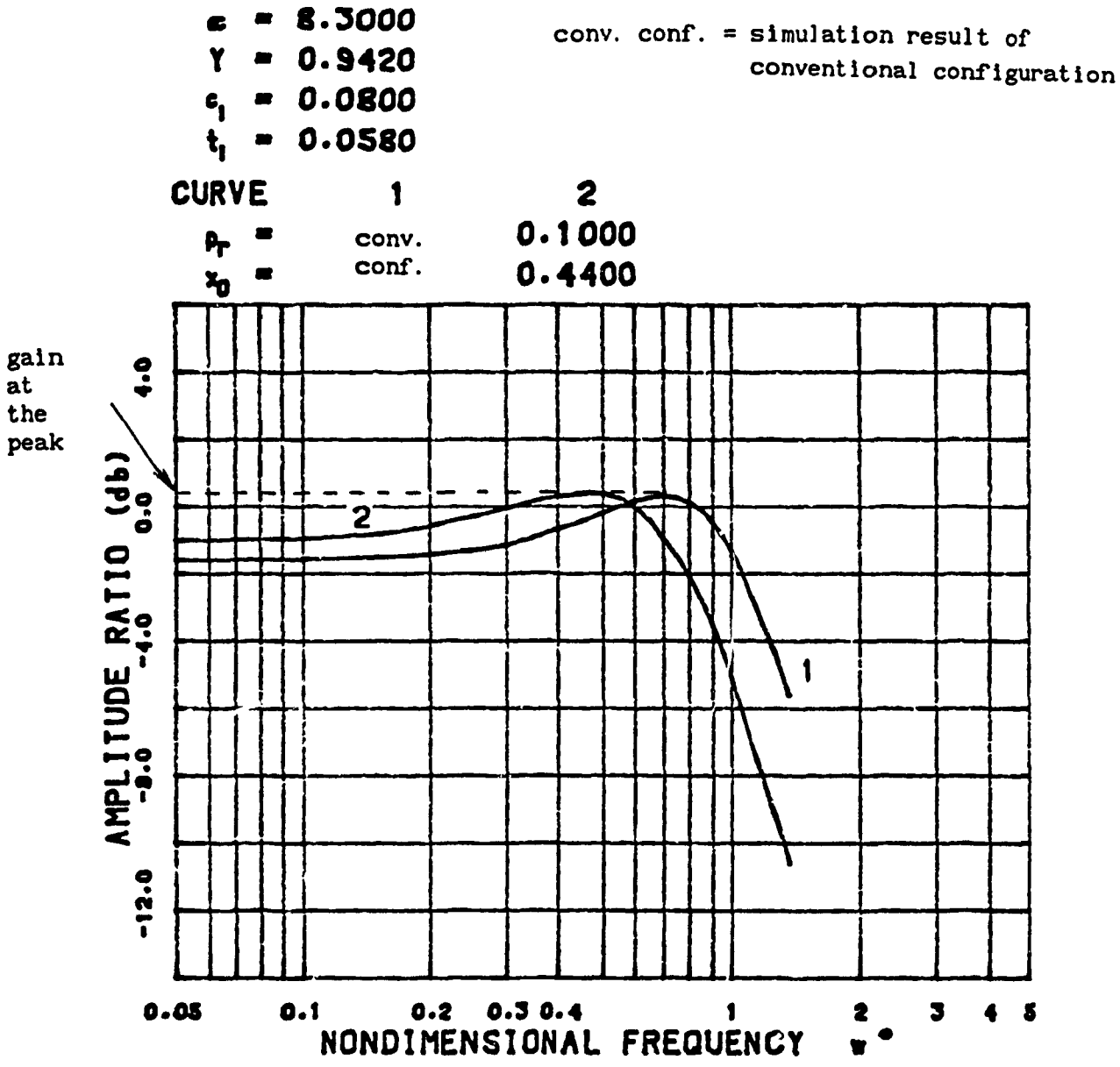

Fig. 7.1(b) Bode Diagram Showing the Upper Boundary from the Gain at the Peak

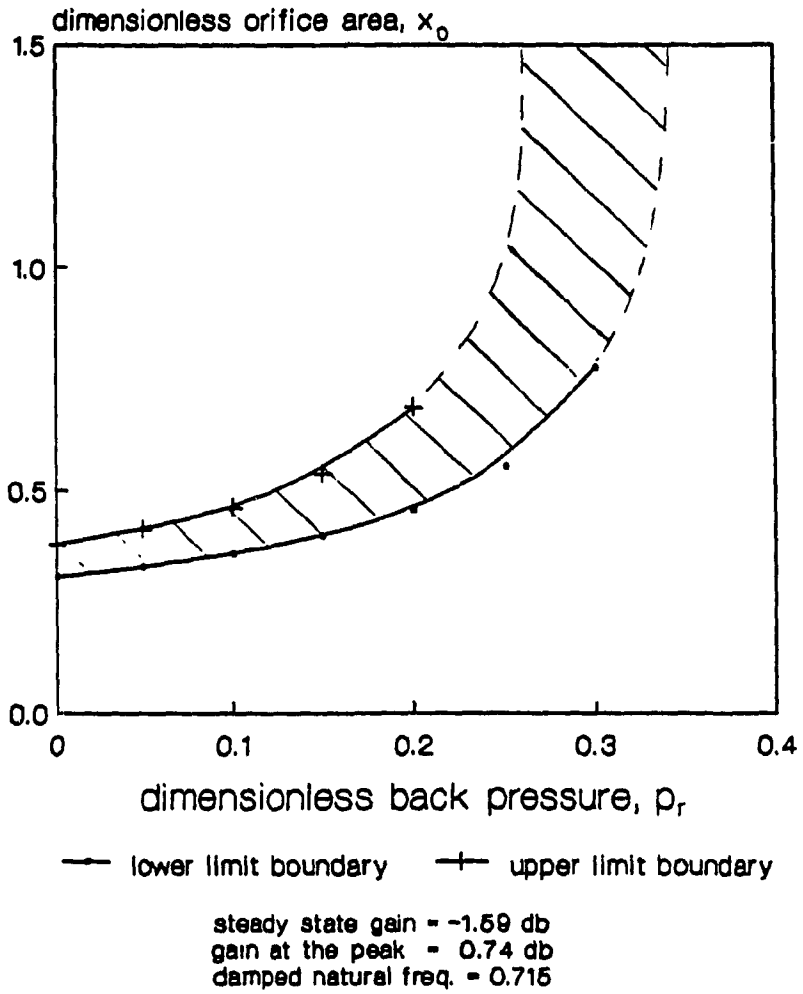

Fig. 7.2 Master Graph Showing the Operating Zone at $v_i = 0.15 + 0.1 \sin\tau$

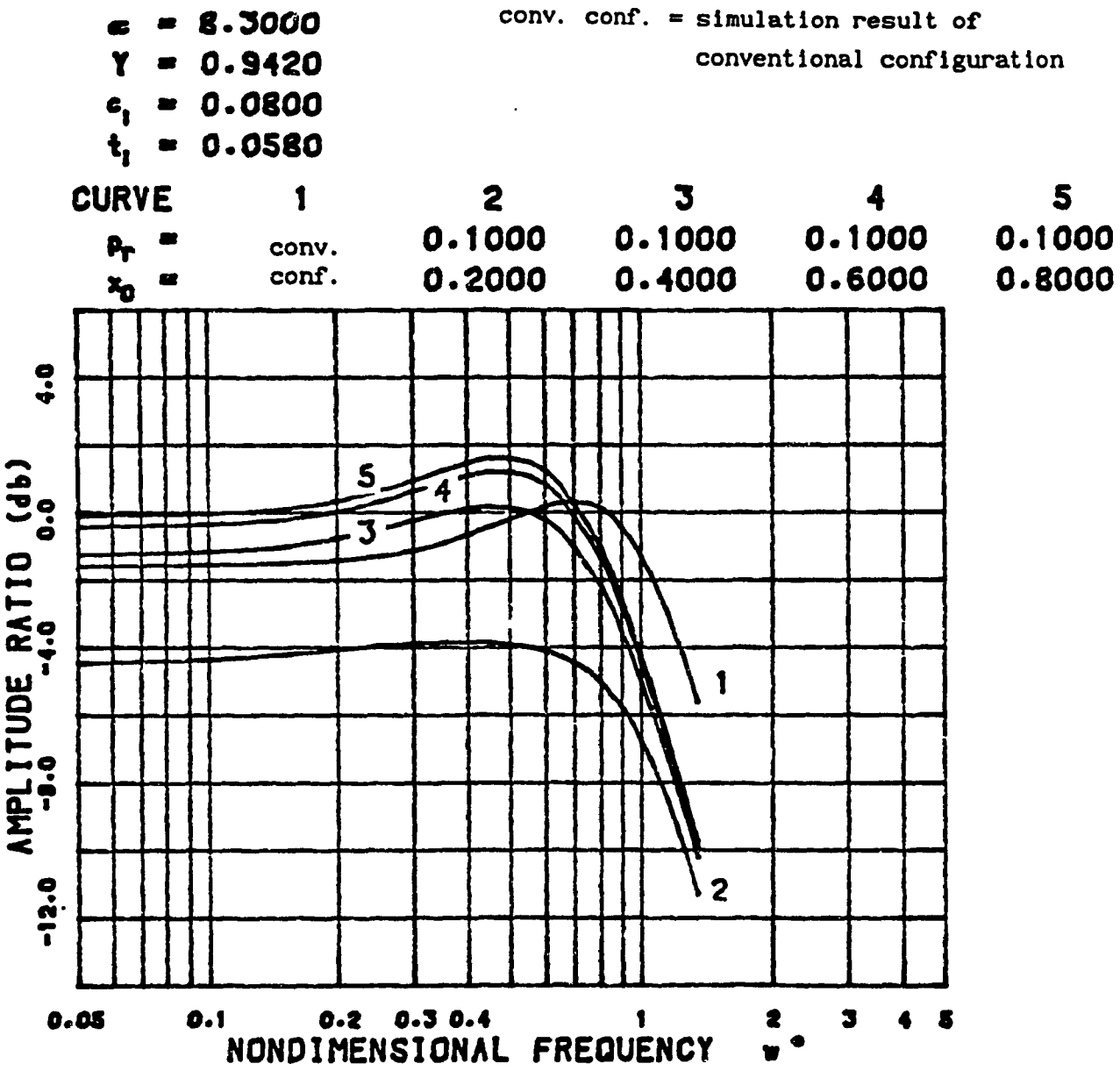

Fig. 7.3(a) Bode Diagram Showing the Existence of Lower and Upper Limit Boundaries at $p_r = 0.1$

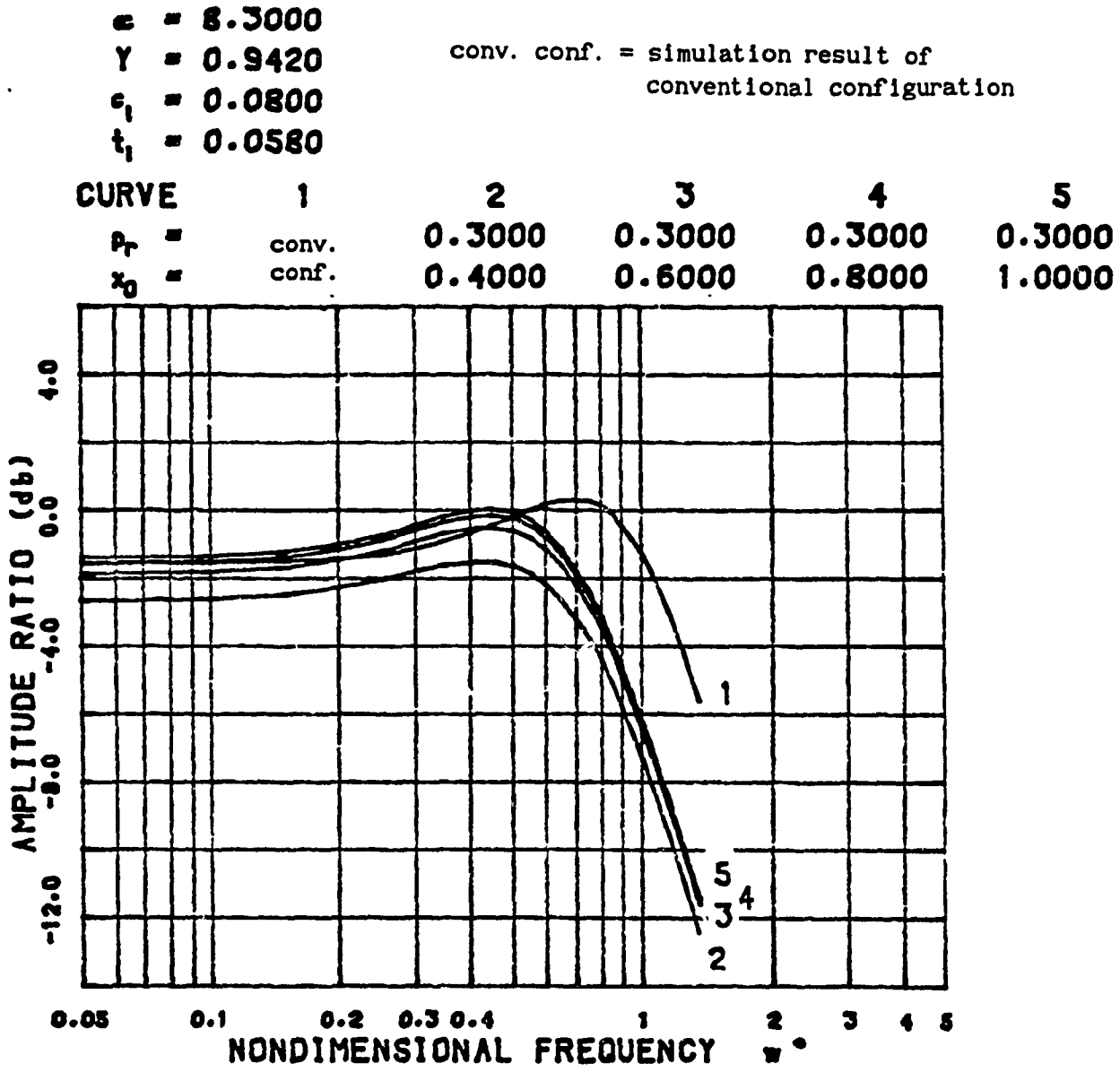

Fig. 7.3(b) Bode Diagram Showing that the Curves of New Configuration Converges before Having an Upper Limit Boundary

to infinity, the system still stays within the operating zone. At p_r = 0.40, the curves converage so fast that its steady state gain cannot reach that of the conventional configuration so that the operating zone does not exist at that back pressure or higher values (Fig. 7.3(c)).

In Fig. 7.4 and 7.5, the offset value of the input signal has been changed to 0.1 and 0.2 respectively. The operating zone in Fig.7.4 is found widened and shifted to the bottom and the right hand side. It means that the system requires a smaller x_o but higher p_r to stay within the operating zone. The reverse is true for the case in Fig. 7.5.

The effect of loading on the frequency response of the system could not be studied from the experimentation. From the operating zone determination method, the effect can be examined. From Fig. 7.6, it can be seen that if the torque load factor is doubled, at p_r = 0.0, the lower and upper limits remain nearly the same as that in Fig. 7.2. When p_r increases, the operating zone bends upward faster and widens more. The maximum allowable back pressure is lower than that in Fig. 7.2 in order for the system to stay within the operating zone. The effect is more prominent with the torque load factor quadrupled in Fig. 7.7.

Conclusively, with higher offset relative to the amplitude of the sinusoidal signal and higher torque load factor, the operating zone is smaller and shifts to the lower back pressure region.

The damped natural frequencies of the new configuration compared to the conventional configuration are shown as follows:

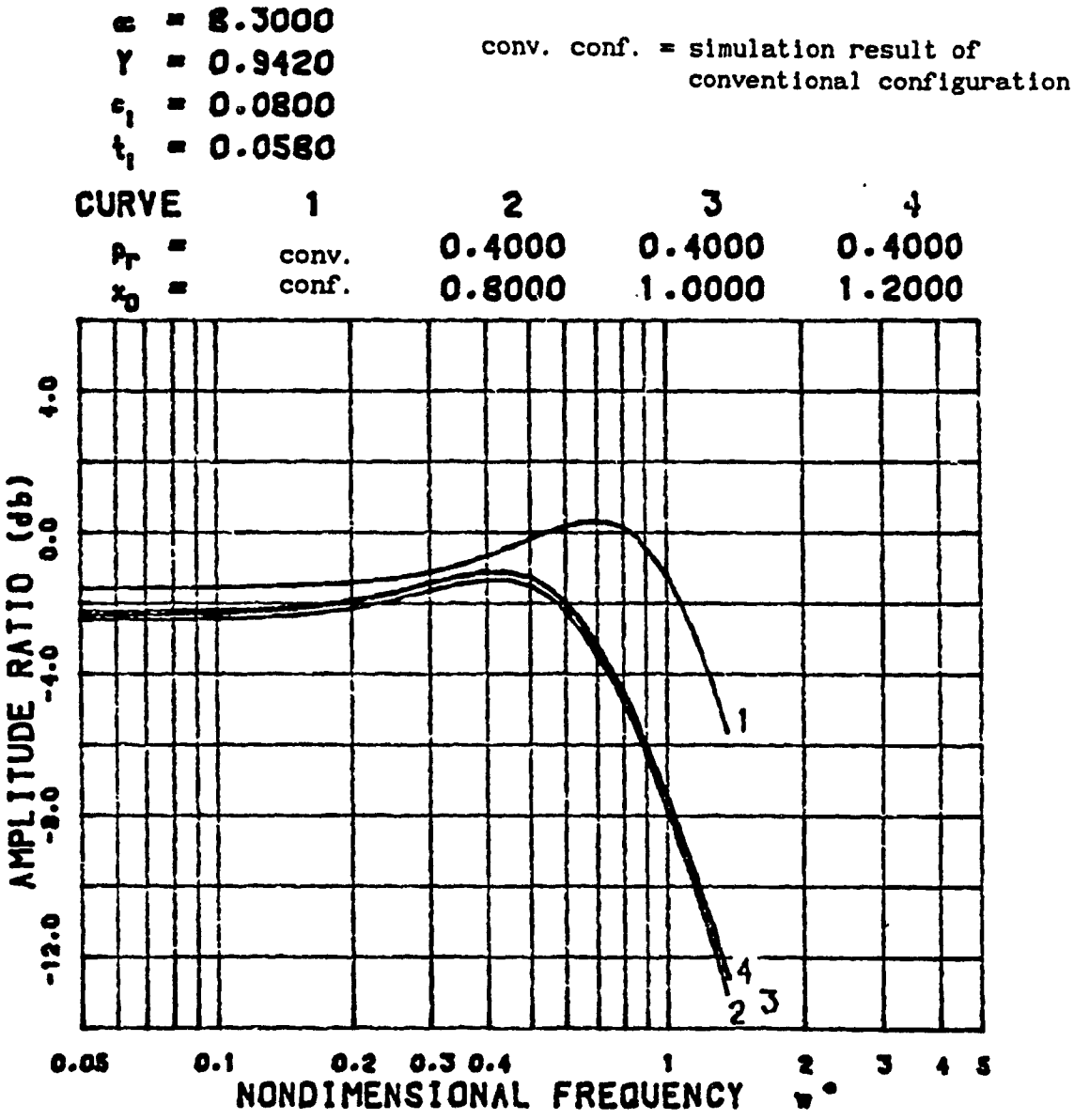

Fig. 7.3(c) Bode Diagram Showing that the Curves of New Configuration Converges before Having an Lower Limit Boundary

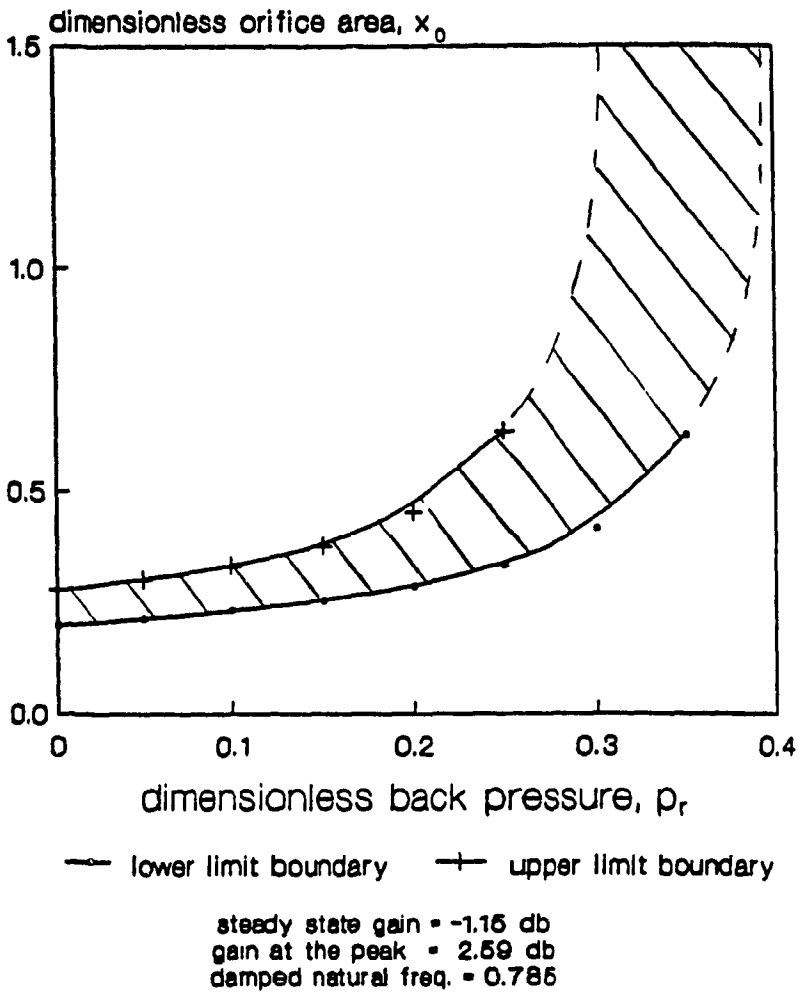

Fig. 7.4 Operating Zone at Reduced Input Offset from Fig. 7.2

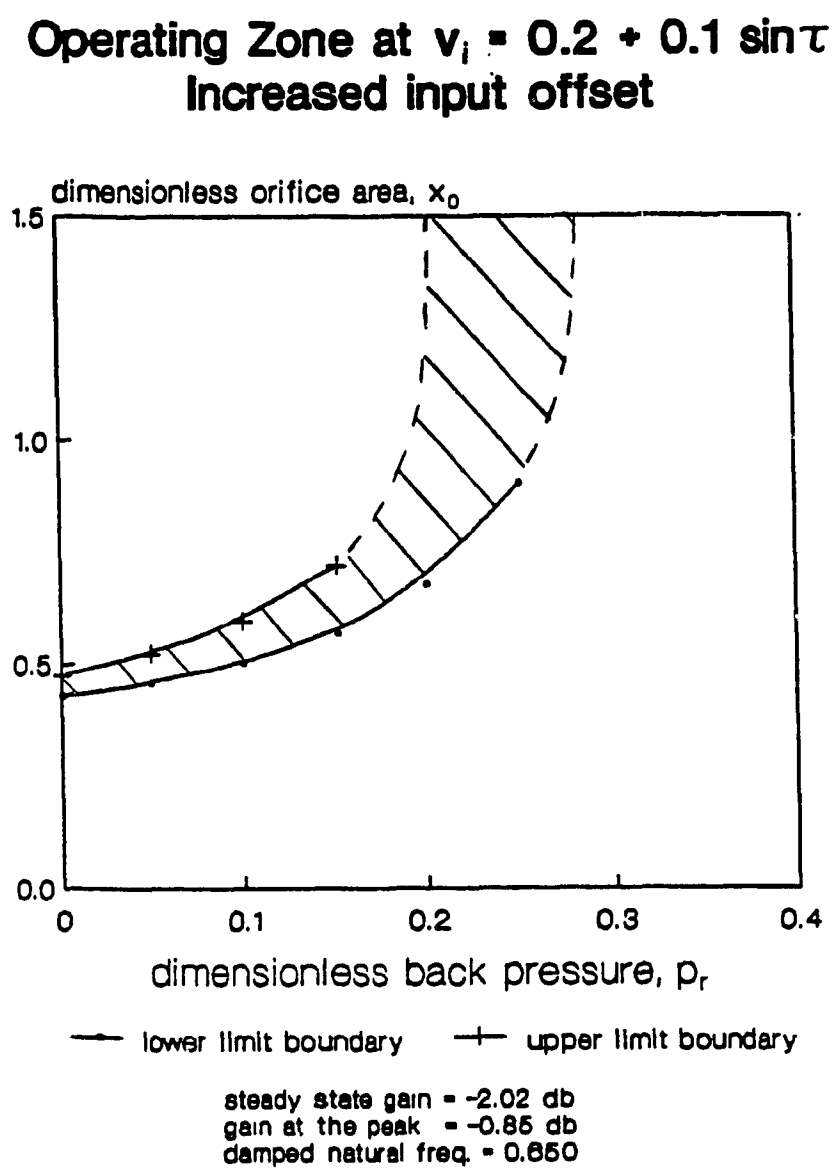

Fig. 7.5 Operating Zone at Increased Input Offset from Fig. 7.2

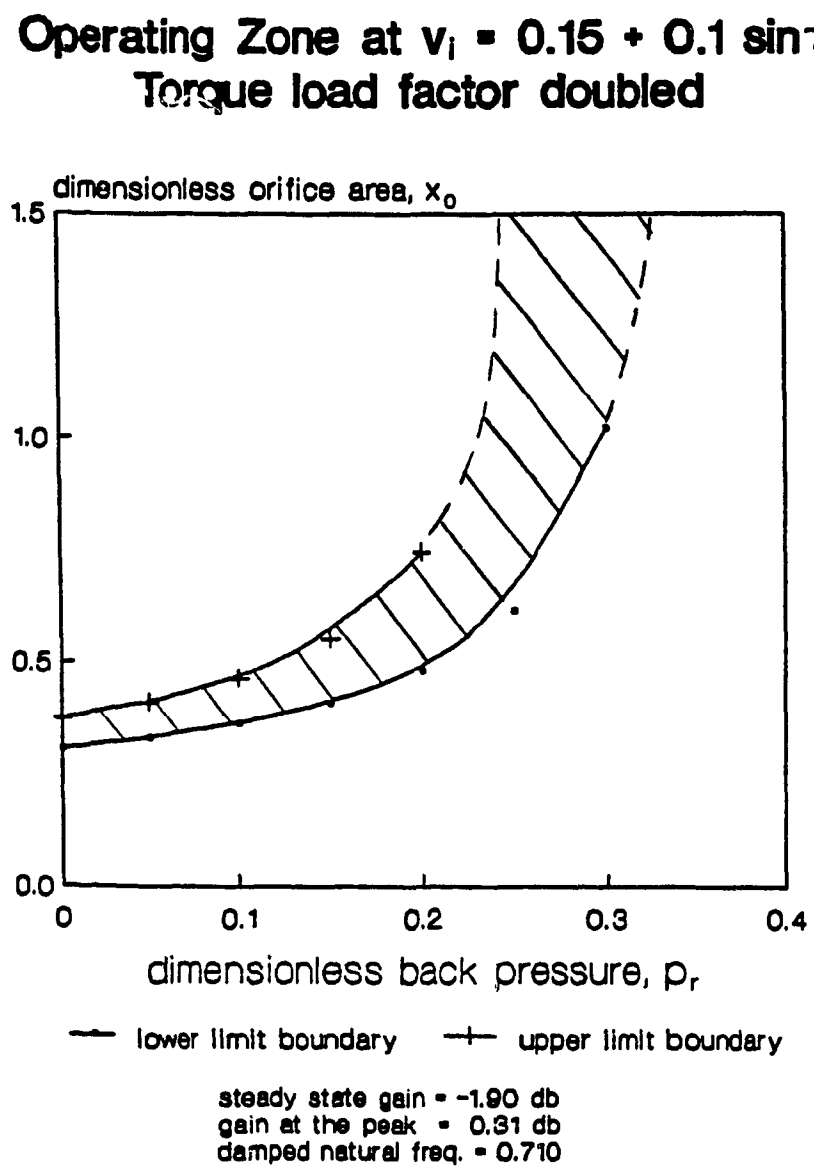

Fig. 7.6 Operating Zone at Doubled Torque Load Factor from Fig. 7.2

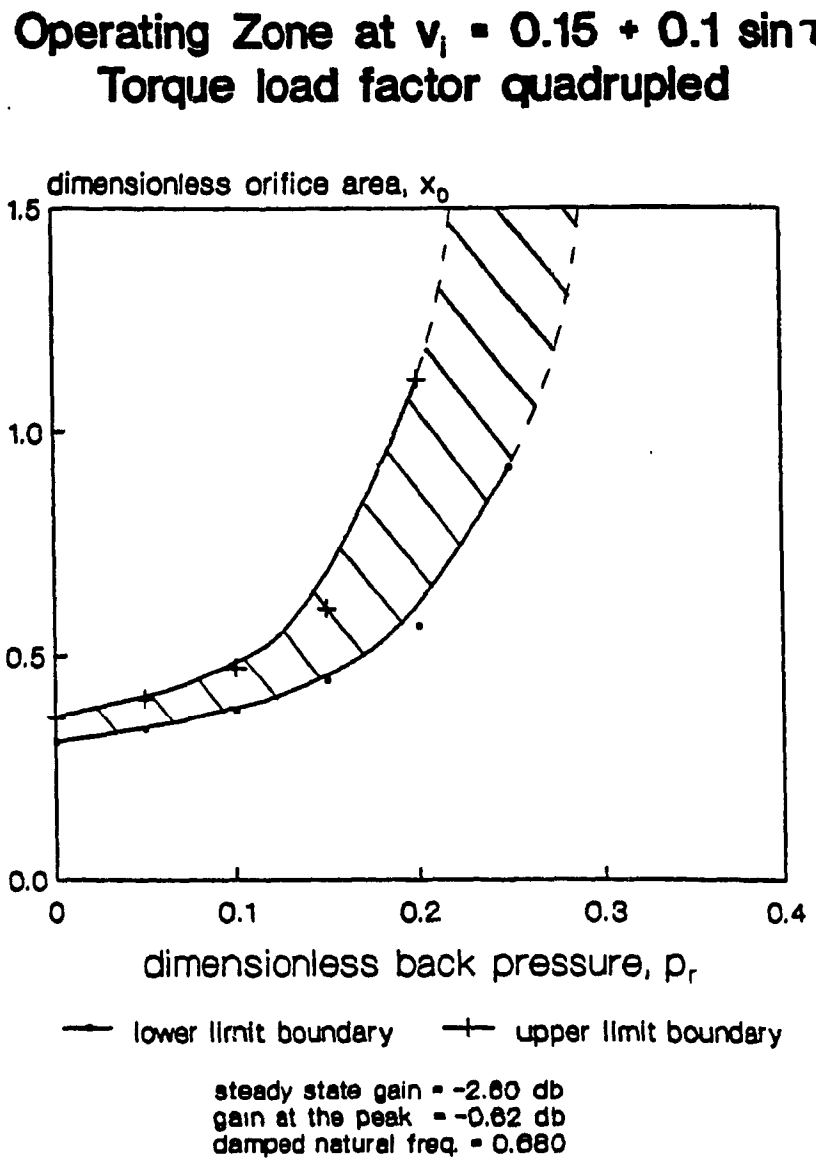

Fig. 7.7 Operating Zone at Quadrupled Torque Load Factor from Fig. 7.2

	Range of ω_d^* in new conf.	ω_d^* in conv. conf.	$1/\sqrt{2}$ of ω_d^* in conv. conf.
Fig. 7.2	0.480 to 0.470	0.715	0.506
Fig. 7.4	0.535 to 0.525	0.785	0.555
Fig. 7.5	0.420 to 0.390	0.650	0.460
Fig. 7.6	0.475 to 0.465	0.710	0.502
Fig. 7.7	0.460 to 0.440	0.680	0.481

The second column indicates the drop of ω_d^* from $p_r = 0.0$ to ω_d^* of highest possible p_r in the boundary limits. They are only slightly less than $1/\sqrt{2}$ of that of the conventional configuration.

7.3 Application of the Operation Zone Determination Method

Given an experimental setup with all the experimental parameters known, they can be nondimensionalised by a computer for simplification and generalisation. It is also possible to compute the operating zones from different inputs or loading conditions. It provides the practical application of determining whether the system can have an operating zone and, if there exists such a zone, how does it look like and how does it change with the inputs and loading conditions. On-line real time computer control can be developed by monitoring the system with the computer and then sending out control signals to the tuning parameters such that the system always stays within the operating zones inspite of the change of inputs and loadings.

7.4 Conclusion

A method for operating zone determination method has been devised to examine the effects of the input signal and loading on the operating zone of the new configuration. Higher offset voltage signal relative to the amplitude of the sinusoidal signal and higher torque load factor are found to give a smaller operating zone and shift the zone to the region of lower back pressure.

The method for determination of the operating zone can be implemented on the computer for real time control of the new servosystem so that there can always be higher steady state gain and higher damping inspite of the inputs and loadings.

CHAPTER 8

CONCLUSION AND EXTENSION

This thesis is the extension of the research work by A. Limaye [13]. The linear actuator circuit by Limaye has been replaced by the rotary motor-pump combination so that the unlimited angular displacement can be used for frequency response analysis. The experimental setup was tested for the dynamic responses and the advantageous characteristics of higher damping and higher steady state gain were observed when the return orifice area and back pressure were properly tuned. However, the damped natural frequency is found only to be about $1/\sqrt{2}$ of that of the conventional configuration. The settling time of the dynamic responses is also found increased. A nondimensionalised mathematical model has been built for the frequency response to simplify and generalise the problem. The simulation and experimental results are then compared. The model is found to be able to predict the frequency response of the two servosystem configurations very well.

An operating zone determination method is devised to define the lower and upper boundary limits of the zone under different input and loading conditions to obtain higher damping and higher steady state gain. Such method can be extended to real-time on-line computer adaptive control.

Other further extensions on this research work can include the following :

1. Open-loop frequency response analysis is usually sufficient for a linear system because it can be used to estimate the transfer function of the system. It can also be used to predict the stability of the closed-loop system. As the new servosystem configuration under investigation is highly nonlinear, the closed-loop frequency response of the system should also be investigated.

2. As the new system is found to have a lower damped natural frequency, an optimisation program should be developed so that its influence on the settling time can be examined.

3. The experimental setup consists of a hydraulic loading circuit, which is not included into the frequency response analysis because of its complicated interwoven nature with the driving portion. However, such loading method is very effective and can be studied as a new research area.

4. Shock waves inside the directional control valve are observed during the experimentation. They come from the sudden opening of the valve after the switching time delay. The time delay can also contribute to the instability of the response. Moreover, the directional control valve used in this research cannot switch properly when the switching frequency is higher than 8 Hz. All these adverse effects should be further studied or a faster switching valve should be chosen.

5. In the conventional configuration, the oil is first throttled

through the variable orifice between the body and the spool of the servovalve, then it goes to the loading element and is throttled again in the variable orifice on the other end of the spool before going back to the tank. The flow forces acting on the faces of the spool lands balance each other and the system becomes stable. In the new configuration, the return port has been blocked so that the flow forces act only on one spool land's face. The unbalanced force acting on the spool can affect the transfer function and stability of the system. The magnitude and significance of such effect should be investigated analytically and experimentally.

REFERENCE

1. Maskrey R.H. and Thayer W.J., "A Brief History of Electrohydraulic Servomechanism", Trans. of ASME, Journal of Dynamic Systems, Measurement and Control, Vol. 100, June 1978, pp 110-116.

2. Pegasus Servovalves, "Two and Three-Stage Series, Internal Operation", Koehring-Pegasus Division, PSV 076, Troy-Michigan.

3. Pegasus Servovalves, "Two-Stage Series, Strong on Performance", Koehring-Pegasus Division, PSV 279, Troy-Michigan.

4. Thayer W.J., "Transfer Functions for Moog Servovalves", Moog Inc. Controls Division, East Aurora, N. Y., Technical Bulletin 103, 1965.

5. Niemas F.J. Jr., "Understanding Servovalves and Using Them Properly", Parts 1, 2 and 3, Hydraulics and Pneumatics Magazine, Oct., Nov., Dec. 1977.

6. Nikiforuk P.N., Ukrainetz P.R. and Tsai S.C., "Detailed Analysis of a Two-Stage Four-Way Electrohydraulic Flow-Control Valve", J. Mech. Engg. Sci., Vol. 11, No. 2, 1969, p. 168.

7. de Pennington A., 't Mannetje J.J. and Bell R., "The Modelling of Electrohydraulic Control Valves and its Influence on the Design of Electrohydraulic Drives", J. Mech. Engg. Sci., Vol. 16, No. 3, 1974, p. 196.

8. Martin D.J. and Burrows C.R., "The Dynamic Characteristics of an Electrohydraulic Servovalve", Trans. of ASME, Journal of Dynamic Systems, Measurement and Controls, Dec. 1976.

9. Kaneko T., "A Research on Electrohydraulic Pressure Control Servovalve", Bulletin of JSME, Vol. 21, No. 155, May 1978.

10. LeQuoc S., Cheng R.M.H. and Limaye A., "A Tuneable Electrohydraulic Servovalve Configuration to Achieve High Actuator Velocity, Fast Response and High Damping", ASME paper 84-WA/DSC-11, New Orleans, U.S.A., Dec. 1984.

11. LeQuoc S., Cheng R.M.H. and Limaye A., "A New Configuration for Electrohydraulic Velocity Control", The Journal of Fluid Control Including Fluidics Quarterly, Dellbridge Publishing Co., Vol. 17, No. 1, 1986, pp 45-64.

12. LeQuoc S., Cheng R.M.H. and Limaye A., "Investigation of an Electrohydraulic Servovalve with Tunable Return pressure and Drain Orifice", Trans. of ASME, Journal of Dynamic Systems, Measurement and Control, Vol. 109, Sept. 1987.

13. Limaye A., "Design and Development of a Novel Electrohydraulic Servovalve Configuration", Master Thesis, Department of Mech. Engg., Concordia University, Feb. 1985.

14. Hibi A. and Ichikawa T., "Measurement Method of Starting Torque of Hydraulic Motors", Hydraulic and Pneumatic Mech. Power, 21, 252, Dec. 1975, pp 434-439.

15. Hibi A. and Ichikawa T., "Mathematical Model of the Torque Characteristics for Hydraulic Motors", Bulletin of the JSME, Vol. 20, No. 143, May 1977, pp 616-621.

16. Nonnenmacher G., "Starting Characteristics of Hydraulic Motors", First European Fluid Power Conference, 10-12, paper no. 33, Sept. 1973.

17. Glickman and Myron, "Transient Speed Analysis of a Servovalve Controlled Hydraulic Motor", Proc. of National Conf. on Ind. Hydraulics, 16, 174, 1962.

18. Watton J., "The Generalised Response of Servovalve-Controlled, Single Rod, Linear Actuator and the Influence on Transmission Line Dynamics", Trans. of ASME, Journal of Dynamic Systems, Measurement and Control, Vol. 106, June 1984.

19. Shearer J.L., "Digital Simulation of a Coulomb Damped Hydraulic Servosystem", Trans. of ASME, Journal of Dynamic Systems and Control, Vol. 105, Dec. 1983.

20. Parnaby J., "Instability Due to Static and Coulomb Friction in

Autonomous Control Systems", Second Fluid Power Symposium, Guildford, England, Jan. 1971.

21. Leburn M. and Scavarda S., "Simulation of Nonlinear Behaviour of an Electrohydraulic Exciter", Simulation, Oct. 1979.

22. LeQuoc S., "Design of Hydraulic Servovalve for Maximum Pressure Sensitivity", Trans. of ASME, Vol. 106, March 1984, pp 116-119.

23. Vilenius M.J., "The Application of Sensitivity Analysis to Electrohydraulic Position Control Servos", Trans. of ASME, Journal of Dynamics Systems, Measurement and Control, Vol. 105, June 1983.

24. Farahat S., "Application of Sensitivity Analysis to Parameter Changes in Nonlinear Hydraulic Control Systems", Master Thesis, Department of Mech. Engg., Concordia University, July 1987.

25. McCloy D. and Martin H.R., "The Control of Fluid Power", Longman Group Limited, London, 1973.

26. Martin H.R. and McCloy D., "Some Aspect of Bistable Hydraulic Servos", Second Fluid Power Symposium, Guildford, England, Jan. 1971.

27. Montgomery J. and Lichtarowicz A., "The Effect of Assymmetrical Lap on the Performance of the Hydraulic Servomechanism", Second Fluid Power Symposium, Guildford, England, Jan. 1971.

28. Tumarkin M.B., "Hydraulic Servomechanisms : Structure and Kinematics", British Library Lending Division, U.K., 1975.

29. Parra A., "A Study of a Servovalve Controlled Hydraulic Radial Ball Piston Motor", Master Thesis, Department of Mech. Engg., Concordia University, Feb. 84.

30. LeQuoc S., Cheng R.M.H. and Leung K.H., "Frequency Response Analysis of a Novel Electrohydraulic Servosystem", Winter Annual Meeting, ASME paper 88-WA/DSC-52, Chicago, Illinois, Dec 1988.

APPENDIX I

CALIBRATION OF COMPONENTS

I.1 Metering Valve (Whitey 4RF4 Regulating Stem)

For the metering of the flow in the return line of the new configuration, a metering valve of 0.200" in orifice and C_v of about 0.51 was chosen.

To calibrate the flow capacity curve of the valve, two methods were used at the same time : the measurements by a turbine flowmeter for large flowrate or by a cylinder and a stopwatch for small flowrate. Fig. I.1 shows the circuit for the measurement.

The pressure difference across the metering valve was measured directly by connecting the inlet and outlet of the valve to the positive and negative ports of a calibrated differential pressure transducer. The flow coefficients, C_v , at half turn open intervals were calculated by the formula

$$Q = C_v \sqrt{\frac{\Delta P}{G}} \qquad \text{(I.1.1)}$$

where

ΔP = pressure difference (psi)

G = specific gravity.

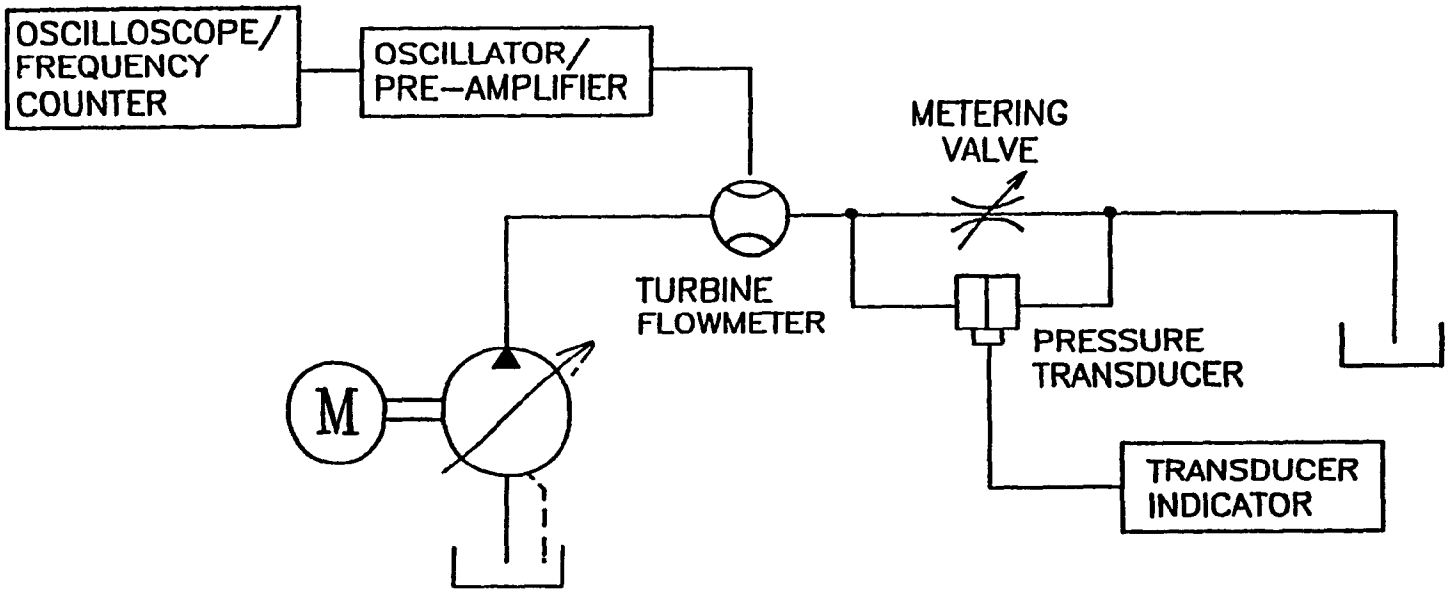

Fig. I.1 Hydraulic Ciruit for Calibration of Metering Valve

The flow capacity curves of the number of turns open against C_v were plotted. The two methods gave very similar results. The curve obtained by the more reliable timing method was shown in Fig. I.2 together with the curve provided by the manufacturer. This curve will be used as the standard for calculation of A_0 (the effective orifice area) in later calculations.

To convert C_v to A_0, the calculations are shown as follow :

$$Q_0 = C_v \sqrt{\frac{\Delta P \ (psi)}{G}} \ GPM, \qquad G = 0.867 \text{ for Tellus 46 oil}$$

$$= C_v \sqrt{\frac{\Delta P \ (psi)}{0.867}} \ GPM \times \frac{3.785 \times 10^{-3} \ m^3 s^{-1}}{60 \quad GPM} \qquad (\text{i.e. in } \frac{m^3}{s})$$

The flowrate can also be given in a second formula :

$$Q_0 = C_d A_0 \sqrt{\frac{2\Delta P \ (Nm^{-2})}{\rho \ (kgm^{-3})}}$$

$$= 0.61 \ A_0 \sqrt{\frac{2 \ \Delta P \ (psi) \times 6894.4 \ (N/m^2/psi)}{867 (kgm^{-3})}} \qquad (\text{i.e. in } \frac{m^3}{s})$$

By equating Q_0, now both in m^3s^{-1}, and eliminating ΔP (both in psi)

$$C_v \frac{1}{\sqrt{0.867}} \times \frac{3.785 \times 10^{-3}}{60} = 0.61 \sqrt{\frac{2 \times 6894.4}{867}} A_0$$

hence $$A_0 = 2.84 \times 10^{-5} \ C_v \ m^2$$

Calibration Curve
for the Metering Valve
by Timing Method

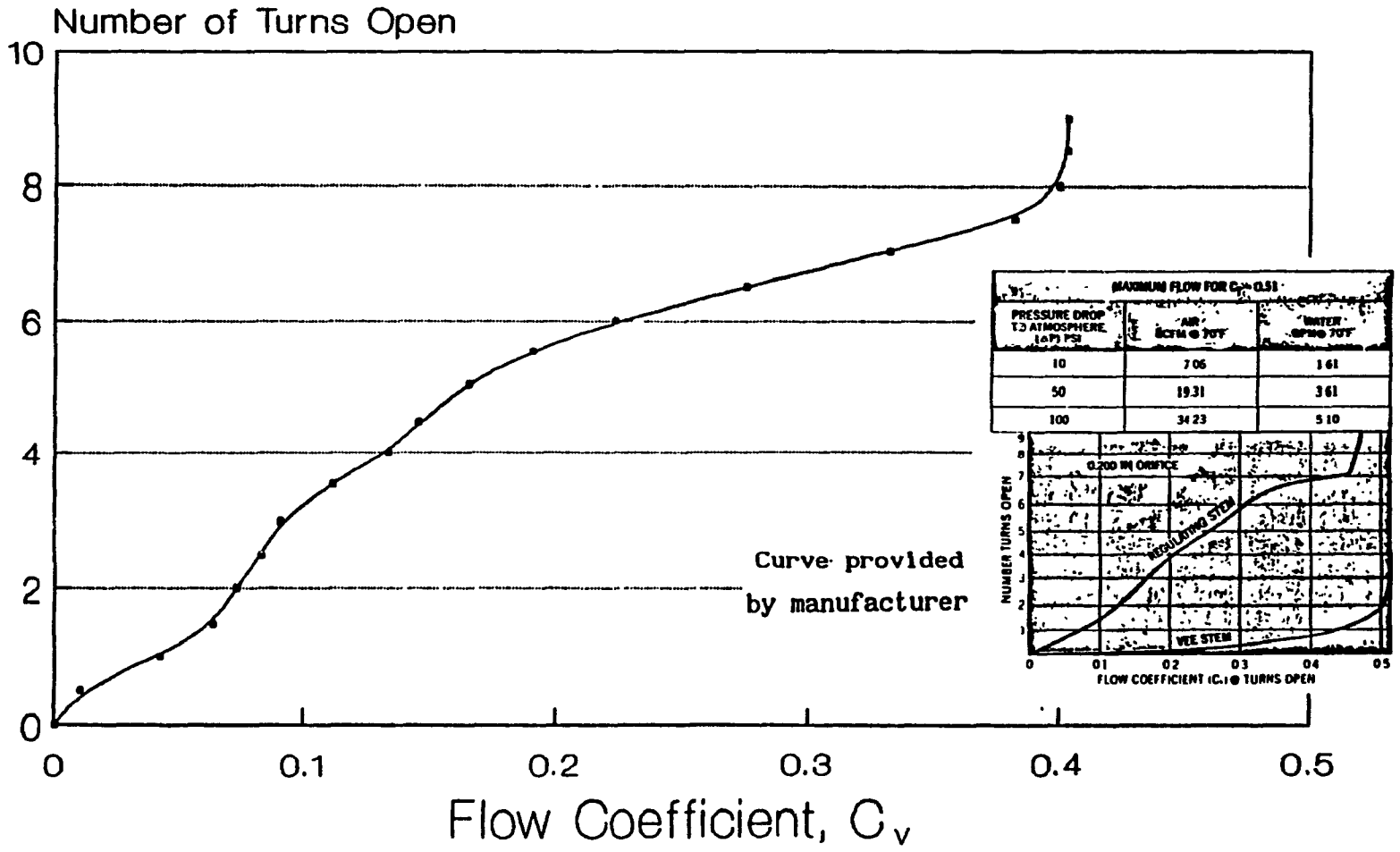

Fig. I.2 Flow Capacity Calibration Curve of the Metering Valve by Timing Method

I.2 Pressure Relief Valve (Vickers CG03B10, pilot operated, 0-8 GPM, 75-1000 psi)

The relief valve chosen was satisfactory because it could keep a very constant back pressure on the drain line despite the upstream pressure (except when the upstream pressure was oscillating rapidly.)

The back pressure on the drain line was monitored by means of a pressure transducer connected before the relief valve. As a matter of reference, a graph of relief pressure plotted against the number of turns in closing the relief valve with zero turn defined at the cracking pressure of the relief valve. (Fig. I.3)

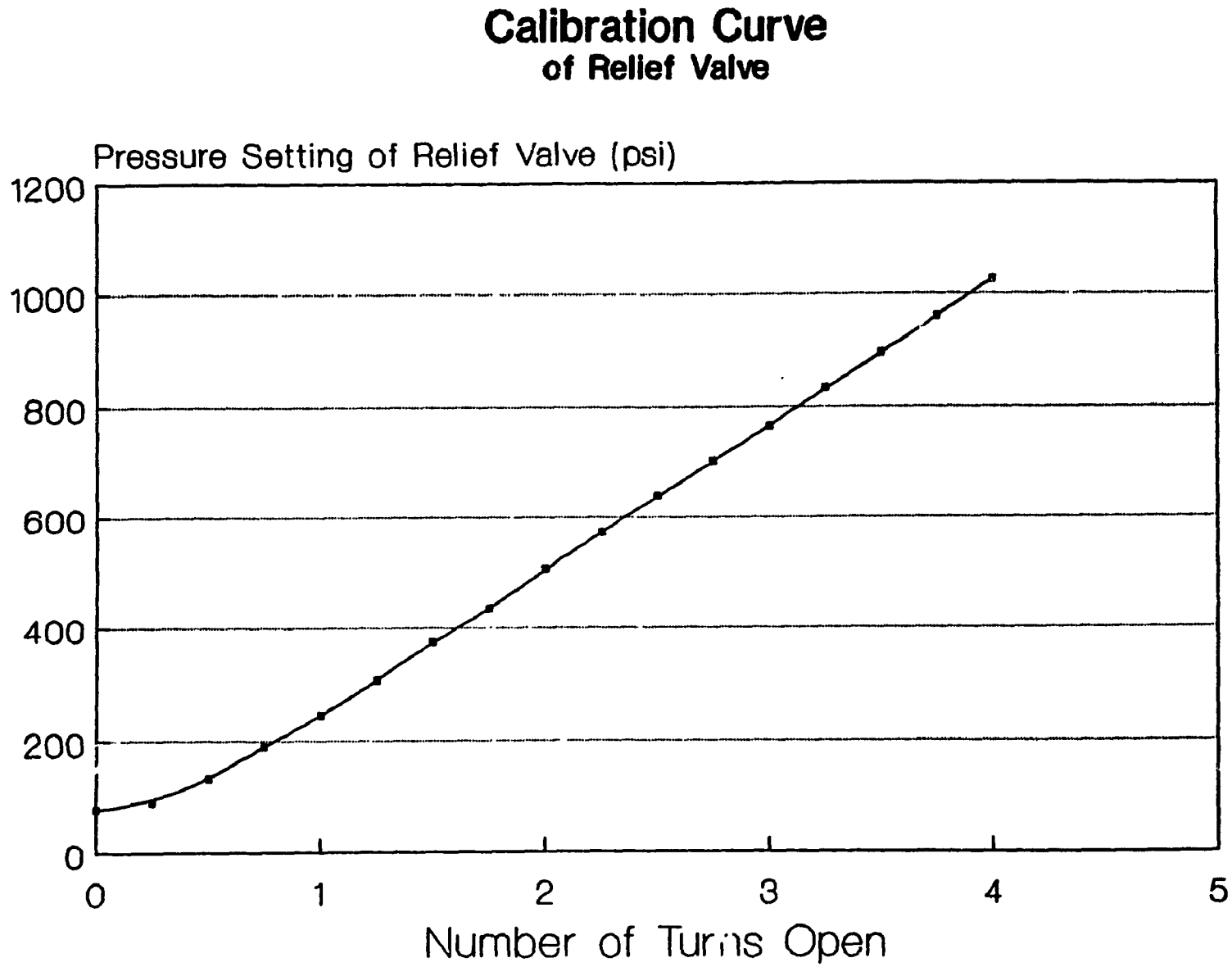

Fig. I.3 Calibration Curve of Relief Valve

I.3 Pressure Transducer

Three Validyne transducers (DP15T) with diaphragms of 1000 psi rating were used to measure the pressures at the inlet and outlet ports of the motor and before the relief valve. They were calibrated by means of a dead weight tester together with their corresponding transducer indicators in steps of 100 psi. The calibration curves were shown in the graphs Fig. I.4, I.5 and I.6.

The positive ports of the transducers were connected to the output of the dead weight tester and the negative ports were opened to the atmosphere. Hysteresis (less than 25 psi) was sometimes observed after the pressure inside the transducer was released.

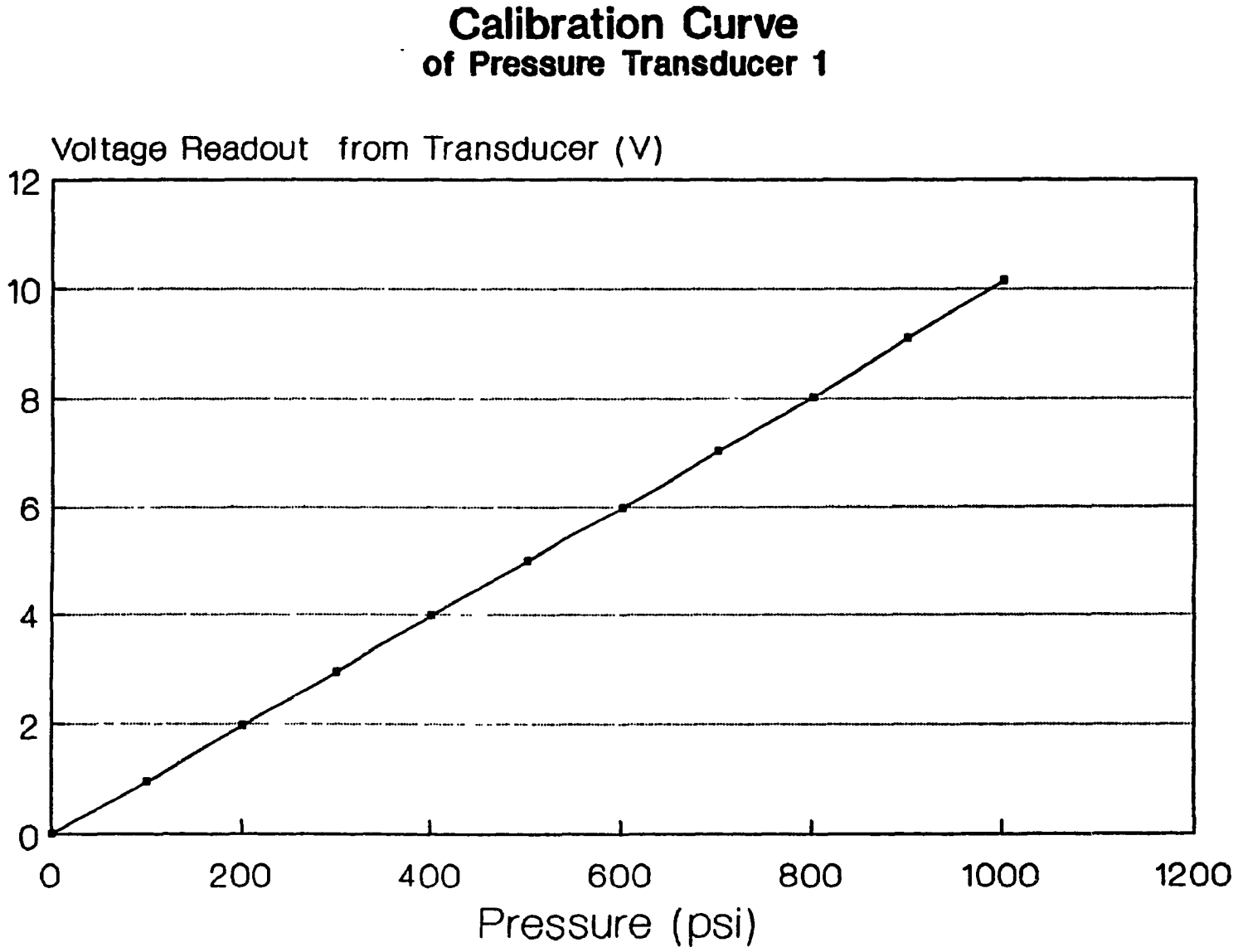

Fig. I.4 Calibration Curve of Pressure Transducer 1 for Port 1 of Servomotor

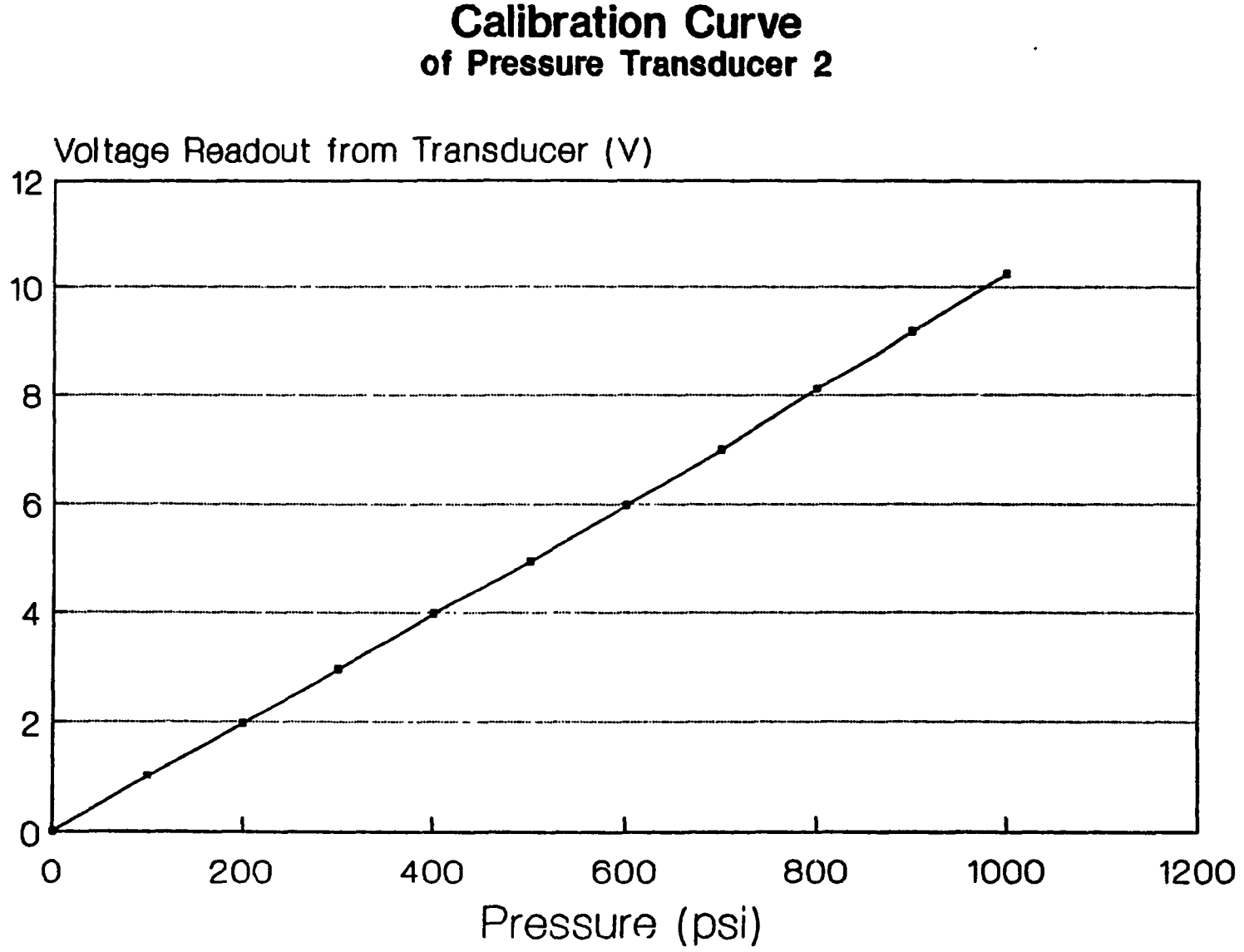

Fig. I.5 Calibration Curve of Pressure Transducer 2 for Port 2 of Servomotor

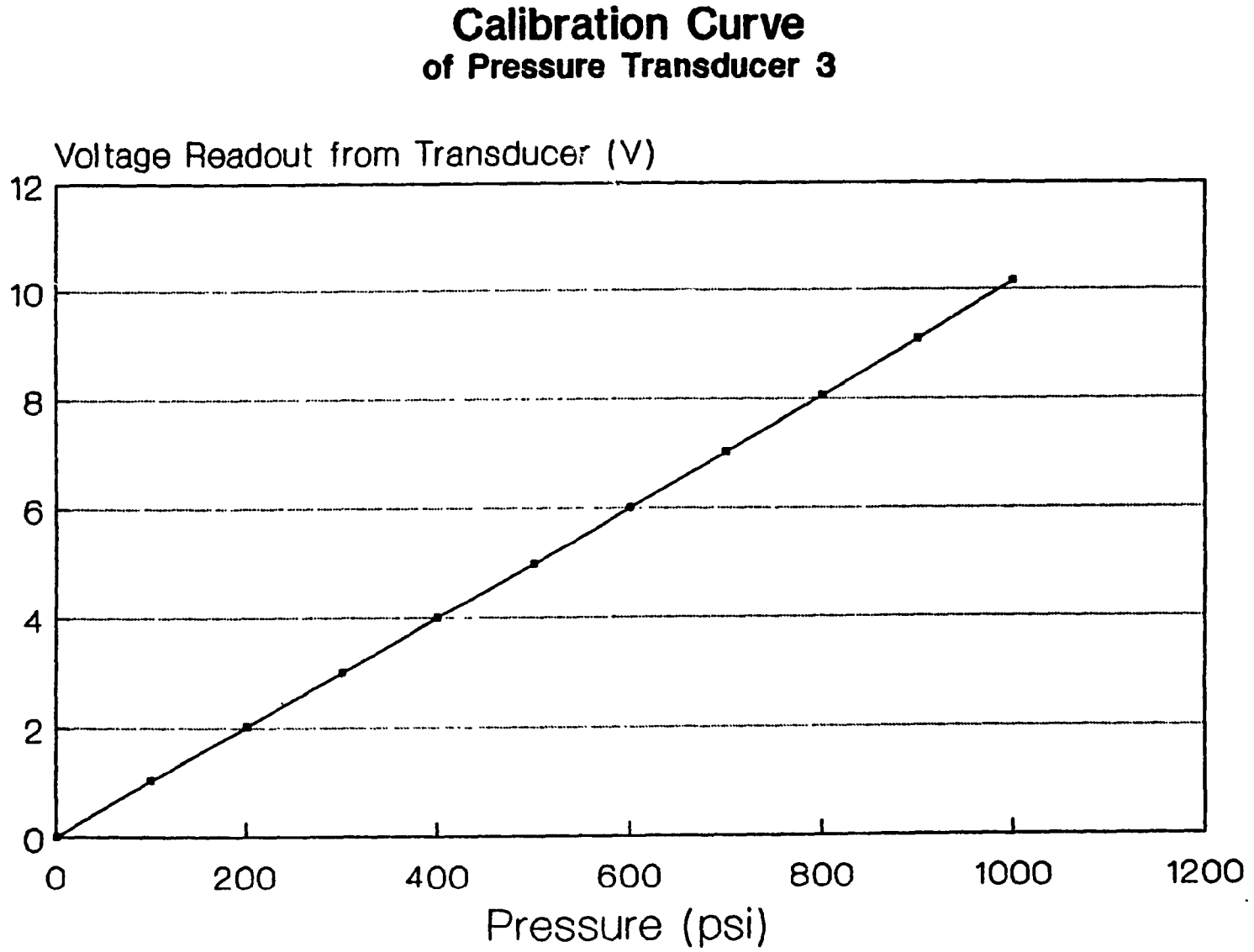

Fig. I.6 Calibration Curve of Pressure Transducer 3 for Relief Valve

I.4 Torque Transducer and Strain Gauge Amplifier

Torque transducer : British Hovercraft Corporation Limited, England.

TT2/4/CA

Sensitivity 2.260 mV/V at 100 lb-ft

Speed range 0-6000 rpm

A differential strain gauge amplifier was built to magnify the differential output signal from the transducer, the order of which was in few mV. The amplifier could also be used to adjust the gain of the feedback torque signal in a closed loop system.

The transducer was calibrated and compared with the calibration curve provided by the manufacturer. A voltage difference of 10.21 V was applied across the transducer through the amplifier. At first, the torque transducer and amplifier were calibrated as a whole by clamping the shaft of the motor with a L-beam lever. The other end of the beam pressed on a load cell one foot away (Fig. I.7). Step pressure difference inputs of approximately 200 psi were applied on the motor up to 2000 psi. The stalling torque applied on the motor was calculated by multiplying the torque arm length and force acting on the load cell together. The gain on the amplifier was adjusted until the sensitivity of the torque and amplifier together was 50 Nm/V. Data points at approximately 200 psi intervals were taken and plotted on graph Fig. I.8. The slope of the graph was 49.95 Nm/V. The differential amplifier was then calibrated alone by step inputs of 20 mV. The calibrated curve

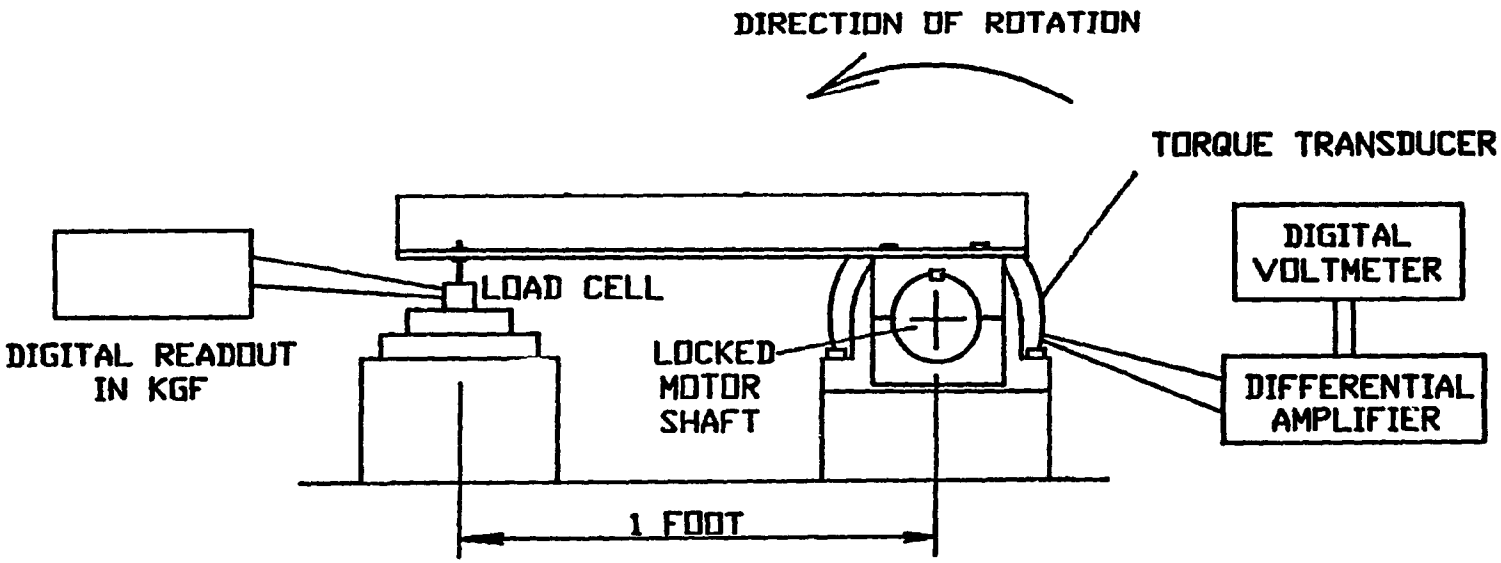

Fig. I.7 Experimental Arrangement for the Calibration of the Torque Transducer

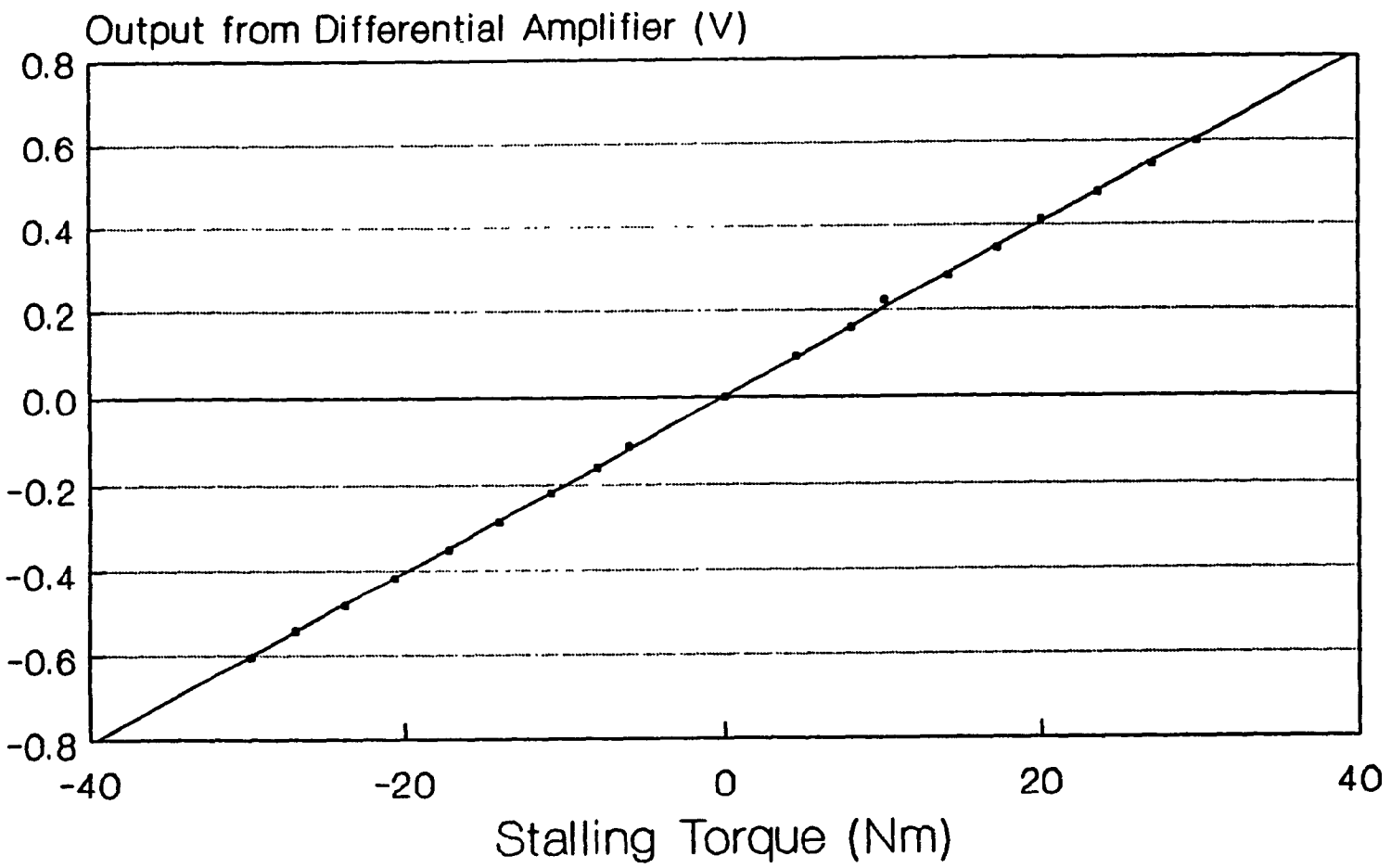

Fig. I.8 Calibration Curve for Torque Transducer and Differential Amplifier Combination

was shown on Fig. I.9. The slope of the graph was 0.1177 V/mV.

Hence, the sensitivity of the torque transducer alone was 1/(0.1177V/mV x 49.95Nm/V) = 0.170 mV/Nm. Meanwhile, the value provided by the manufacturer was also 0.170 mV/Nm (excitation voltage 10.21 V).

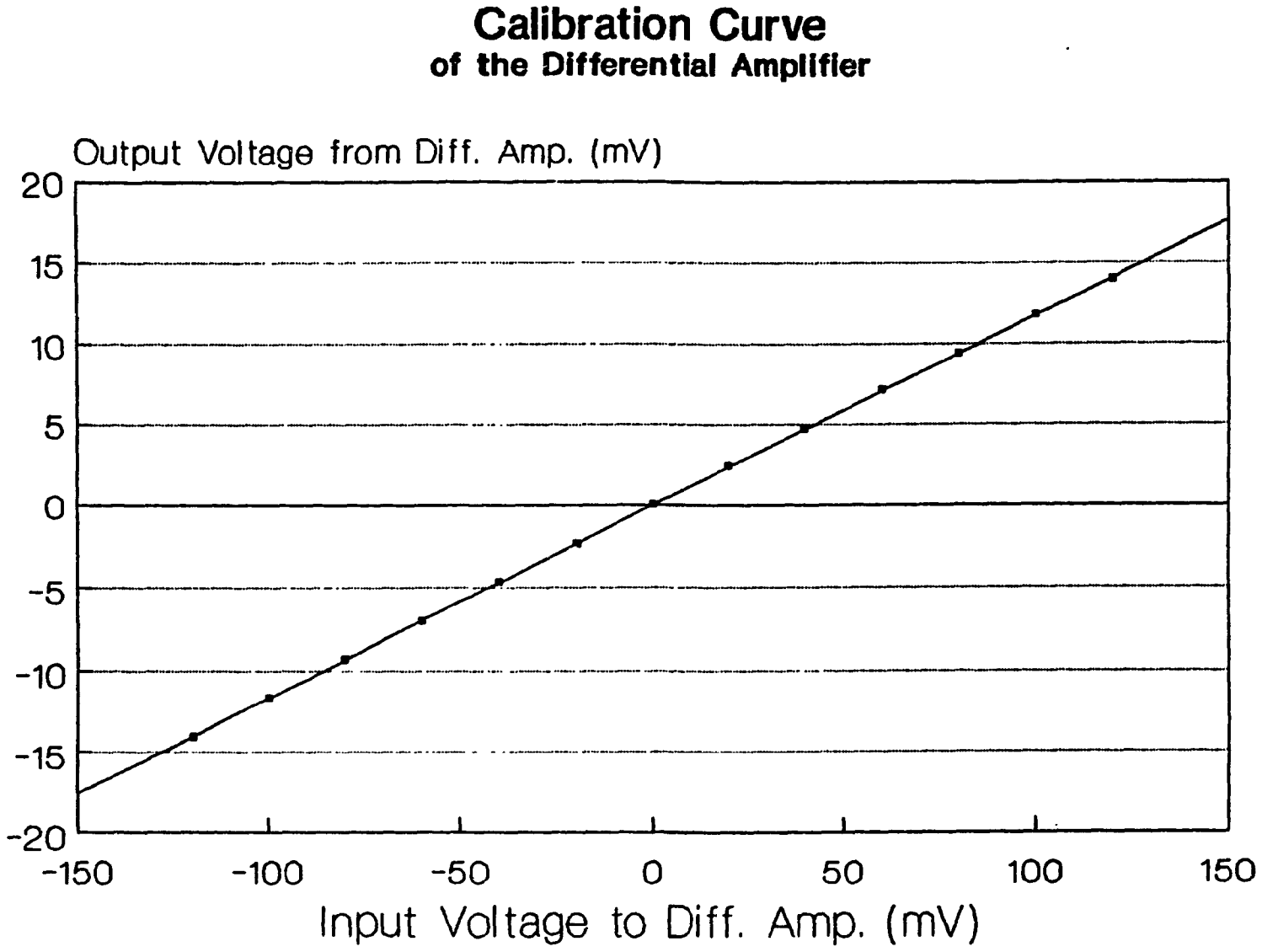

Fig. I.9 Calibration Curve for Differential Amplifier

I.5 Tachometer

The tachometer was calibrated in the Mechanical Engineering Workshop by means of a NC turning machine. The velocity was read from its digital readout. Only one direction of rotation could be measured and the sensitivity of the opposite direction was assumed to be the same due to symmetry. (Fig. I.10)

The calibration sensitivity was 20.4 V/1000 rpm while the value provided by the company was 20.8 V/1000 rpm.

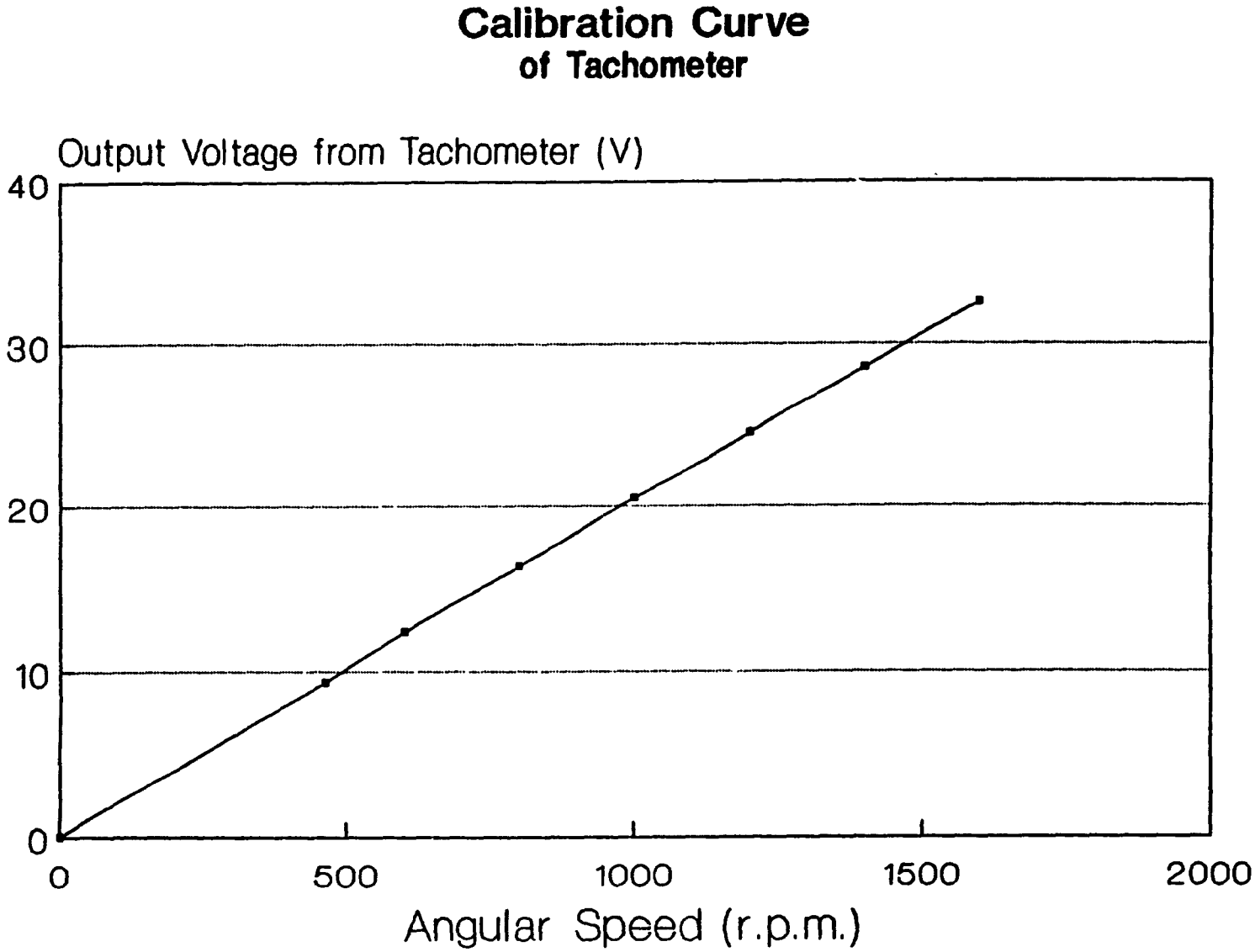

Fig. I.10 Calibration Curve of Tachometer

I.6 Directional Control Valve and On-Off Controller

Differential control valve : Yuken DSG 01 3C2 A120 5090

Maximum pressure : 4500 psi

Maximum flowrate : 16.6 GPM

Coil type : 120 V a.c.

An on-off controller was built to drive the solenoids of the directional control valve. Depending on the sign of the input signal from the summation op-amp inside the servo-controller, appropriate solenoid was activated and the switching of the supply and drain ports can be achieved.

The time delay in actuation of the directional control valve was defined as the time taken for the pressure transducer to start to vary after the step input signal (the effect could be clearer for square wave) switched a step. The delay was seen from experiment to vary between 4 to 12 ms. Fig. I.11 shows the effect of time delay on the pressure switching.

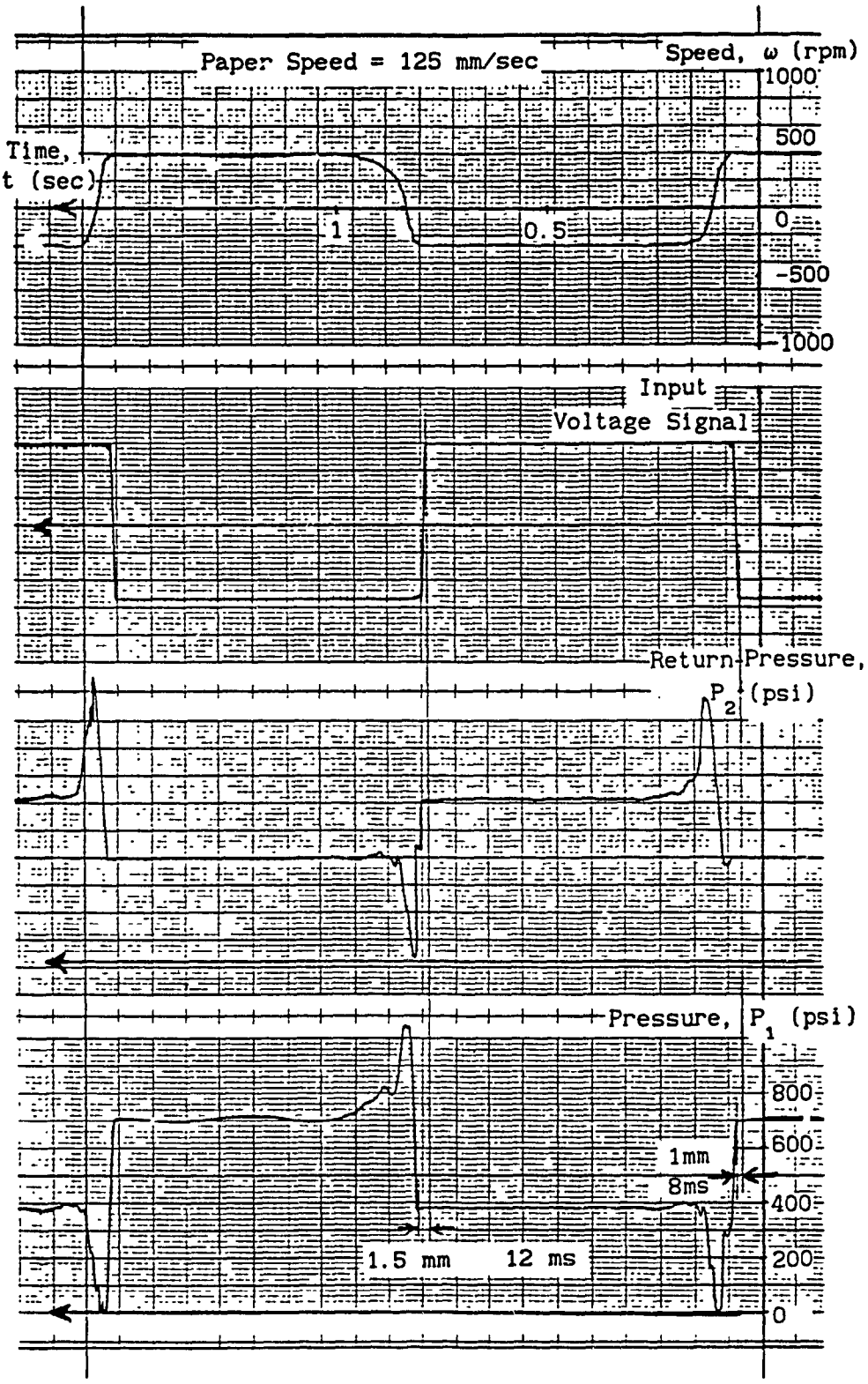

Fig. I. 11 Effect of Pure Time Delay on Step Change of Direction of Flow in New Configuration

APPENDIX II

ELECTRONIC CIRCUIT DIAGRAMS

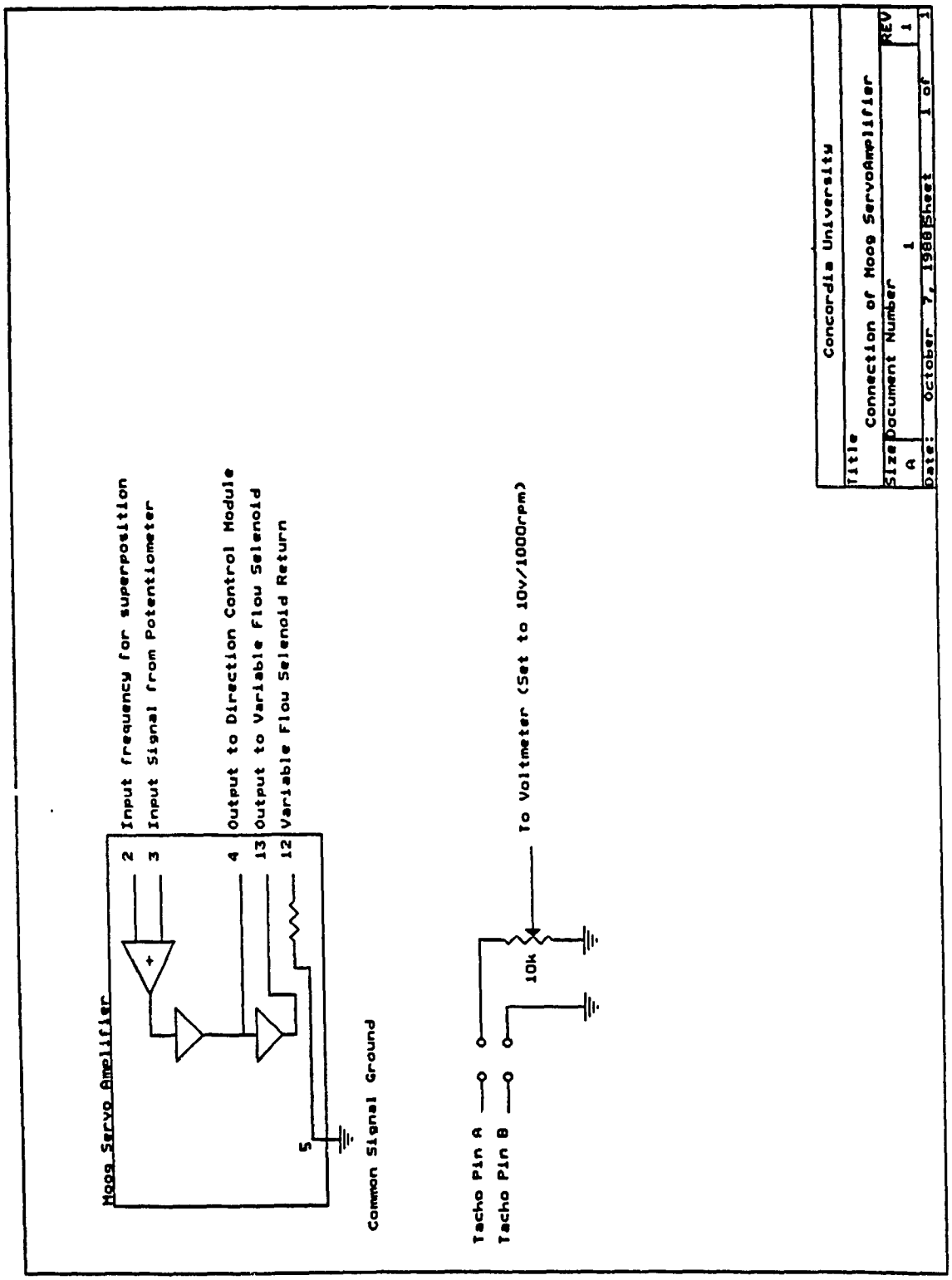

Fig. II.1 Pin Connection Diagram to the Moog Servo Amplifier for Controlling of Servovalve of the Motor

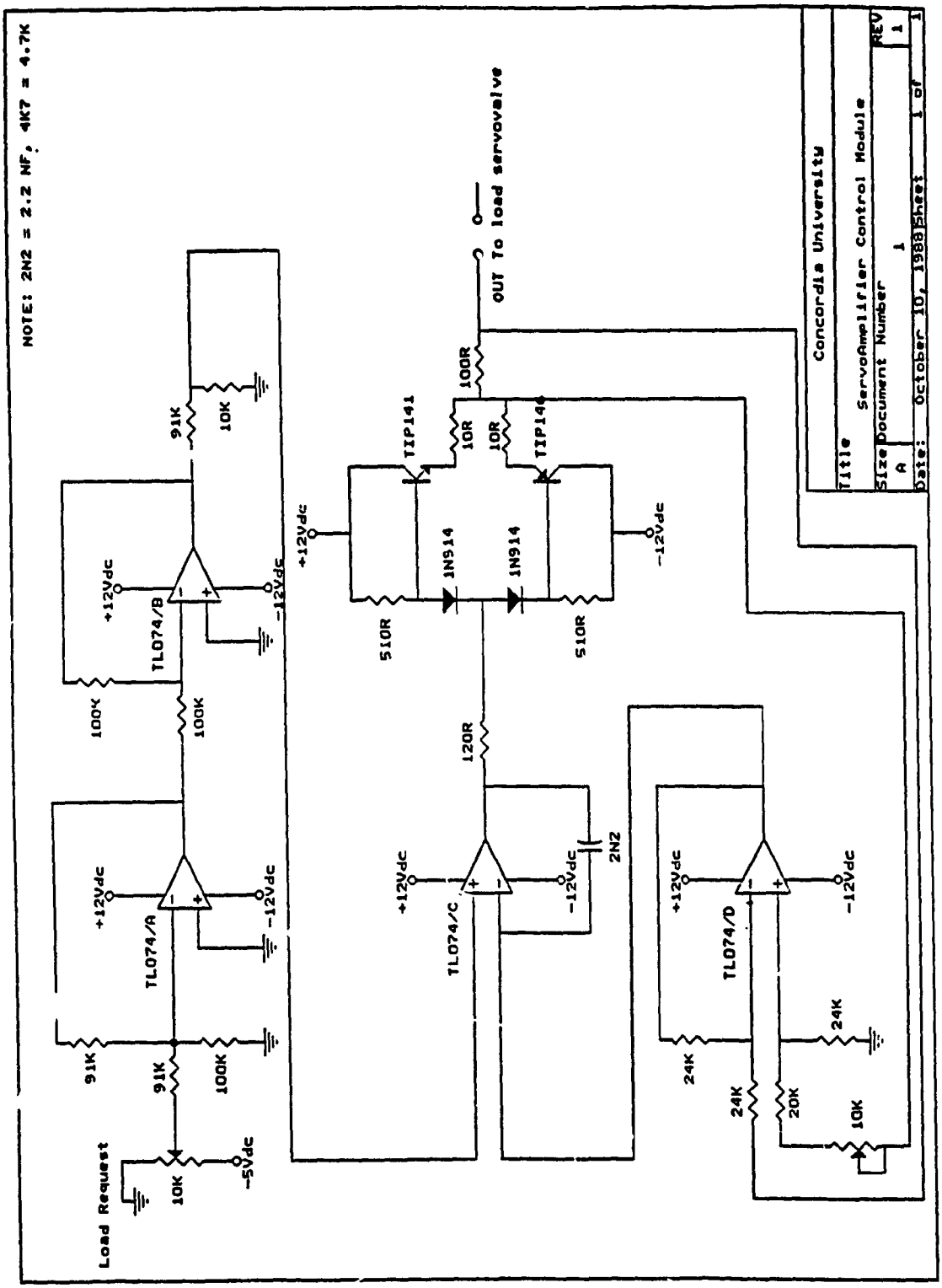

Fig.II.2 Servoamplifier Control Module for the Servovalve of the Pump

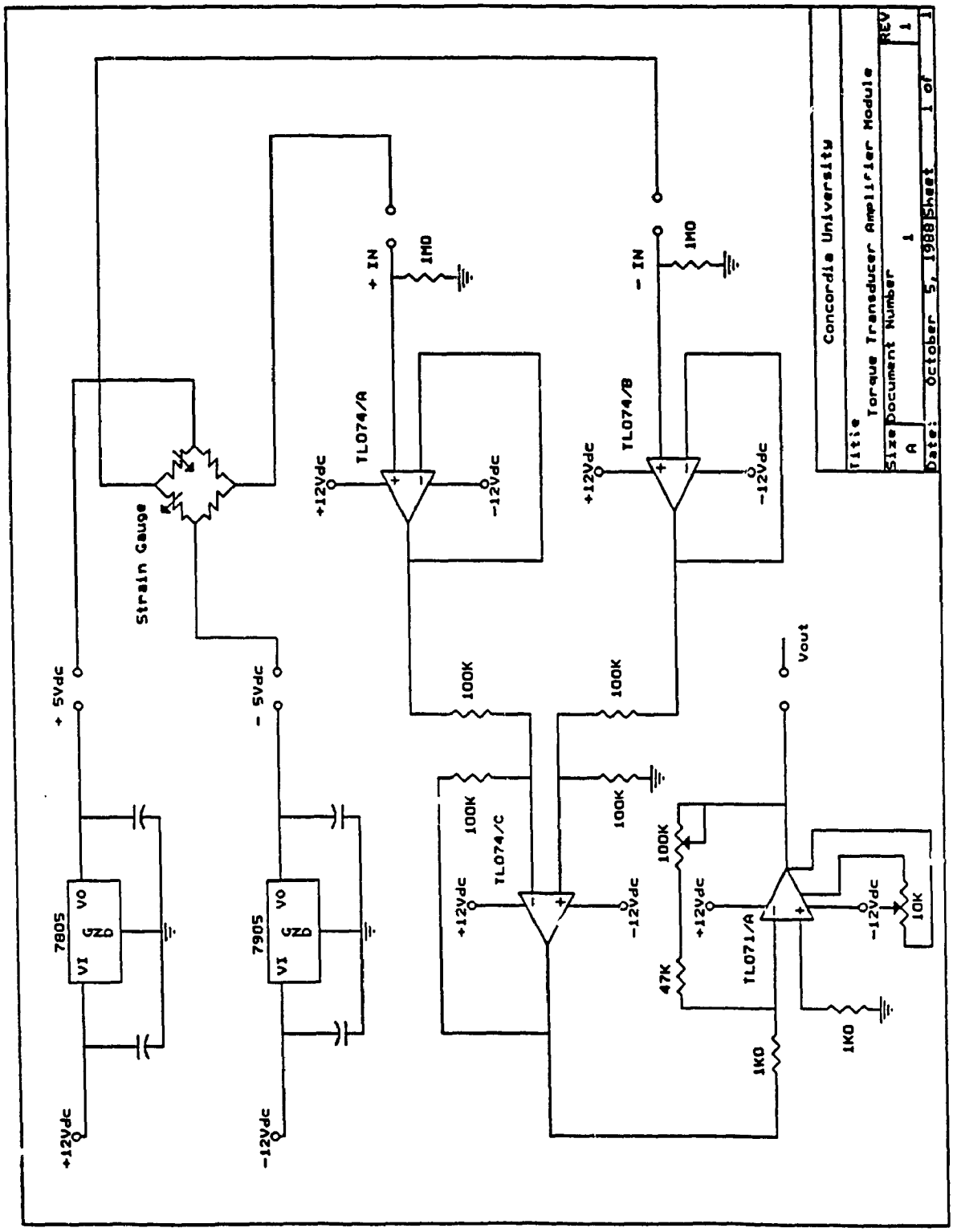

Fig. II.3 Torque Transducer Amplifier Module

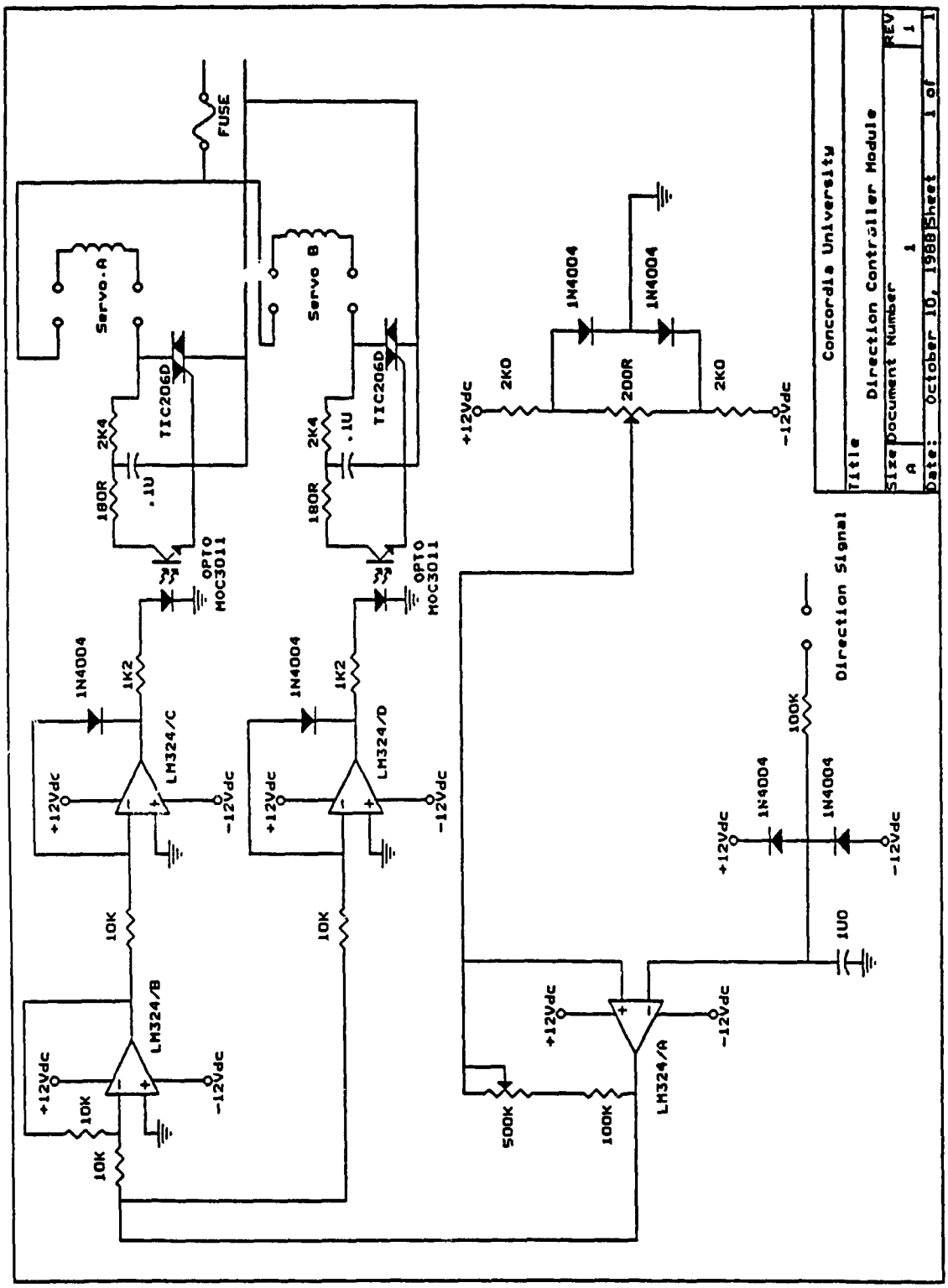

Fig. II.4 Direction Controller Module

APPENDIX III

EFFECT OF NONLINEARITIES ON THE RESPONSES OF THE SYSTEM

Nonlinearities such as the unsymmetry of the servovalve, the dead zone from the overlapped region between the spool and the body of the servovalve, and static friction have great effects on the responses of the system during the switching of direction of rotation. In order to investigate the effect, sinusoidal waves are input to the setup, the outputs of the tachometer, torque transducer and pressure transducer are recorded on a four strip chart recorder.

In Fig. III.1, a dead zone can be found from the zero velocity region of the output response. A small shock wave can be proved for having existed during switching from the observation of the disturbances in the torque transducer pressure output responses. In the case of the new configuration, the switching time delay of the directional control valve, which accounts to about 8 ms, causes an even larger shock wave during switching. During the time delay, the pressure inside the exit chamber builds up. When the valve area between the spool and the body of the directional control valve suddenly open, the abrupt release of pressure creates a shock wave in the oil. The existence of shock wave can again be verified from the pressure and torque transducers outputs on the strip chart recorder diagram, Fig. III.2a and Fig. III.2b. The shock wave becomes more and more prominent with increasing input frequencies. When the input frequency is above 7 Hz, the shock wave overcomes the sinusoidal output and makes the reading for the frequency

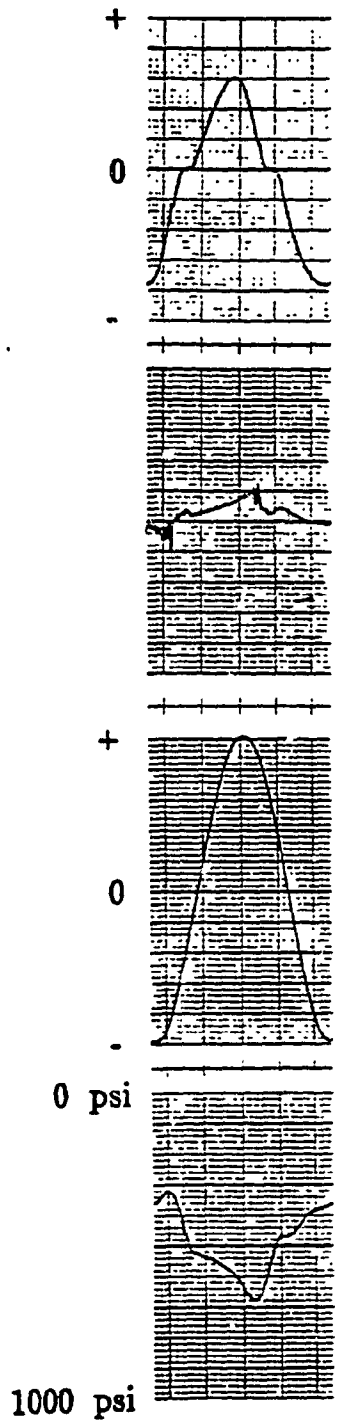

Output wave form showing the effect of dead zone acrosss zero line

Transducer signal (notice the shock wave disturbance after switching)

Input sine wave (notice the phase lead of the input over the output)

Pressure signal (notice the pressure peak from the shock wave after switching

(paper speed = 125 mm/s)

Fig. III.1 Frequency Response of Conventional Configuration at 5 Hz, Showing the Effect of the Dead Zone across the null Region

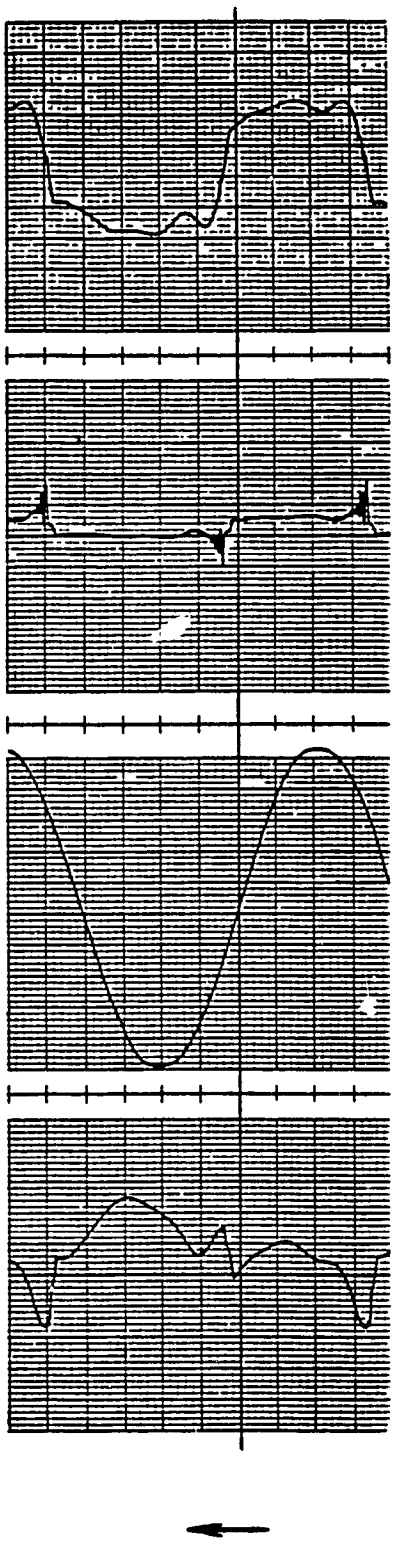

Fig. III.2a Frequency Response of New Configuration at 5 Hz, Showing the Effect of the Dead Zone across the Null Region

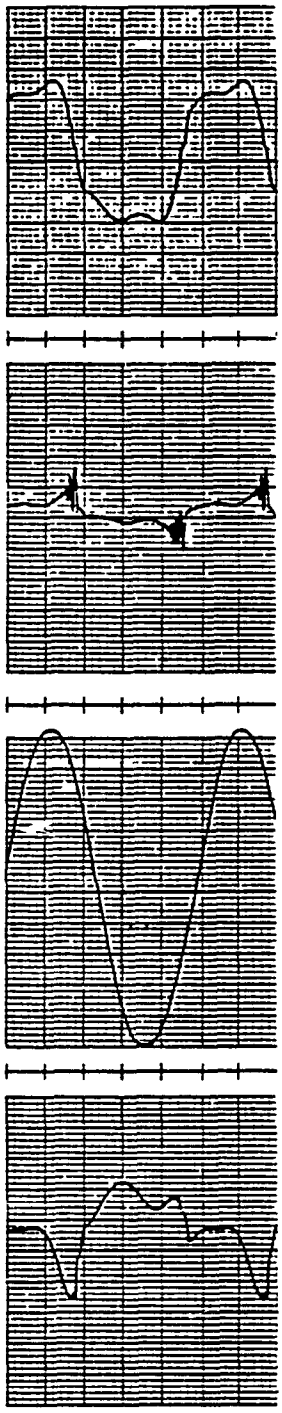

Fig. III.2b Frequency Response of New Configuration at 5 Hz, Showing the Peak Very Close to the Maximum of the Output Response

reponse impossible, Fig. III.2c and Fig. III.2d. If the input frequency is higher than 25 Hz, the directional control valve misses some steps in switching, giving an irregular output, Fig. III.3. Hence, in order to avoid the crossing of the output zero velocity line and the subsequent nonlinearities, an offsetted input should be introduced in the simulations and experiments.

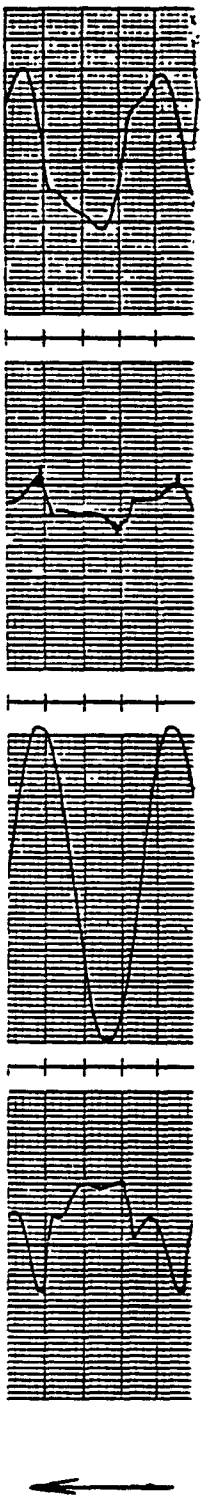

Fig. III.2c Frequency Response of New Configuration at 7 Hz, Showing How the Shock Wave Dominates the Peak of the Output Response

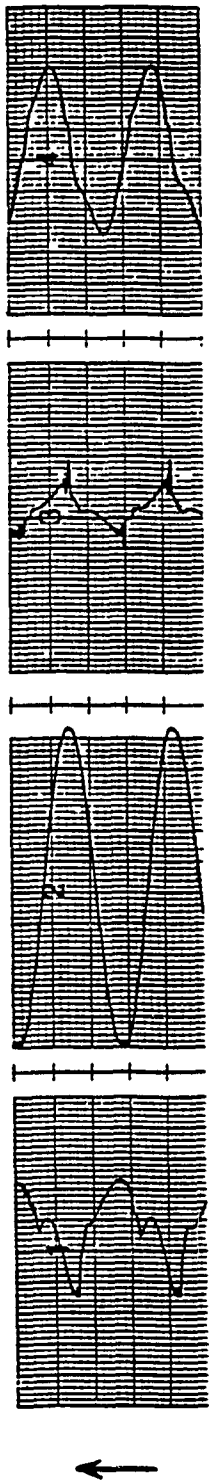

Output wave form

Transducer signal

Input sine wave

Pressure signal

Fig. III.2d Frequency Response of New Configuration at 9 Hz, Showing that the Peak of the Output is Actually Produced by the Shock Wave

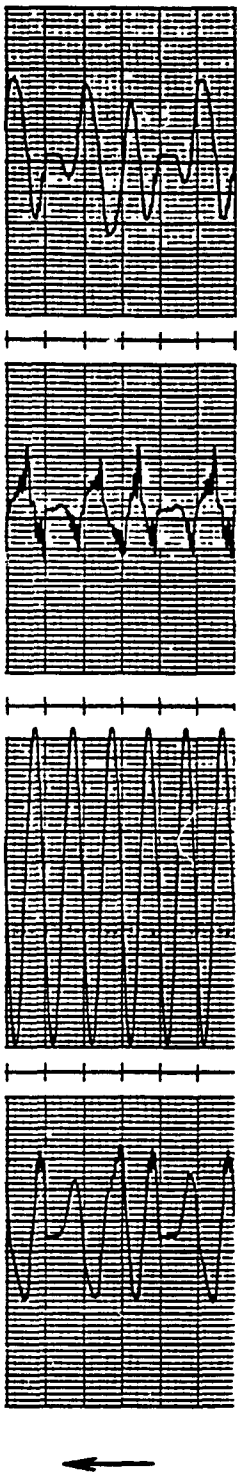

Fig. III.3 Irregular Output Waveform of the New Configuration at 25 Hz, Showing the Effect of the Missing Steps of the Directional Control Valve